2021

Development of a Hybrid-Electric Aircraft Propulsion System Based on Silicon Carbide Triple Active Bridge Multiport Power Converter

Cole M. Ivey
University of Kentucky, civey62598@gmail.com
Digital Object Identifier: https://doi.org/10.13023/etd.2021.443

STUDENT AGREEMENT:

I represent that my thesis or dissertation and abstract are my original work. Proper attribution has been given to all outside sources. I understand that I am solely responsible for obtaining any needed copyright permissions. I have obtained needed written permission statement(s) from the owner(s) of each third-party copyrighted matter to be included in my work, allowing electronic distribution (if such use is not permitted by the fair use doctrine) which will be submitted to UKnowledge as Additional File.

I hereby grant to The University of Kentucky and its agents the irrevocable, non-exclusive, and royalty-free license to archive and make accessible my work in whole or in part in all forms of media, now or hereafter known. I agree that the document mentioned above may be made available immediately for worldwide access unless an embargo applies.

I retain all other ownership rights to the copyright of my work. I also retain the right to use in future works (such as articles or books) all or part of my work. I understand that I am free to register the copyright to my work.

REVIEW, APPROVAL AND ACCEPTANCE

The document mentioned above has been reviewed and accepted by the student's advisor, on behalf of the advisory committee, and by the Director of Graduate Studies (DGS), on behalf of the program; we verify that this is the final, approved version of the student's thesis including all changes required by the advisory committee. The undersigned agree to abide by the statements above.

Cole M. Ivey, Student

Dr. JiangBiao He, Major Professor

Dr. Daniel Lau, Director of Graduate Studies

DEVELOPMENT OF A HYBRID-ELECTRIC AIRCRAFT PROPULSION SYSTEM BASED ON SILICON CARBIDE TRIPLE ACTIVE BRIDGE MULTIPORT POWER CONVERTER

THESIS

A thesis submitted in partial fulfillment of the requirements for the degree of Master of Science in Electrical Engineering in the College of Engineering at the University of Kentucky

By

Cole M. Ivey

Lexington, Kentucky

Director: Dr. JiangBiao He

Department of Electrical and Computer Engineering

University of Kentucky

2021

ABSTRACT OF THESIS

DEVELOPMENT OF A HYBRID-ELECTRIC AIRCRAFT PROPULSION SYSTEM BASED ON SILICON CARBIDE TRIPLE ACTIVE BRIDGE MULTIPORT POWER CONVERTER

Constrained by the low energy density of Lithium-ion batteries with all-electric aircraft propulsion, hybrid-electric aircraft propulsion drive becomes one of the most promising technologies in aviation electrification, especially for wide-body airplanes. In this thesis, a three-port triple active bridge (TAB) DC-DC converter is developed to manage the power flow between the turbo generator, battery, and the propulsion motor. The TAB converter is modeled based on the emerging Silicon Carbide (SiC) Metal-Oxide-Semiconductor Field Effect Transistor (MOSFET) modules operating at high switching frequency, so the size of the magnetic transformer can be significantly reduced. Different operation modes of this hybrid-electric propulsion drive based on the SiC TAB converter are modeled and simulated to replicate the takeoff mode, cruising mode, and regenerative charging mode of a typical flight profile. Additionally, soft switching is investigated for the TAB converter to further improve the efficiency and power density of the converter, and zero voltage switching is achieved at heavy load operating conditions. The results show that the proposed TAB converter is capable of achieving high efficiency during all stages of the flight profile.

KEYWORDS: Hybrid-electric aircraft, multiport converter, high efficiency, triple active bridge, high power density, soft switching

Cole M. Ivey

November 8, 2021

DEVELOPMENT OF A HYBRID-ELECTRIC AIRCRAFT PROPULSION SYSTEM BASED ON SILICON CARBIDE TRIPLE ACTIVE BRIDGE MULTIPORT POWER CONVERTER

By
Cole M. Ivey

Dr. JiangBiao He
Director of Thesis

Dr. Daniel Lau
Director of Graduate Studies

November 8, 2021

ACKNOWLEDGMENTS

This thesis, while an individual work, is the result of input and support from several people. I would first like to thank my academic advisor, Dr. JiangBiao He, for his continuous support and mentorship throughout my graduate career. His advice throughout has been invaluable to me and to the completion of this work. I would like to thank my other thesis committee members – Dr. Aaron Cramer, Dr. Yuan Liao, and Dr. Joseph Sottile – for their valuable feedback. Sincere thanks also to Dr. Abdulgafor Alfares for generously lending his advice and expertise to this thesis. Additionally, I would like to acknowledge my peers Pranoy Roy, Majid Fard, and Ben Luckett who are PhD students with me in AMPERE Lab, for their input and suggestions.

I would like to gratefully acknowledge Dr. Lawrence Holloway and the Tennessee Valley Authority, as well as NASA Kentucky, for the financial support of the research presented in this thesis.

Finally, I would like to thank my parents and my closest friends for their endless support and encouragement.

TABLE OF CONTENTS

LIST OF TABLES

LIST OF FIGURES

CHAPTER 1. INTRODUCTION

1.1 Research Motivation

In recent years, a global effort has been directed towards reducing emissions in all sectors to combat climate change. The general scientific consensus is that global warming must be limited to 1.5 °C above pre-industrial levels to prevent catastrophic consequences [1]. To limit global warming to 1.5 °C, drastic reductions in greenhouse gas emissions must be made as soon as possible [2]. As such, there has been an increasing amount of interest in renewable energy and electrified transportation technology.

Emissions from traditional aircraft are made up of several compounds, with carbon dioxide (CO_2) and nitrogen oxides (NO_x) being the primary climate-forcing pollutants [3]. In 2018, aviation was responsible for one gigaton of CO_2 emissions, accounting for roughly 2.5% of global CO_2 emissions [4, 5]. However, since aircraft release pollutants in sensitive areas of the atmosphere, their emissions have a disproportionate impact on the climate. When considering other factors such as contrails, NO_x emissions, and other atmospheric interactions, it is estimated that aviation accounts for 3.5% of global warming [6]. Of these emissions, roughly 81% are due to passenger aircraft [7]. The full breakdown of aviation-related CO_2 emissions is shown in Figure 1.1.

Without new technologies, emissions from aviation are bound to increase significantly as global demand for air transport is expected to triple from 2020 to 2050 according to pre-COVID-19 estimates [6]. To facilitate development in this area, technology roadmaps such as the European Union's (EU) Flightpath 2050 and the International Air Transport Association's (IATA) Aircraft Technology Roadmap to 2050 lay out a path to a lower carbon future in aviation. Released in 2011 by the EU Commission,

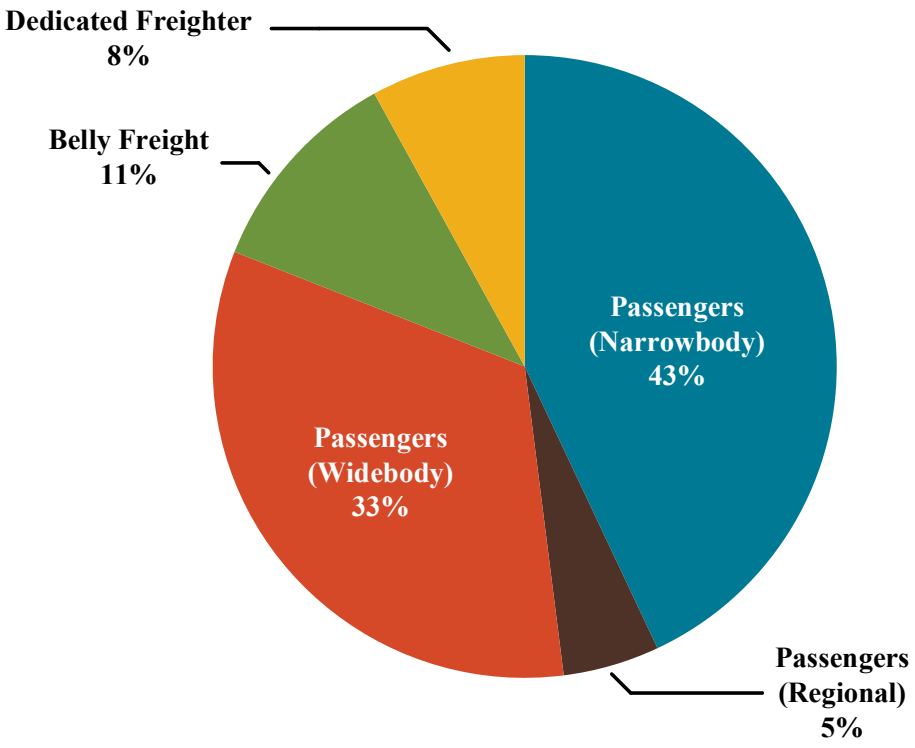

Figure 1.1: Breakdown of aviation-related emissions [7].

Flightpath 2050 sets goals to decrease CO_2 emissions by 75% and NO_x emissions by 90% [8]. While near-term advancements such as alternative fuels and improved engine design offer significant emissions reductions, their potential eventually plateaus. For example, according to the IATA, when compared to a baseline aircraft in 2015 evolutionary engine improvements can reduce fuel burn by up to 25% [9]. On the other hand, all-electric aircraft (AEA) can achieve zero emissions with much higher energy efficiency, but AEA is only feasible for small airplanes (e.g., up to 20-seat urban region airplanes) due to the much lower energy density of present batteries compared to that of jet fuel. For large aircraft such as twin-engine wide-body systems, hybrid-electric propulsion has the potential to reduce fuel burn by 40-60% [9, 10]. Additionally, there is a tradeoff between CO_2 and NO_x reduction in traditional aircraft engine design - decreasing one increases the other [11]. To

decrease CO_2 emissions in an aircraft engine, engine pressure and temperature must be increased. This process also results in increased production of NO_x. By electrifying propulsion systems and using battery storage to supplement power, both CO_2 and NO_x emissions can be reduced without tradeoff, since overall fuel burn is reduced by means of electrification rather than engine modifications.

Electrified aircraft also have the potential to improve overall system efficiency when compared to traditional aircraft. It is estimated that hybrid-electric aircraft can improve cruise efficiency by as much as 12% compared to a traditional internal combustion engine [12]. All-electric propulsion systems offer even more drastic improvements with an overall system efficiency of 75–83%, compared to the 20–36% of a traditional aircraft system [13]. In addition to the benefits of hybrid-electric and all-electric propulsion, more electric aircraft (MEA) have shown that auxiliary systems can achieve higher energy efficiency, higher reliability, and lower operational cost through electrification [14]. The Boeing 787 for example harbors a total of 1.45 MW of onboard power for systems such as electric air conditioning, electric driven hydraulic pumps, electric brakes, etc. [15]. By electrifying secondary systems that would not conventionally use electric power, the 787 achieves a 20% reduction in fuel burn and CO_2 and a 60% smaller acoustic noise footprint compared to the Boeing 767.

Acoustic noise is another problem that aircraft manufacturers must address in future designs. Long-term exposure to airport noise has been found to increase the risk of cardiovascular disease in adults, affect academic performance in children, and disrupt sleep in communities located nearby [16]. While the number of people affected by airport noise has been reduced significantly since the 1970s, as of 2012 more than 300,000 people in the

United States were still exposed to significant noise levels [17]. Flightpath 2050 calls for acoustic noise emissions in aircraft to be reduced by 65% between 2011 and 2050. While many measures can be taken to reduce aircraft noise, it is estimated that electric propulsion could reduce aircraft noise by up to 85% [18].

Overall, hybrid-electric aircraft (HEA) have proven to be a very promising approach to significantly reduce gas emissions, acoustic noise, operation cost, and improve system efficiency compared to conventional engine-based aircraft propulsion systems. The low energy density of present Lithium-ion batteries – about 50 times lower than liquid fuel – significantly constrains the payload capacity and flight range of electric aircraft, which is why battery-powered AEA are only suitable for interstate small airplanes such as flying taxis or flying cars [19]. In comparison, it is estimated that increases in battery specific energy density by 2040 would allow for HEA to meet up to 75% of regional transportation demand [20]. Figure 1.2 shows estimated payload vs. flight range and power rating for a variety of electric propulsion technologies – we can see that AEA are limited to small commuter aircraft due to the low energy density of batteries, while HEA are able to cover a wide range of payloads and flight range. For these reasons, HEA will be key to lowering emissions over the next few decades, and research into enabling technologies such as high efficiency lightweight power electronic converters for managing the power flow in hybrid-electric aircraft is a crucial first step.

1.2 Electrified Aircraft and Aircraft Propulsion

Recent developments in high-efficiency power electronics, electric machines, batteries, and other aviation technologies have allowed for an increasing degree of electrification in aircraft systems. In MEA, secondary systems are driven electrically rather

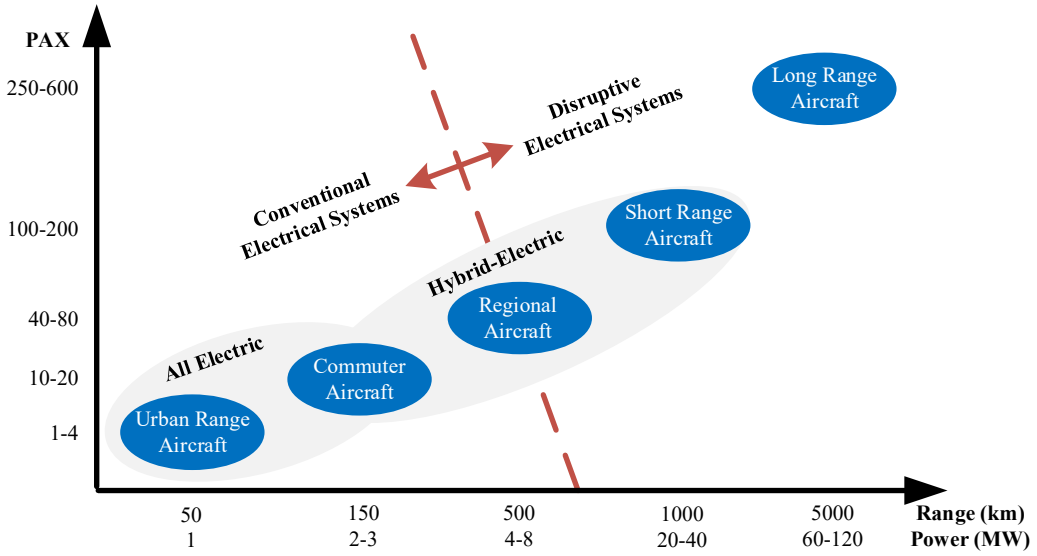

Figure 1.2: Evolution of aircraft electrical systems [21].

than pneumatically or hydraulically and offer significant benefits in terms of fuel burn and acoustic noise reduction. In HEA, battery energy storage is used in combination with jet fuel engines to power the propulsion systems, providing further reduction in fuel burn and emissions. Turboelectric aircraft use the internal combustion engine to drive a generator, powering propulsion through more efficient electric motors. Finally, AEA propulsion is powered entirely by battery energy, with the potential to completely eliminate emissions on short-range, low-payload flights. In this section, each of these categories are discussed, along with industry demonstrations for each concept where available.

1.2.1 More Electric Aircraft

More Electric Aircraft can be defined as aircraft that have a larger percentage of secondary systems powered electrically than traditional aircraft. In traditional aircraft, many systems are powered through hydraulics or pneumatics. In MEA, auxiliary systems are powered electrically using engine-driven generators and onboard power electronics.

The power electronics in MEA perform the appropriate energy conversion and power management from the generators, then distribute that power to separate AC/DC busses. Several voltage levels must be regulated by the onboard power electronics to meet the needs of the various auxiliary loads. A typical architecture for the electrical system in a MEA is shown in Figure 1.3.

Existing MEA in industry have shown that electrification of aircraft systems can reduce fuel burn, operation cost, and acoustic noise compared to conventional aircraft [7, 22]. Several MEA are operational today, including the Boeing 787, Lockheed Martin F-35, and Airbus A380.

1.2.2 All-Electric Aircraft

The propulsion system in an AEA is powered entirely by electricity and does not require jet fuel. Energy is stored in a battery pack, which is used to drive the propulsion motors of the aircraft. A diagram of an all-electric propulsion system is shown in Figure 1.4. While all-electric aircraft are best suited to eliminate emissions and decrease acoustic noise in aviation, the payload of such aircraft is significantly constrained by the energy density of battery technology. Currently, state of the art Lithium-Ion batteries have a specific energy density of about 250 Wh/kg, while the energy density of jet fuel is 12,000 Wh/kg – nearly 50 times greater [23, 24]. Even emerging battery chemistries such as Lithium Sulfur only offer an improvement of about two times that of Lithium-Ion at 450 Wh/kg [25]. The effect of the lower energy density is offset slightly by the gains in overall system efficiency when compared to traditional aircraft. The efficiency of the drive system of an AEA is about 80%, while overall efficiency for a gas turbine is roughly 40% [26].

However, battery storage is still far from being a replacement for jet fuel in terms of energy density. This limitation constraints all-electric aircraft to small urban air taxis –

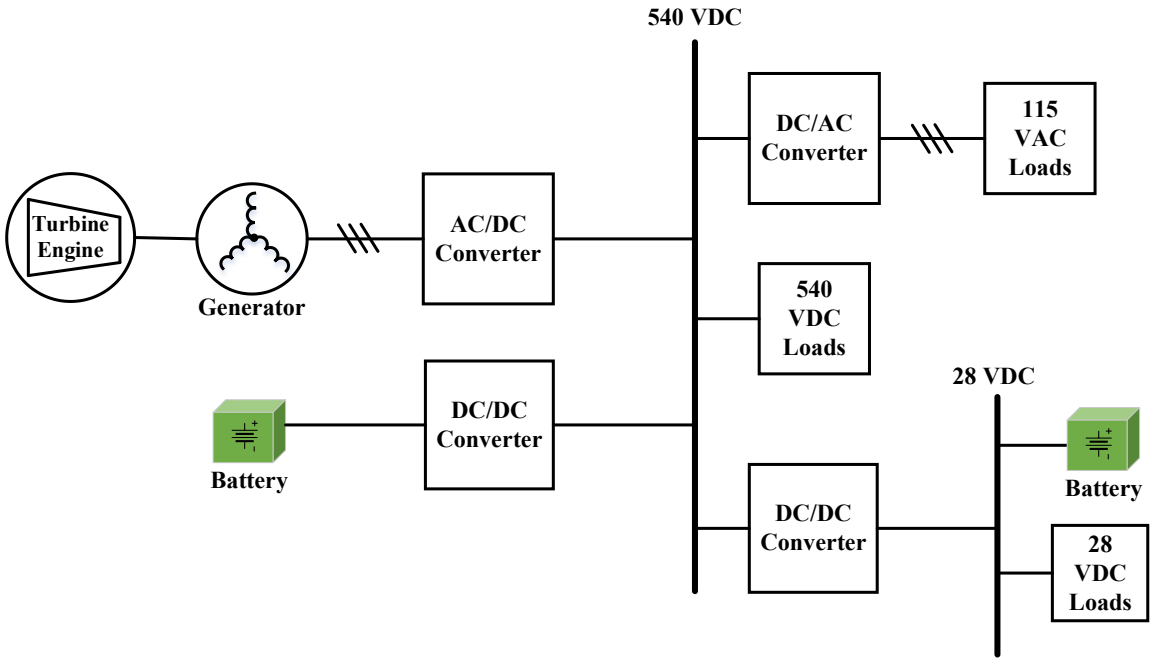

Figure 1.3: HVDC system of a More Electric Aircraft [27].

for larger or longer-range aircraft it will be necessary to develop hybrid-electric propulsion systems that can draw power from both battery storage and jet fuel.

Several industry R&D demonstrations from companies like EHang, MagniX, Joby Aviation, etc. have been performed showing the efficacy of all-electric propulsion systems. In addition to demonstrations, business partnerships with aviation companies are accelerating the development of electric vertical takeoff and landing (eVTOL) air-taxis to deploy in congested urban areas. Uber and Joby Aviation plan to deploy their Uber Elevate program as early as 2023, which could make all-electric air travel a reality in the near future [28].

1.2.3 Parallel-Hybrid Aircraft

Hybrid-electric aircraft are the most promising concept for wide-body passenger aircraft and have the potential to significantly reduce emissions and acoustic noise of regional air travel. In general, HEA can be organized into two different categories

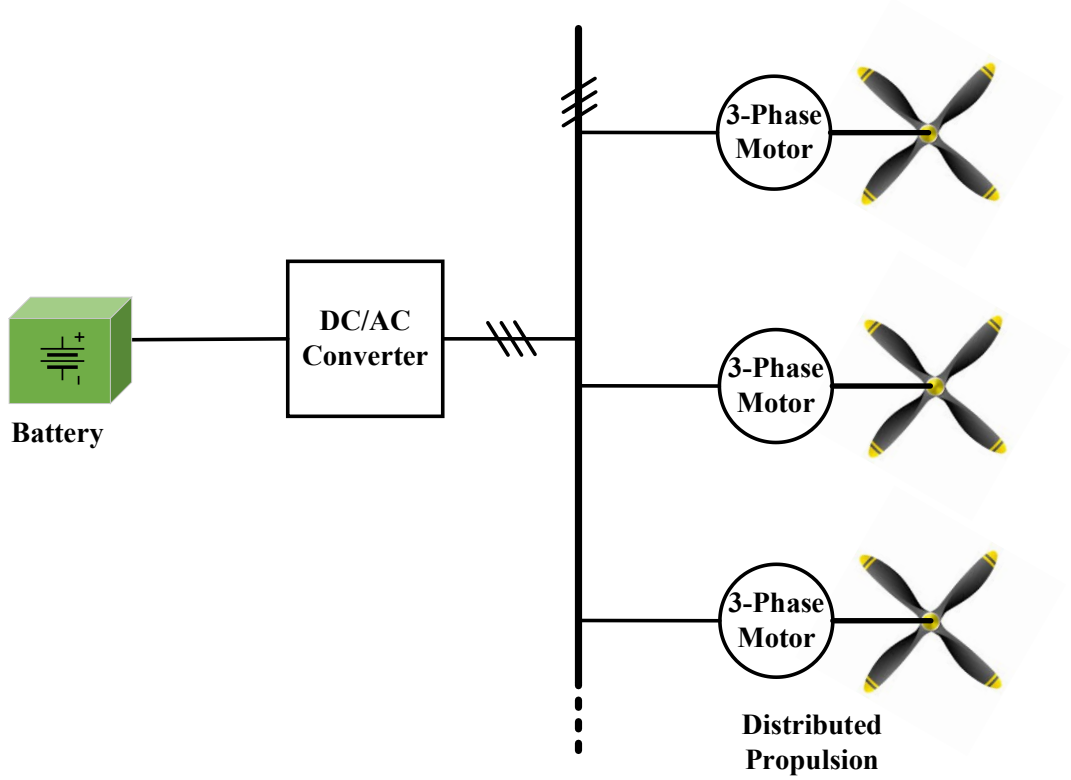

Figure 1.4: Electrical diagram of an all-electric aircraft propulsion system.

depending on the power distribution architectures: parallel-hybrid and series-hybrid. Series-hybrid architectures will be discussed separately in Section 1.2.4.

A typical powertrain for a parallel-hybrid aircraft is shown in Figure 1.5. In a parallel-hybrid, battery and fuel power are transferred to a shared mechanical output. Battery power is used to drive an electric motor, which is mechanically connected to the shaft of a fuel-powered turbofan, powering the propulsion fan in tandem. The parallel-hybrid architecture often requires fewer propulsion devices when compared to the distributed propulsion schemes that are common with all-electric and series-hybrid architectures. One challenge of the parallel-hybrid propulsion is that the speed of the propeller is not always the optimal speed of the engine. A continuously variable transmission may be required with some parallel-hybrids for independence between the

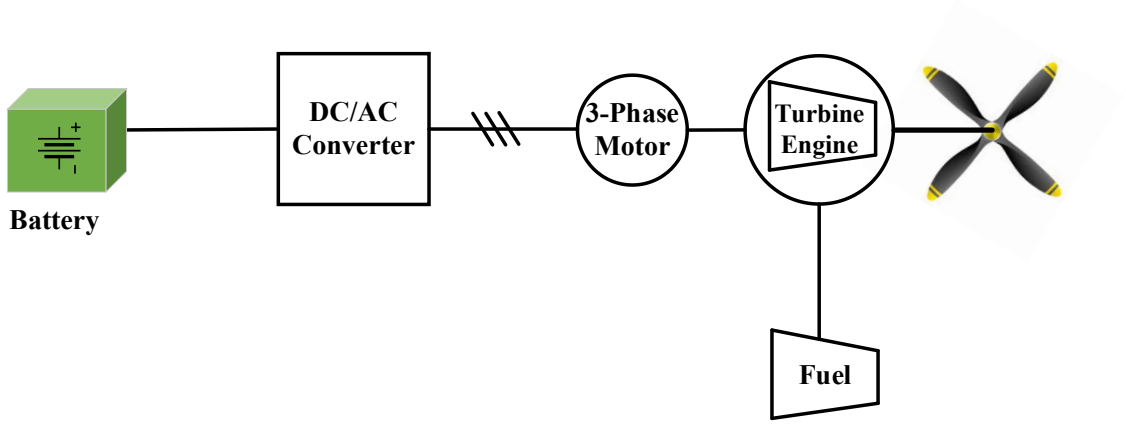

Figure 1.5: Electrical diagram of a parallel-hybrid propulsion system.

rotational speed of the engine and the propeller, which could reduce range and efficiency due to the additional weight [29].

The parallel-hybrid is generally regarded as a near-term option for electrified propulsion and has seen successful flight demonstrations, including one from Ampaire Inc. with 160 kW of onboard power [30].

1.2.4 Series-Hybrid Aircraft

The series-hybrid approach uses a fuel powered turboshaft to drive a generator, which supplies an electric bus with power. Also connected to the electric bus is a battery energy storage system. The propulsion motors can draw power from both the engine-driven generator and the battery storage system – interfacing the two sources to a common output requires an efficient and compact power converter. An illustration of the series-hybrid powertrain is given in Figure 1.6.

The current state of series-hybrid aircraft is largely conceptual, and future development will be dependent on the development of battery technologies and potential

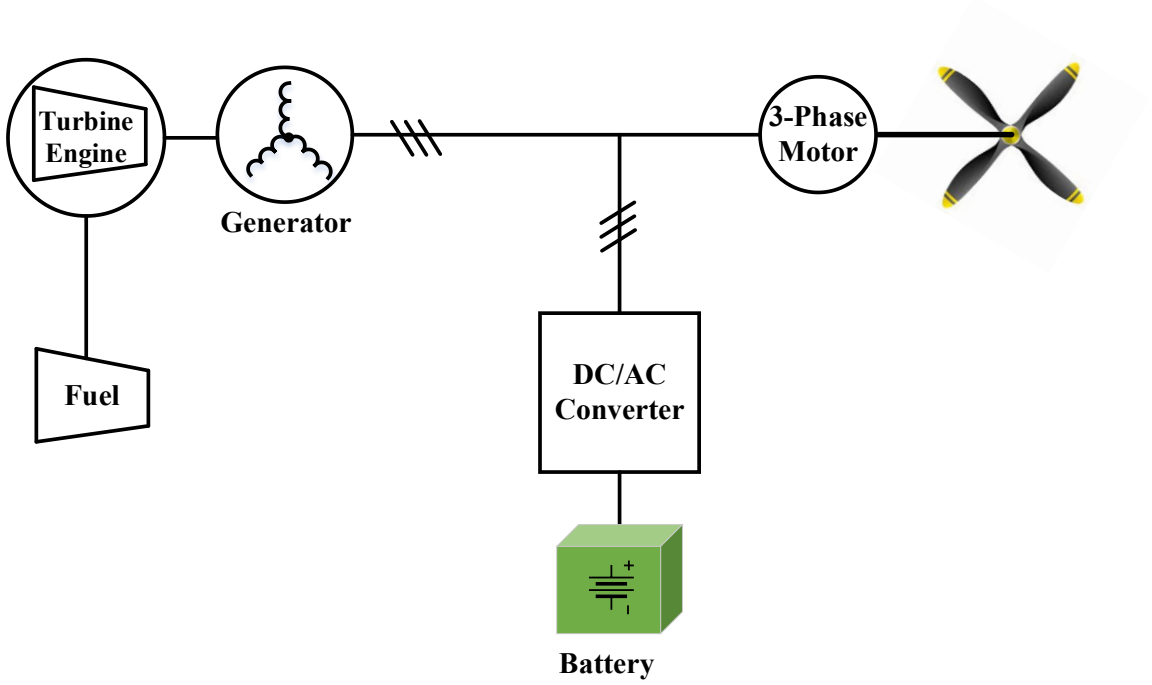

Figure 1.6: Electrical diagram of a series-hybrid propulsion system.

integration of renewable energy sources such as solar panels [31]. That said, small-scale series-hybrid demonstrations have been performed, such as the DA36 E-Star developed by Siemens AG, Diamond Aircraft and EADS. Siemens estimates that in the future, this concept could reduce fuel burn and emissions by up to 25% [32].

1.2.5 Turboelectric Aircraft

Turboelectric aircraft are similar in concept to the series-hybrid, but rather than supplementing the electric bus with battery power, the propulsion fans connected to electric machines which are exclusively powered by a generator driven by an internal combustion engine. The layout of the turboelectric drivetrain can be seen in Figure 1.7. Like the series-hybrid, turboelectric aircraft may also require a compact and efficient power converter for distribution if the concept is designed to utilize multiple generators. Along with the parallel-hybrid concept, turboelectric aircraft are a near-term option for electrified

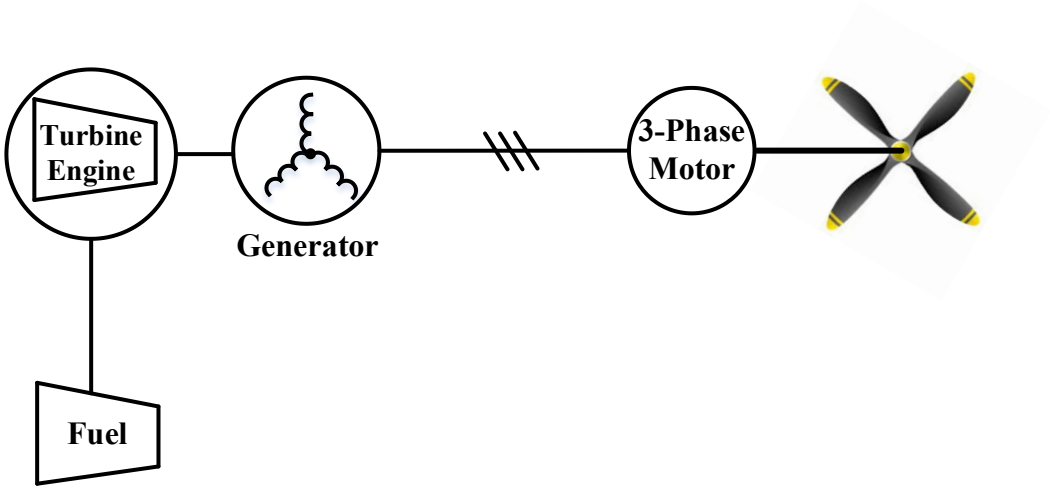

Figure 1.7: Electrical diagram of a turboelectric propulsion system.

propulsion. NASA has developed several wide-body turboelectric concepts and estimates fuel burn reduction at 7-12% using conventional jet fuel, although in combination with future technologies estimates reach up to 70% [33, 34].

1.2.6 Industry R&D Demonstrations

Several industry demonstrations have been performed to gain an understanding of real-world benefits and challenges of electrified propulsion. Current flight demonstrations largely consist of small all-electric aircraft. Since hybrid topologies are generally considered for larger, higher power passenger aircraft, the timeline for R&D is longer and most current demonstrations are limited to testbeds or scaled down systems on small aircraft. This section summarizes several industry demonstrations of electrified propulsion and examples of specifications and intended markets, when available.

Several companies are currently focused on developing electric aircraft for short-range, limited payload flights. Most emerging development is focused on small eVTOL aircraft. For example, EHang is developing an autonomous aerial vehicle aimed to transport passengers in highly congested cities. EHang estimates the range of their aircraft

at 35 km at its maximum payload of 220 kg, and completed autonomous trial flights in Japan in 2021 [35, 36].

Joby Aviation is another company focused on the development of air taxis and has partnered with Uber to carry out the aircraft design for Uber Elevate. Joby recently performed a flight demonstration as part of a press release video and estimates a range of 240 km on one charge, with capacity for four passengers [37]. According to the patents filed, each of the 6 motors on Joby's eVTOL will be rated to at least 130 kW, but normal operation is expected to be closer to 50 kW per motor [38].

Another significant developer in the eVTOL space is BETA Technologies, who plans to offer both cargo and passenger versions of their ALIA-250c aircraft. The ALIA-250c is expected to have a range of 250 miles, has been successfully flight tested, and has orders from both UPS and the United States Air Force [39, 40].

One electric aircraft company that is not focusing on eVTOL technology is magniX. MagniX develops electric propulsion units for aircraft, and currently offers propulsion units with motors rated at 350 kW and 640 kW [41]. They have performed flight demonstrations with electric propulsion retrofits of traditional aircraft. Their retrofitted Cessna 208B was the world's largest all-electric airplane at the time of its flight demonstration and was equipped with a 250 kW motor, with a maximum range of 100 miles [42].

While hybrid-electric aircraft have fewer full flight demonstrations, several important developments have been made in recent years by NASA, GE, Rolls-Royce, etc. In 2017, Airbus and Rolls-Royce launched the E-Fan X demonstrator concept. The demonstrator was to be outfitted with a series-hybrid propulsion system consisting of a

generator, one of four jet engines replaced with a 2 MW electric motor, and a 3 kV DC power distribution system [43]. The project was cancelled in April 2020, but Airbus and Rolls-Royce claim that they have a more focused vision of their hybrid-electric flight projects going forward.

In 2019, NASA and GE announced a partnership to develop a 1 MW Silicon Carbide (SiC) power inverter for commercial aircraft, and plan to move towards building and testing altitude-ready power inverters after testing on the ground [44].

In 2021, Honeywell and Rolls-Royce both unveiled high-power generators meant for hybrid-electric propulsion systems. Honeywell's 1 MW generator is capable of running on biofuel and can provide power for multiple electric motors depending on the needs of the aircraft [45]. Meanwhile, Rolls-Royce has begun testing of a 2.5 MW generator on a newly renovated testbed, bringing together the generator and a 3 kV power electronics system to test full system functionality [46, 47].

While most hybrid-electric aircraft development remains in the early stages, there have been successful flight demonstrations of hybrid-electric propulsion technology. In November 2020, Ampaire held a 20-minute demonstration flight of the Electric EEL – a Cessna 337 retrofitted with a parallel-hybrid propulsion system. The Electric EEL can hold 3 passengers or 450 lbs. of cargo, with over 200 miles of range [48]. The propulsion system combines a 300 hp engine with a 160 kW electric propulsion unit to achieve a 50% reduction in fuel burn and emissions [49]. Ampaire is also developing aircraft for regional flights and larger concepts with NASA and ARPA-E.

A summary of the aircraft and demonstrators discussed in this section is shown in Table 1.1. Because information is largely only available through press releases, the units and lists of specifications vary for each aircraft. Unavailable information has been omitted.

1.3 Multi-Port DC-DC Power Converters

Of the general topologies for electrified propulsion, series-hybrid and turboelectric show the most promise for future wide-body airplane designs. While a series-hybrid approach is assumed for this work, both system architectures will require a compact and efficient power converter to distribute and manage the power between sources and loads.

Recall that in a series-hybrid propulsion system, a generator and battery pack are used to supply power to the propulsion motor. To interface the fuel-powered generator, battery storage, and the load, it is necessary to develop a power converter solution capable of exhibiting high efficiency, high power density, high reliability, and flexible energy control. Generally, there is a tradeoff between power density, reliability, and control flexibility. The inclusion of a transformer can increase reliability through galvanic isolation but may lower the power density in the process. Using power diode based multi-pulse

Table 1.1: Aircraft electrifications

Aircraft	**Classification**	**Range**	**Payload**	**Rated Electrical Power**	**Max. Rated Voltage**
Boeing 787	MEA	N/A	N/A	1.45 MW	540 VDC
Ampaire Electric EEL	Parallel-Hybrid	321 km	204 kg	160 kW	
Airbus Rolls-Royce E-Fan X	Series-Hybrid			2 MW	3 kV DC
magniX eCaravan	All-Electric	160 km		250 kW	500-800 VDC
Joby Aviation	eVTOL (All-Electric)	241 km	4 PAX	6x130 kW	
BETA Alia-250c	eVTOL	402 km	5 PAX		
EHang AAV	eVTOL	35 km	220 kg		

rectifiers rather than active switching devices can increase power density and lower the complexity of the control design but comes at a cost of control flexibility since diodes are uncontrolled devices and there is no control of the rectified DC bus voltage. The goal in selecting a converter is to find a balance between these parameters that is suitable for use in an aviation power system.

Current solutions to this problem in the literature consist of either separate power converters at each propulsion motor or the use of a high-voltage DC link to directly connect the energy sources to the load [50, 51]. By implementing a three port DC-DC converter, the need for separate power converters at each source or load is eliminated, resulting in fewer power conversion stages. Therefore, a multi-port DC-DC converter can achieve higher power density, lower losses, and lower cost than a comparable solution with multiple converters. Multi-port converters are typically derived from the switching cells of common two-port converters such as buck, boost, half-bridge, etc. The following sections will discuss four classifications of multi-port DC-DC converters – unidirectional, bidirectional, non-isolated, and galvanically isolated – and give examples of the advantages and disadvantages of each with respect to their application in hybrid-electric propulsion systems.

1.3.1 Unidirectional Multi-Port Converters

In a unidirectional multi-port power converter, there are one or more ports where the energy can only flow in one direction. This can be inherent to the topology, such as the single-ended primary-inductor converter (SEPIC)-based three-port converter proposed in [52] or can be achieved by using power diodes for rectification rather than active switching devices. The output port of a triple active bridge converter, for example, could be made unidirectional through the use of a diode rectifier. Note that this also tends to change the

control strategy of the converter since diodes are uncontrolled devices [53]. In general, unidirectional converters use fewer active switching devices, allowing for simple control and higher power density. That said, for a hybrid-electric propulsion system a bidirectional converter topology is required to maximize efficiency and flexibility. It can be useful in some scenarios, for example, to recharge the battery storage using power generated by other systems of the aircraft. For this reason, the converter topology must have bidirectional capability.

1.3.2 Bidirectional Multi-Port Converters

In a bidirectional multi-port converter, energy can be transferred in either direction at each port depending on the operating conditions. This allows for flexible energy management to charge and discharge energy storage in the system using the same converter. Bidirectional converters are often used in battery storage systems where regenerative battery charging is desired. As shown in Figure 1.8, many unidirectional converters can be converted to bidirectional by replacing diodes with active switches such as SiC metal-oxide-semiconductor field-effect transistors (MOSFETs), and vice versa.

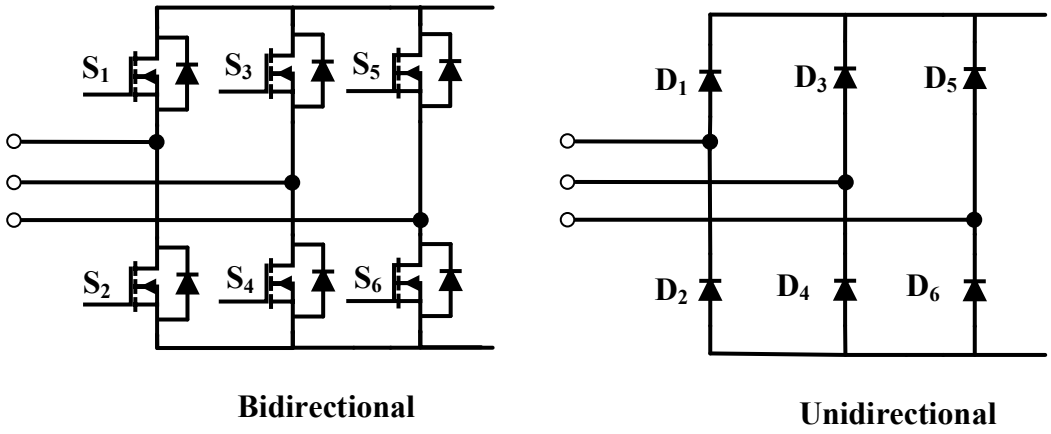

Figure 1.8: Bidirectional and unidirectional variants of a three-phase PWM rectifier.

Control of bidirectional multi-port converters is typically more complex than their unidirectional counterparts since there are more active switches. However, the main benefits yielding from bi-directional converters include the flexible control of the power flow and voltage levels.

1.3.3 Non-Isolated Multi-Port Converters

In non-isolated converters, all ports share a common ground and integrate the sources through a common DC bus without magnetic coupling [54]. In general, non-isolated multi-port converters provide excellent power density in terms of converter topology due to the absence of a bulky power transformer, but the auxiliary components required to achieve soft switching increase the device count considerably [55]. The switching electromagnetic interference (EMI) noise also tends to be higher in non-isolated converters, which may trip the microcontrollers and raise concerns about reliability [52]. Additionally, the inherent fault tolerance of non-isolated converters is low due to the common ground and has the potential to damage the rest of the system in the case of a fault. Therefore, while the power density, weight, and efficiency of non-isolated converters are favorable for aircraft propulsion, they are not suited for such a safety critical application.

1.3.4 Isolated Multi-Port Converters

In isolated converters, all sources and loads are galvanically isolated from one another using a power magnetic transformer, enhancing the reliability of the system when compared to non-isolated topologies. While the power density of such converters suffers from the inclusion of the transformer, the size of the transformer can be reduced by using a high switching frequency, which is feasible by leveraging the emerging SiC MOSFET devices. The transformer also allows for inherent soft switching operation in many isolated

DC-DC converter topologies due to the presence of the associated leakage inductance. Due to the soft switching operation, the dv/dt of the switching devices is significantly reduced, resulting in lower emissions of EMI. In hard switched, high-frequency switching of the semiconductor devices, EMI can cause several issues, and risks tripping the system microcontroller, saturating the filter inductors or capacitors due to pronounced leakage current. These issues can often be avoided with no extra cost in isolated converters.

This work proposes a bidirectional three port DC-DC converter that would eliminate the need for separate power converters at each source or load. Fewer stages in power conversion will result in lower power losses and a higher power density. Additionally, the proposed converter offers the benefit of galvanic isolation and improved reliability through the use of a high-frequency phase-shifting transformer and the associated AC link [54]. The triple active bridge (TAB) converter was chosen to meet the power, efficiency, and power density requirements for the hybrid-electric propulsions system.

1.3.5 Medium-Voltage Architecture

In addition to reliability, efficiency, and power density, the voltage and current stresses in the converter are an important consideration. To reduce cable weight and mitigate ohmic losses, electrical systems in aircraft have been trending towards higher AC-bus and DC-bus voltages. In conventional aircraft, typical voltage bus levels are a 3-phase fixed-frequency 115 V AC-bus, a 270 V DC-bus, and 28 V DC-bus [56]. In recent years, medium-voltage (MV) and high-voltage (HV) architectures have been introduced in the literature and in industry to achieve lower cable weight and higher power capacity [27]. Common MV architectures utilize 540 V DC-buses, or variable-frequency 230 V AC-

buses. HV systems under consideration often range from 1 kV to 3 kV DC, such as the testbed examples mentioned in Section 1.2.6.

This work is based on a series-hybrid system architecture that utilizes DC-bus voltages of 540 V, 800 V, and 1.2 kV – higher voltage levels than most electric propulsion architectures on the market. As a result, the switching devices in the specified power converter must be capable of tolerating these voltage levels. Compared to other topologies such as the triple-half-bridge, the TAB has lower current stresses on each switch. To minimize the weight and physical dimensions of the phase shifting transformer, commercially available SiC MOSFETs are used for higher switching frequency, yielding higher overall efficiency and power density. For this reason, the TAB was chosen for its power capacity and low switching stresses.

1.4 Review of Dual Active Bridge Converter

Since the TAB is a variation of the dual active bridge (DAB) converter, it is helpful to first review the fundamental principles of the DAB.

1.4.1 Circuit Description and Operating Principle

The DAB converter is an isolated, bidirectional two-port DC-DC converter characterized by two H-bridges and a transformer, with power transferred through the leakage inductance of the transformer. The typical topology of a DAB is shown in Figure 1.9 (a). Each H-bridge creates a square wave v_x on the windings of the transformer, with amplitude equal to the DC bus voltage V_x. The power flow is controlled by the relative phase shift between the voltages enacted on the transformer windings. Figure 1.9 (b) shows the equivalent circuit of a DAB, represented as two square wave voltage sources connected by a line inductance. Assuming a duty cycle of 0.5 and a constant frequency, the power

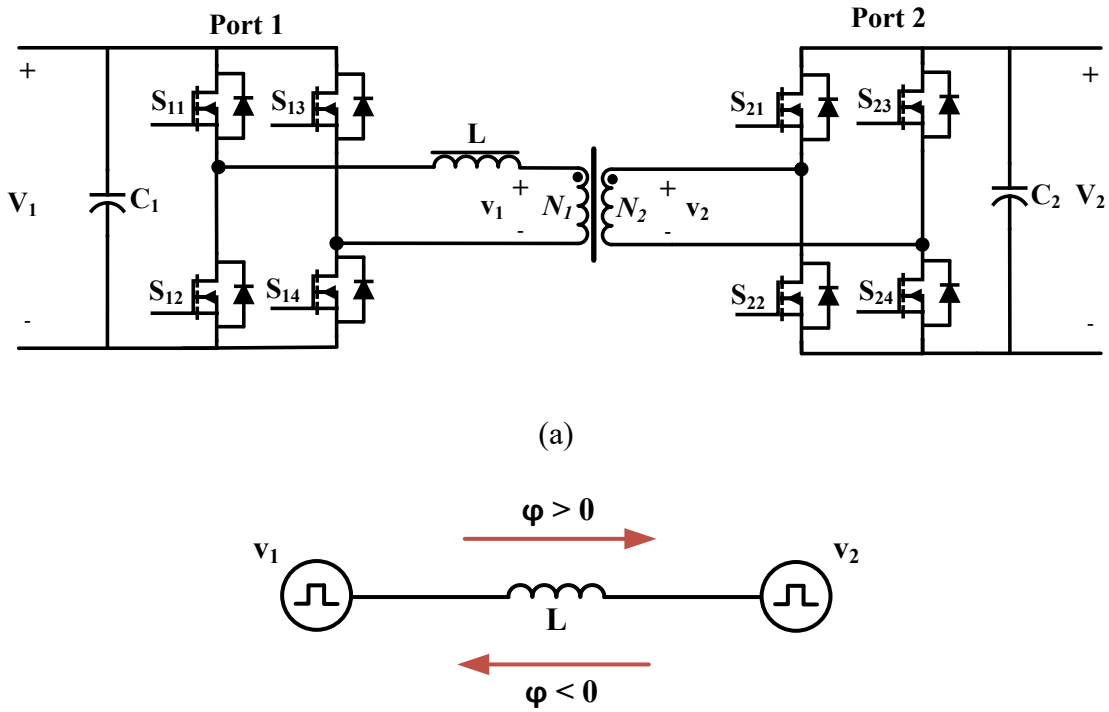

Figure 1.9: (a) Dual Active Bridge converter and (b) equivalent circuit [57].

transfer of the DAB converter is given by Equation 1, where φ represents the phase shift between ports, V_1 is the DC voltage of Port 1, V_2 is the DC voltage of Port 2, f_s is the switching frequency of the converter, L is the leakage inductance of the transformer, N_1 is the number of turns in the primary winding, and N_2 is the number of turns in the secondary winding:

$$P = \frac{V_1 V_2 \varphi (1-|\varphi|)}{2 f_s L} \frac{N_1}{N_2} \tag{1}$$

Note that the phase shift φ is the angle in degrees divided by 180. The direction of power flow can be reversed by simply reversing the phase shift between the two windings.

The switching sequence of the MOSFETs in each H-bridge is as follows: S_{11} and S_{14} turn on simultaneously, inducing a positive voltage V_1 on the primary transformer

winding. At the same time, S_{12} and S_{13} switch as the complement of S_{11} and S_{14}, turning off. After a half cycle, assuming a duty cycle of 0.5, S_{11} and S_{14} turn off and S_{12} and S_{13} turn on, applying a negative voltage -V_1 to the transformer. The switches in the output H-bridge switch in the same pattern, offset by phase shift φ.

While the voltage on the transformer can be thought of as a square wave applied by the switching of the converter, the current in the DAB is governed by the charging and discharging of the leakage inductance. Figure 1.10 gives an illustration of how the voltage and current waveforms in the converter vary over time. From t_0 to t_1, the current rises sharply from a negative value to a positive value as the positive voltage charges the inductor. When a positive voltage is applied to the secondary winding at t_1, the rise in inductor current continues, albeit slower than the first interval. At t_2, the primary-side H-bridge changes polarity, and a negative voltage is applied to the primary winding. As a

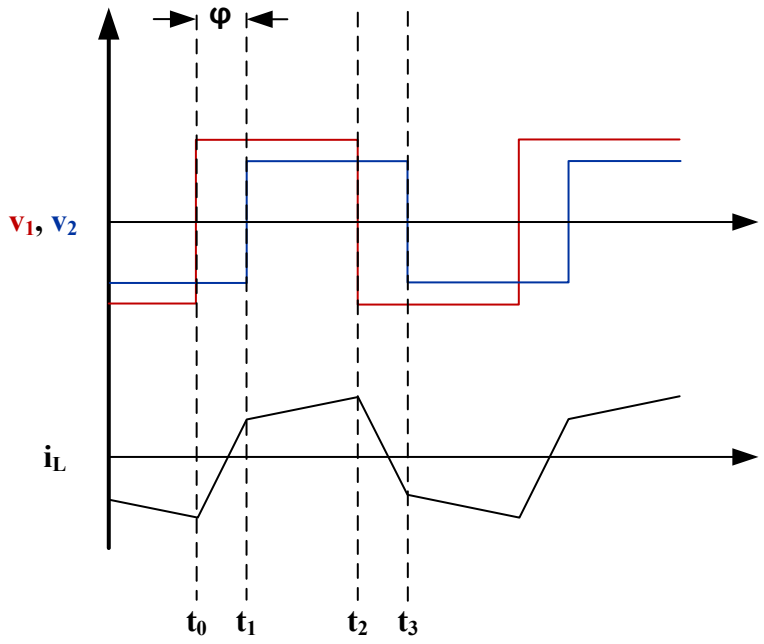

Figure 1.10: Current and voltage waveforms in a DAB converter using SPS control.

result, the current in the leakage inductance sharply decreases and negative current flow is observed. At t_3, the voltage on the secondary winding changes polarity and the decline in inductor current slows. The slope during each interval is proportional to the relative phase angle between each bridge.

The control strategy in Fig. 1.10 is called single phase shift (SPS) control, where the flow of power is dependent on a phase shift enacted between the ports of the converter. One inherent property of SPS control is reactive power in the circuit. When SPS control is used, the inductor current is reversed for a portion that transmits power backwards. This region is shaded in orange in Figure 1.11. Consequently, the forward current (shaded in gray) must increase to maintain positive power transmission [58]. The shaded areas in the figure are referred to as circulating current, or reactive current. This circulating current can result in lower system efficiency and large current stresses on the switches of the converter. In addition to reactive power, the natural soft switching capability of the DAB is limited

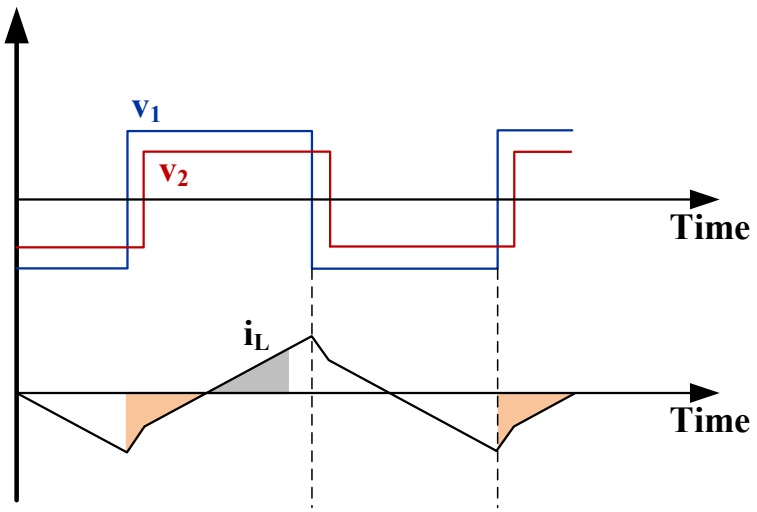

Figure 1.11: Reactive power in a dual active bridge converter [58].

when using SPS control, especially when voltage gain is away from unity or when variable-voltage input sources are used. Several alternative control strategies offer improved performance at a cost of control complexity. Dual phase shift (DPS) control introduces an additional phase shift between the diagonal switches (e.g., S_{11} and S_{14}). The resulting voltage applied to the transformer is the quasi-square wave shown in Figure 1.12. This significantly mitigates the reactive power and has been shown to improve dynamic performance and system efficiency in [59]. A similar quasi-square wave results from the use of PWM plus phase shift control, which is analyzed in [60] to extend the soft switching range for converters with widely varying input voltages. For simplicity of analysis, the remainder of this section will focus on a DAB converter with SPS control.

1.4.2 Control and Design Considerations

The primary component in the design of the DAB is the energy transfer element, namely, the leakage inductance of the transformer. By rearranging (1), we can calculate the leakage inductance required to achieve maximum power. For maximum power transfer P_{max}, the phase shift φ is assumed to be 0.5, which corresponds to a value of 90 degrees:

$$L \leq \frac{V_1 V_2 * 0.5(1-|0.5|)}{2 f_s P_{max}} \frac{N_1}{N_2} \tag{2}$$

The second consideration in the design of the DAB converter is the zero voltage switching (ZVS) turn-on soft switching capability. Since the ZVS range is limited, careful analysis must be performed to optimize performance and minimize losses in the system. To begin analyzing the ZVS range, ideal power devices are assumed, and the magnetizing inductance of the transformer is neglected. To achieve ZVS under these assumptions, the current must flow through the anti-parallel diode of the MOSFET during turn-on. That is [58]:

$$\begin{cases} i_L(t_0) < 0 \\ i_L(t_1) > 0 \end{cases} \tag{3}$$

At lower levels of output power, the positive charging interval of the leakage inductance does not have sufficient time for i_L to change from positive to negative. As a result, $i_2 < 0$ at time t_1 and soft switching is lost in the switches of the secondary port.

When considering the non-ideal conditions for ZVS operation, the parasitic capacitance of the switches must be considered in the analysis to avoid an over-estimation of the turn-off losses. The parasitic capacitance of each switch will be notated with the same subscript as the corresponding switch, i.e., C_{11} for S_{11}, C_{13} for S_{13}, etc. The inclusion

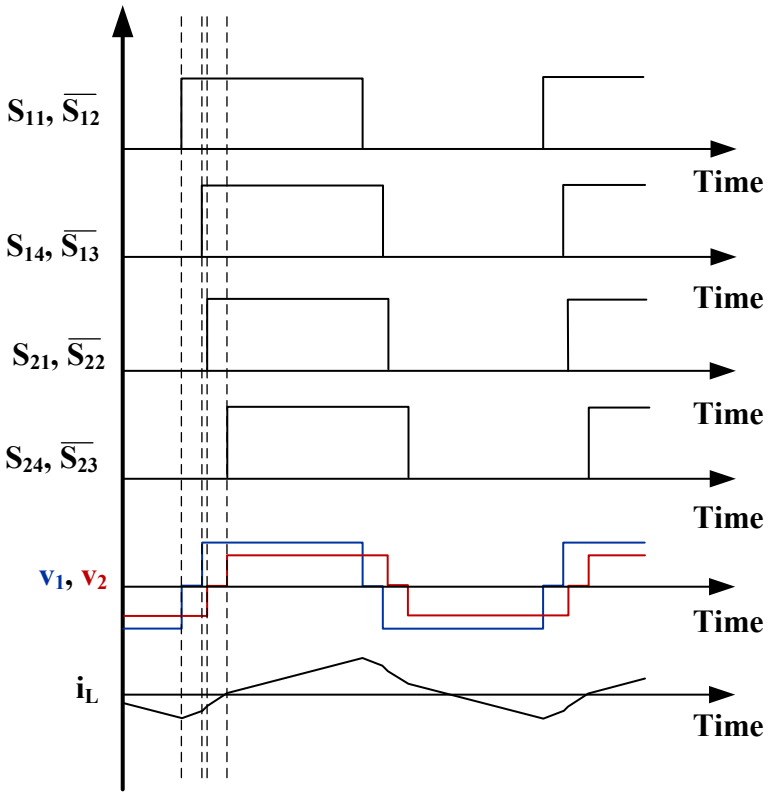

Figure 1.12: Waveforms in a dual active bridge converter using DPS control.

of capacitance in the analysis leads to greatly reduced, or even eliminated turn-off losses in the system. Without a parallel capacitor on each switching device, high turn-off losses can be observed that lead to lower efficiency and reliability and introduce EMI concerns. Without a capacitor, the voltage across the switching device will reach V_1 shortly after turn-off with a high dv/dt. The introduction of the parallel capacitor reduces this dv/dt by conducting current during turn-off. When S_{11} and S_{14} turn off, the current in the leakage inductance L discharges C_{12} and C_{13}, and charges C_{11} and C_{14}. This charging and discharging continues until their voltages reach that of the opposite rails, i.e. $+V_1$ in C_{11} and C_{14}, and 0 V in C_{12} and C_{13}. If the current is still positive at this point, the parallel diodes D_{12} and D_{13} turn on and clamp the voltage across each capacitor. The ZVS condition for transistor turn-off is given by the following [61]:

$$\frac{1}{2}Li_L{}^2 = 2\,CV_1V_2 \tag{4}$$

Equation (4) states that the energy stored in the inductance must be equal to the energy delivered to charge and discharge the device output capacitances. If the parasitic capacitance C of the switch is not sufficient, an external snubber capacitor can be placed in parallel to optimize the turn-off losses. In addition to capacitor sizing, the dead time between turn-on cycles must be sufficient to allow the capacitors to fully charge and discharge.

1.5 Applications of DAB and TAB Converters

Before describing the TAB converter in full detail, it is helpful to acknowledge the current applications of DAB and TAB converters in the literature. Since the TAB is a multi-port continuation of the DAB, their applications have historically been similar. DAB and

TAB topologies are often utilized in medium-voltage (MV) and high-voltage (HV) systems to transfer power between sources. Because of their bidirectional capabilities, the DAB and TAB are popular topologies for the integration of batteries, supercapacitors, and other energy storage systems.

The DAB has been used in several vehicle charging and grid applications. In [62], the authors propose a DAB converter to regulate the power between a solar photovoltaic system and a battery energy storage system. In [63], a DAB is used to interface a battery to the DC-bus of a hybrid fuel cell vehicle. [57] provides a reference design for a DAB converter in electric vehicle charging applications, using the bidirectional capability to advance vehicle-to-grid infrastructure.

DAB converters have also seen use in aerospace applications. In [64] and [65], the DAB is utilized in the distribution system of a more electric aircraft, transferring power between the 270 VDC and 28 VDC busses of the system. In [66], a thermal analysis is performed on a DAB used in a hybrid-electric aircraft propulsion system.

Similarly, the TAB converter has been used extensively in grid and hybrid vehicle systems – oftentimes to reduce the total number of conversion steps in the system. In [67], a TAB converter is used in a fuel cell hybrid vehicle to interface a supercapacitor and fuel cell to the load through a single converter. In [68], a TAB converter is proposed to interface a photovoltaic system with a battery energy storage system and a load. In one application, a TAB is utilized for a shipboard micro-grid system [69].

Once again in line with the DAB converter, the TAB has been utilized to distribute power in MEA systems, often to interface the ±270 VDC and 28 VDC busses to a battery bus [70]. Additionally, the review presented in [55] contends that the TAB is an ideal three-

port power converter for aviation power distribution systems. While the TAB converter has been proven in power distribution systems, work to demonstrate its potential in aircraft propulsion is limited in the literature.

1.6 Objectives

The objective of this work is to develop an efficient, modular, multi-port power converter with high power density that will meet the demands of voltage and current stresses typical of a hybrid-electric aircraft propulsion system. A series-hybrid propulsion system will be studied using a TAB converter to interface the generator DC-link, the battery energy storage system, and the DC-link of the electric propulsion motors. The TAB converter will be designed using commercially available SiC switching devices and a simulation model will be developed to analyze the electrical and thermal performance of the converter under steady-state conditions.

1.7 Thesis Outline

The thesis is organized as follows. In Chapter 1, background is given to the research motivation with descriptions of the impact of aviation on climate change, the current state-of-the-art in passenger aircraft electrification, and background on multi-port converters and their role in power systems with multiple sources.

In Chapter 2, the TAB converter is explained in detail including a description of the circuit topology, operating principle, control design, and motivation to use SiC switching devices. In addition, the modes of operation for the TAB converter are given for a typical hybrid-electric flight profile.

In Chapter 3, the concept of soft switching in TAB converters is introduced and discussed.

In Chapter 4, the modeling and simulation of the TAB converter are developed, including the modeling of the SiC devices, Lithium-Ion battery, and transformer. The simulation results are presented to demonstrate the efficiency and thermal performance of the TAB.

In Chapter 5, the work is concluded and future work on the hybrid-electric propulsion system is discussed.

CHAPTER 2. TRIPLE ACTIVE BRIDGE CONVERTER

2.1 Circuit Description

The full hybrid-electric aircraft propulsion system under study is given in Figure 2.1. A series-hybrid architecture is assumed, utilizing an onboard generator and battery storage system to deliver power to the propulsion motor load. The TAB converter is used to interface the power sources to the motor load with high power density and high efficiency while offering bidirectional power transfer [71]. The DC ports of the converter consist of a 540 V bus from the rectified generator output (i.e., Port 1), an 800 V bus from the battery storage (Port 2), and a 1.2 kV output to the propulsion motor drive (Port 3).

2.1.1 Circuit Topology

The dual active bridge converter was developed as a solution to bi-directional DC-DC power transfer. Its soft switching capability make it an efficient and cost-effective solution for renewable energy and microgrid applications, electric vehicle charging, etc. With the decreasing cost of energy storage solutions, many grid-tied and electrified vehicle systems have moved towards designs that utilize a combination of sources, using batteries or capacitors to supplement power from a primary source. To interface multiple sources to a load, multi-port conversion is more compact and efficient than several two-port conversion stages. As a result, the TAB is developed as a compact solution to transfer power across multiple DC buses.

One key benefit of the TAB is the modularity and scalability of the converter. While the proposed converter utilizes H-bridge switching cells at each port, several different switching cells can be used depending on the demands of the application. For lower power applications, half-bridges can be used to reduce component cost and converter size while

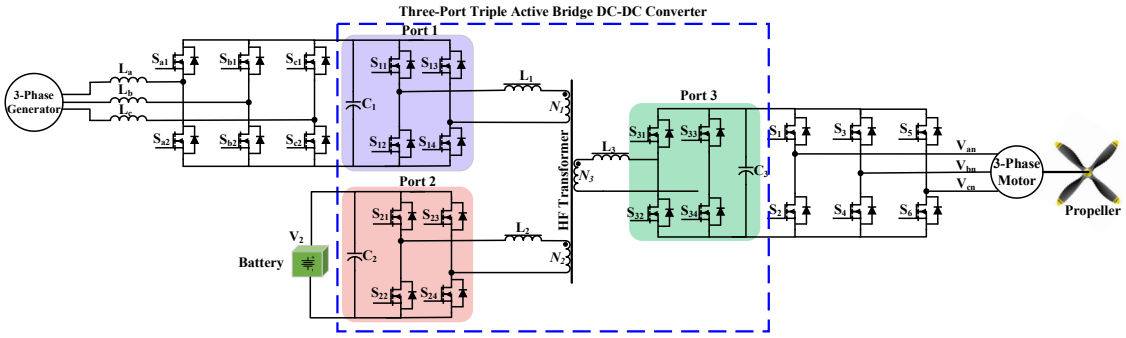

Figure 2.1: Series-hybrid aircraft architecture under consideration interfaced through a SiC TAB converter.

still offering the galvanic isolation and soft switching benefits of the TAB converter. Similarly, for ports that require higher voltage levels, neutral-point clamped (NPC) multilevel switching blocks or series-connected switching modules can be used to maintain rated operation of the switching devices.

Since the TAB is a three-port variant of the dual active bridge, many behavioral characteristics of the topology carry over, with an extra winding and H-bridge to accommodate the third port. The TAB converter interfaces the three H-bridge ports through a high-speed three-winding transformer. By using a high switching frequency, the size of the transformer can be reduced to maintain a high power density. Additionally, the use of Litz wire and a nanocrystalline core ensure highly efficient operation of the magnetic components of the converter.

2.1.2 Operating Principle

To analyze the TAB, a fully labeled diagram is given in Figure 2.2 (a). Much like the DAB, each H-bridge in the TAB converter generates a square wave voltage v_x on their respective windings. The power flow at each port is governed by the relative phase shifts in the converter, and energy is transferred through the leakage inductances of the

transformer. Unlike the DAB, the use of a three-winding transformer introduces tightly coupled power equations that complicate the control strategy. The equivalent circuit shown in Figure 2.2 (b) is the delta equivalent circuit of the TAB converter and is used to simplify analysis. The equivalent circuit inductance values L_{12}, L_{13}, and L_{23} can be calculated from the transformer leakage inductances L_1, L_2, and L_3 by the following [72]:

$$L_{12} = \frac{L_1L_2+L_1L_3+L_2L_3}{L_3} \tag{4}$$

$$L_{13} = \frac{L_1L_2+L_1L_3+L_2L_3}{L_2} \tag{5}$$

$$L_{23} = \frac{L_1L_2+L_1L_3+L_2L_3}{L_1} \tag{6}$$

There is one equation for each path of power flow shown in Figure 2.2 (b). The power in the converter can be described by the following, assuming SPS control and a duty cycle of 0.5:

$$P_{12} = \frac{V_1V_2\varphi_{12}(1-|\varphi_{12}|)}{2f_sL_{12}} \frac{N1}{N2} \tag{7}$$

$$P_{13} = \frac{V_1V_3\varphi_{13}(1-|\varphi_{13}|)}{2f_sL_{13}} \frac{N1}{N3} \tag{8}$$

$$P_{23} = \frac{V_2V_3\varphi_{23}(1-|\varphi_{23}|)}{2f_sL_{23}} \frac{N2}{N3} \tag{9}$$

$$P_1 = P_{12} + P_{13} \tag{10}$$

$$P_2 = -P_{12} - P_{23} \tag{11}$$

$$P_3 = -P_{13} + P_{23} \tag{12}$$

Power P_{ij} and phase shift φ_{ij} denote the power flow between ports *i* and *j* and the phase shift between transformer windings *i* and *j*, respectively. The phase shift variables φ_{ij} act as control variables for the converter power and are related by the following:

$$\varphi_{13} = \varphi_{12} + \varphi_{23} \tag{13}$$

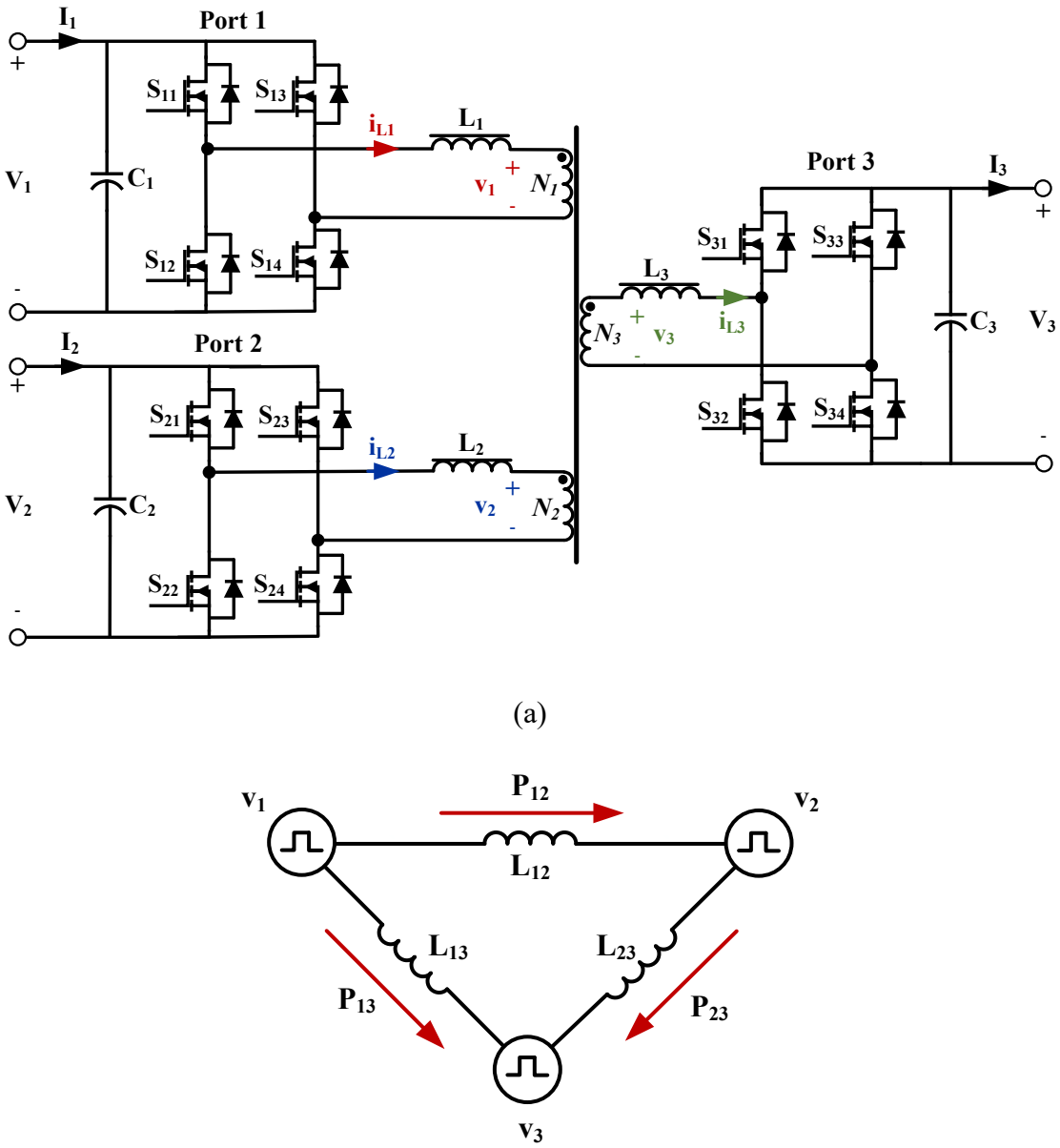

Figure 2.2: (a) Triple Active Bridge converter and (b) delta equivalent circuit of a TAB.

Control of the converter becomes problematic, however, since the power through each individual port (P_1, P_2, P_3) relies on two phase shift parameters. As such, changing the power in one branch of the converter will influence the other branches. To mitigate the tightly coupled power equations, [70] proposes a decoupling method in which one of the

power transmission paths is effectively eliminated from the equivalent circuit. If, for example, $L_{12} \gg L_{13}, L_{23}$, the power equations become:

$$P_1 = P_{13} = \frac{V_1 V_2 \varphi_{13}(1-|\varphi_{13}|)}{2 f_s L_{13}} \frac{N1}{N3} \tag{14}$$

$$P_2 = P_{23} = \frac{V_2 V_3 \varphi_{23}(1-|\varphi_{23}|)}{2 f_s L_{23}} \frac{N2}{N3} \tag{15}$$

$$P_3 = P_1 + P_2 \tag{16}$$

As a result, the coupling between the port power and phase shift angle is weakened. To decouple the power in practice, the leakage inductances of the transformer must meet the following condition:

$$L_3 \ll L_1, L_2 \tag{17}$$

By manipulating (14) and (15), the required values of the main transfer elements L_1 and L_2 can be estimated:

$$L_i \leq \frac{V_i V_3 0.5(1-|0.5|)}{2 f_s P_{max_i}}, \qquad i = 1, 2 \tag{18}$$

where V_i is the input DC voltage of port i; P_{max_i} is the maximum rated power entering or leaving the port; 0.5, equivalent to 90 degrees, is the phase shift value where the converter reaches maximum power transfer; and f_s is the switching frequency in Hz. L_3 is set to a value much less than L_1 and L_2 as described in [70]. From (18), note that a larger inductance would require a larger phase shift to deliver the same power. A large phase shift results in a higher circulating current, which motivates the use of a small leakage inductance in the design [73].

Like the dual active bridge, several modulation strategies are proposed to reduce circulating current, switching stresses, and losses in the converter. Reactive power is present in the TAB under traditional SPS control and can lead to less efficient operation,

especially in applications with large mismatches in source voltage. Once again, several methods have been proposed to mitigate reactive power and achieve gains in efficiency. In [72], a method is proposed that introduces additional passive components. The proposed blocking capacitor creates an infinite impedance between the source ports, creating an open-circuit path to block circulating current from flowing. Others propose novel control methods. In [60], a duty-cycle control similar to DPS is implemented to reduce reactive power and improve efficiency. In [74], a control method is proposed to intermittently operate the TAB as a DAB, turning off the gates of the power-transmitting bridges for a portion of the switching cycle. As a result, the circulating current is suppressed, and the author claims an overall efficiency increase of 2.5 percent. Compared to the DAB, there is an extra port and therefore an extra degree of control in the TAB converter, which leads to greater overall complexity in implementation. In this work, a SPS modulation strategy is used to simplify analysis while achieving high efficiency in the TAB converter.

An illustration of the voltage and current waveforms in the TAB using SPS control is given in Figure 2.3. With three unique leakage inductances, the flow of current in the TAB becomes more complex than its two-port counterpart. The appearance of the current waveforms in the converter will vary depending on the phase shifts in the converter. In Figure 2.3, the phase shift φ_{13} is greater than φ_{12}. From t_0 to t_1, the current through L_1 increases as a positive voltage is applied to winding 1. Meanwhile, the current through L_3 begins increasing at a quicker rate. From t_1 to t_2, the current in inductor L_2 rises, switching polarity. The current through inductor L_3 also switches polarity, rising more quickly than the previous interval. From t_2 to t_3, a positive voltage is applied to each winding. During

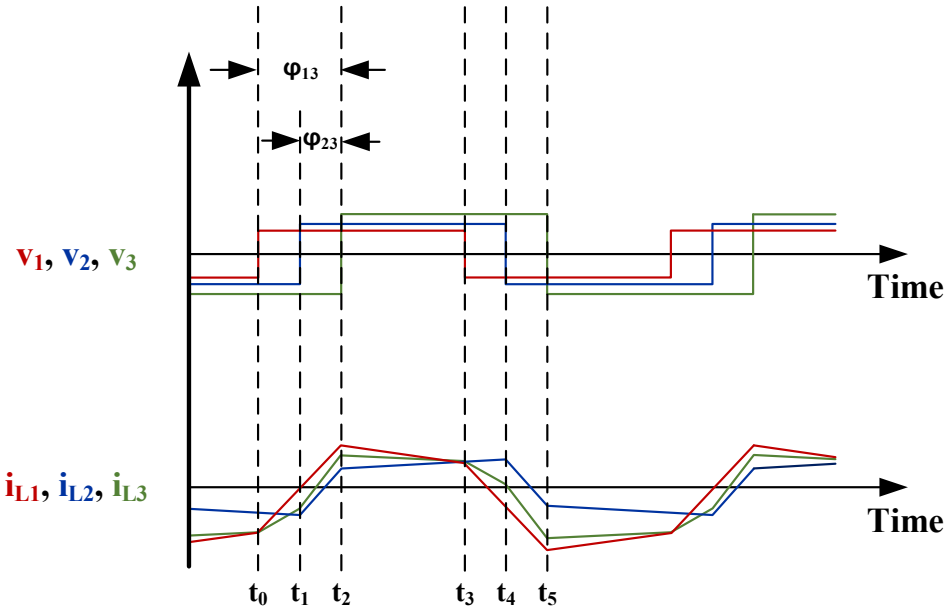

Figure 2.3: Current and voltage behavior in a TAB using SPS control when $\varphi_{13} > \varphi_{12}$.

this interval, currents i_{L_1} and i_{L_3} decrease slightly while maintaining a positive polarity. i_{L_2} continues to rise at a slower pace than the previous interval. From t_3 to t_4, v_1 switches to a negative polarity and i_{L_1} sharply decreases. i_{L_2} continues to rise at the same rate and i_{L_3} begins decreasing more sharply. From t_4 to t_5, v_2 switches polarity and i_{L_2} sharply decreases, going from positive to negative. i_{L_1} and i_{L_3} continue decreasing until reaching their peak negative values.

It can be shown that peak voltage across each switch x in a given port is equal to the DC-bus voltage of that port:

$$V_{in} = V_{S_{1x},S_{2x}} \tag{18}$$

$$V_{out} = V_{S_{3x}} \tag{19}$$

Equations (18) and (19), along with simulated current values, were used to choose the commercial SiC switching devices for the converter.

2.1.3 SiC Switching Devices

In the proposed converter, SiC MOSFETs are utilized to achieve lower losses and greater power density when compared to traditional silicon (Si) switching devices. Because of the lower on-state resistance $R_{ds(ON)}$, lower switching energies and faster switching speed of SiC devices, they can achieve lower conduction and switching losses. Additionally, SiC MOSFETs have nearly three times the thermal conductivity of comparable Si MOSFETs, meaning heat is easier to remove from the devices [75]. Combined with the lower thermal losses, the use of SiC enables more compact thermal management solutions, greatly improving the power density of the system. Another benefit over silicon switching devices is the capability to operate at higher switching frequencies – silicon devices cannot operate at the same energy levels at high switching frequency [76]. Higher switching frequencies allow for more compact sizing of magnetic components such as the three-winding transformer in the TAB. As a result, the size of the converter can be reduced significantly compared to a converter using Si devices. Finally, the higher breakdown voltage of SiC allows for higher voltage systems, which can significantly decrease cable weight throughout the aircraft. The material advantages of SiC over Si devices for high temperature, high voltage, and high frequency applications are summarized in Fig. 2.4.

In addition to the enhanced thermal performance and power density, SiC MOSFETs may provide enhanced reliability in high-altitude aviation applications. Cosmic radiation has been shown to cause spontaneous failures in semiconductor power devices. These spontaneous events are called Single Event Burnouts (SEB). The probability of SEB depends on both the intensity of the cosmic radiation and the electric field applied to the

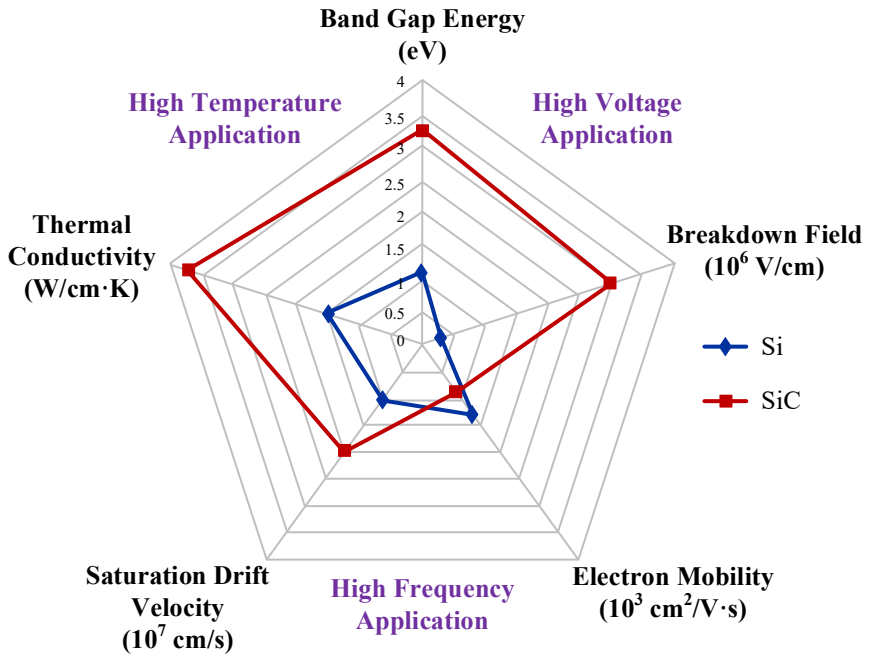

Figure 2.4: Performance comparison between Si and SiC switching devices [77].

semiconductor device [78]. The altitudes typical of passenger aircraft have significantly higher amounts of cosmic radiation than at sea level. It is estimated that exposure to cosmic radiation doubles for every 4,500 feet of increasing altitude [79]. Commercial aircraft commonly cruise around 36,000 feet. Thus, the switching devices used in high-altitude applications like passenger aircraft must be highly reliable and resilient to the effects of cosmic radiation. A common technique to manage SEB in Si devices is to de-rate the switching devices by lowering the voltage or using multiple devices in series. However, the decrease in power density is undesirable for aviation applications.

SiC devices have been shown to consistently have lower rates of SEB failure than comparable Si devices [80-83]. In [81], a comparative study is performed to analyze the difference in robustness between Si and SiC switching devices when subjected to cosmic radiation. The authors conclude that the SiC devices are more robust and may allow for

less de-rating than Si-based designs. As a result, SiC devices are more well-equipped for reliable and compact high-altitude operation.

Another consideration in the converter design is the degradation of dielectric insulation at high altitudes. In high-voltage designs, air acts as a dielectric insulator. At high altitudes, air pressure is lower, reducing the effectiveness of air's insulating effect. Paschen's law relates the breakdown voltage in a gas to the ambient pressure and the distance between two electrodes – the resulting relationship can be seen in Figure 2.5. Air pressure at sea level is equal to 14.7 psi. At a typical cruising level of 36,000 feet, it is reduced by roughly 88% to 3.3 psi. As a result, the breakdown voltage of air is decreased

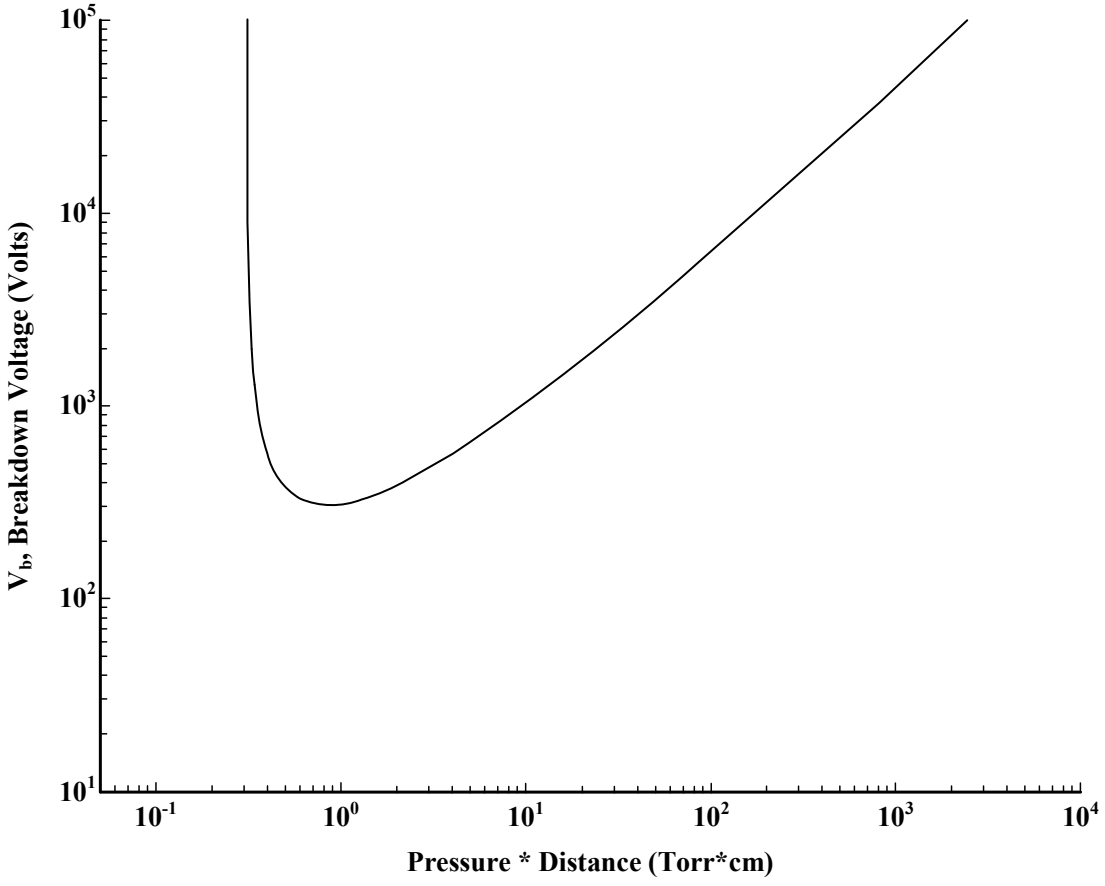

Figure 2.5: Paschen curve for air [84].

and physical spacing between high-voltage lines must be increased to prevent arcing and ensure safe operation. The resulting converter will typically be larger than a comparable converter for terrestrial applications, with more conservative voltage ratings to avoid the risk of failure.

2.2 Operation Modes in Hybrid-Electric Flight

To simplify analysis of the TAB converter for the proposed application, three modes of operation are defined that correspond with a typical flight profile of a hybrid-electric aircraft. The following sections will describe the flight profile and define the direction of power flow and total power required in the converter for takeoff, cruising, and landing.

2.2.1 Aircraft Mission Profile

In defining the modes of operation in the converter we must first examine a typical mission profile for a hybrid-electric aircraft. Figure 2.6 describes the considered flight profile [85]. Peak power is drawn during takeoff, utilizing the rated 300 kW of the converter. While cruising, the aircraft requires about 33% of the rated power – in this case, 100 kW. Finally, during the descent phase, about 17% of the rated power is required to perform landing operations. During landing and ground maneuvering, it is possible to regain a small fraction of the expended power through regenerative operation, utilizing the bidirectional capability of the converter.

2.2.2 Takeoff – Mode 1

Defined as Mode 1, the takeoff phase requires the full power operation of the propulsion drive. In this mode, both the generator and battery will power the load. In the proposed converter, a rated power of 300 kW is delivered to the propulsion motor load. Of

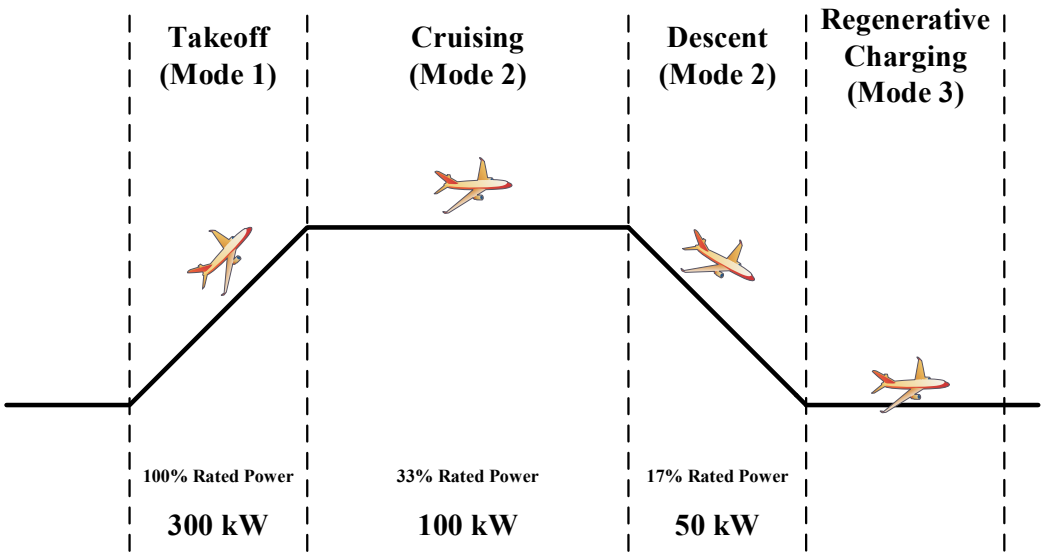

Figure 2.6: Aircraft mission profile under study [85].

this 300 kW, 100 kW is supplied by the onboard generator, while 200 kW is supplied by the battery storage to supplement the remaining power. The SiC switches in each port are controlled by two proportional-integral (PI) controllers to determine the required phase shifts and resulting gate signals, and power is transferred from the generator and batteries to the load by phase-shifting the gate signals of Ports 2 and 3 relative to Port 1.

2.2.3 Cruising and Descent – Mode 2

During the aircraft cruising mode, only the generator provides 33% of the rated motor power to the propulsion fan load. In this mode, the TAB converter supplies 100 kW to the propulsion motor. In descent, the operation of the converter is identical, but the required power is half that of the power while cruising. In descent, 50 kW is transferred from the generator to the propulsion motor. The Port 2 H-bridge switches are turned off in Mode 2 to prevent power flow to or from the batteries, and the TAB acts as a DAB converter. During this mode, a single PI controller is used to determine the phase shift φ_{13} required for the demanded power.

2.2.4 Regenerative Charging – Mode 3

It is generally accepted that unlike electric ground-vehicles, electric and hybrid-electric aircraft can only regenerate a very small fraction of the total power expended. During the descent phase, it is estimated that the regenerative or windmilling operation of unused propulsion motors can be harnessed to regain roughly 5% of the aircraft's potential energy [86, 87]. Additionally, developments in the literature suggest that regenerative braking during runway taxiing can be utilized to regain expended energy [88]. Therefore, to minimize charging cost and wait time, the power available at Port 3 can be transferred through the converter to charge the battery. In this mode, a 90-degree phase shift is enacted between Ports 2 and 3 such that any available power is transferred completely to the battery pack. The power in this mode depends on several internal and external physical factors that affect the back electromotive force (EMF) of the propulsion or landing gear motors, including the back-EMF voltage constant of said motors.

2.3 Closed-Loop Control

In a triple active bridge converter, closed-loop control is often necessary to regulate the power to and from each power port, especially in dynamic applications where the demand is constantly changing. At a minimum, the control system must be capable of regulating the power to and from each port of the TAB converter. The following sections will discuss the state of the art in the TAB control, the control system of the proposed controller, and how to achieve the phase-shift PWM gate signals for the MOSFETs in the TAB.

2.3.1 PI Control and Coupled Power Equations

In the TAB, a unique problem is presented in the coupled power equations of the system. From (7) – (12) it can be seen that by changing one phase shift in the converter, the power through each port is affected. Several novel methods to decouple the power equations have been proposed in the literature. In addition to the inductor sizing method discussed, there are multiple advanced control strategies to decouple the control loops.

The most common in the literature is the decoupling matrix method utilized in [89, 90]. A diagram for the decoupling matrix control is shown in Figure 2.7. In [89, 90], Ports 2 and 3 are both configured as outputs, with only Port 1 acting as a source. As a result, currents I_2 and I_3 are used as reference variables for the control system and the phase shifts φ_{12} and φ_{13} are adjusted accordingly. To implement decoupling matrix control, the transfer function of the system must be found first. This is the system matrix **G**, which outputs currents I_2 and I_3, for a given combination of φ_{12} and φ_{13}. Matrix **H**, the inverse

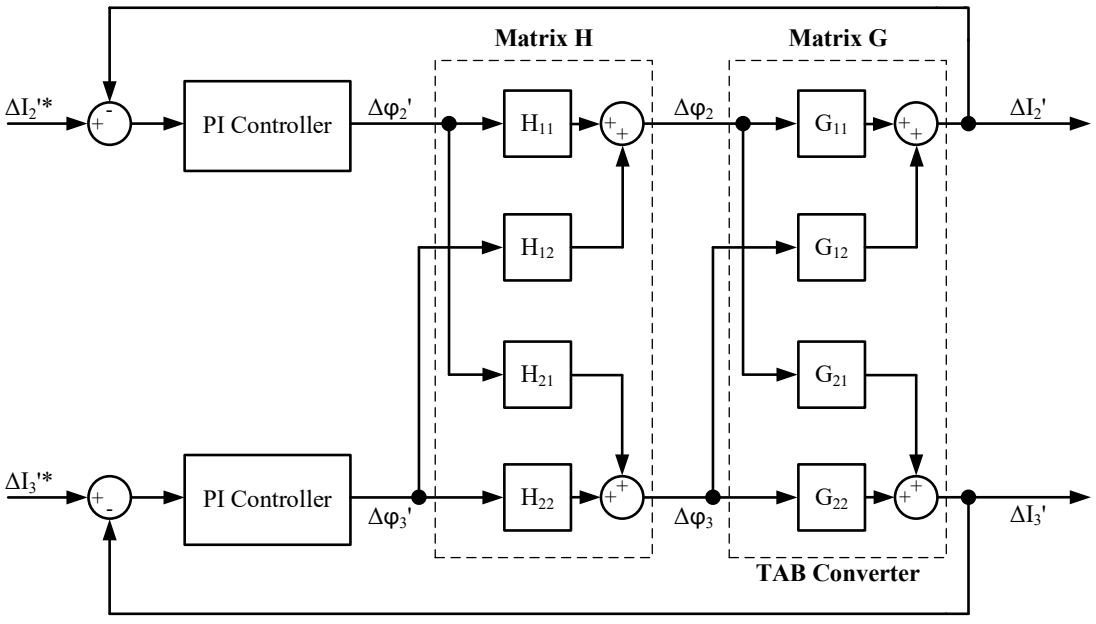

Figure 2.7: Block diagram of a decoupling matrix control system [90].

of **G**, is designed to diagonalize system matrix **G**. In doing so, the interference of φ_{12} on the φ_{13}-I_3 control loop and the interference of φ_{13} on the φ_{12}-I_2 control loop are eliminated [90]:

$$\begin{cases} \boldsymbol{X} = \boldsymbol{GH} = diag[x_1, x_2] \\ \boldsymbol{H} = \boldsymbol{G}^{-1} \end{cases} \tag{20}$$

While the decoupling matrix shows quick response time and stable operation, one drawback of the decoupling matrix is its limited operating range. To maintain linearity, the implementation depends on a lookup table with pre-defined operating points. If the requested operating point is too far from the pre-determined points in the lookup table, the control system sees a degradation in performance.

In [91], a novel feed-forward control method is proposed with decoupling capability at a wider operating range, and simpler implementation than the decoupling matrix method. Rather than pre-calculating the operating points of the converter, the feed-forward method mitigates the coupling interference across the operating range by using a combination of closed and open loops in the control. A diagram of the feed-forward control is shown in Figure 2.8. First, one closed loop of the TAB control system is converted to an open loop, using the Subsystem block to calculate the value of φ_{13} for a given reference I_3^*. The output of the feed-forward block is then added to the output of the PI controller, compensating for the interference of the φ_{13}-I_3 open loop on the closed φ_{12}-I_2 loop. While the feed-forward method offers satisfactory performance at a wide range of inputs, the design and implementation of the control blocks quickly becomes cumbersome and prone to mathematical error.

The decoupling method discussed in Section 2.1.2, which relies on the design of the converter such that $L_3 \ll L_1, L_2$, remains the most straightforward method to regulate

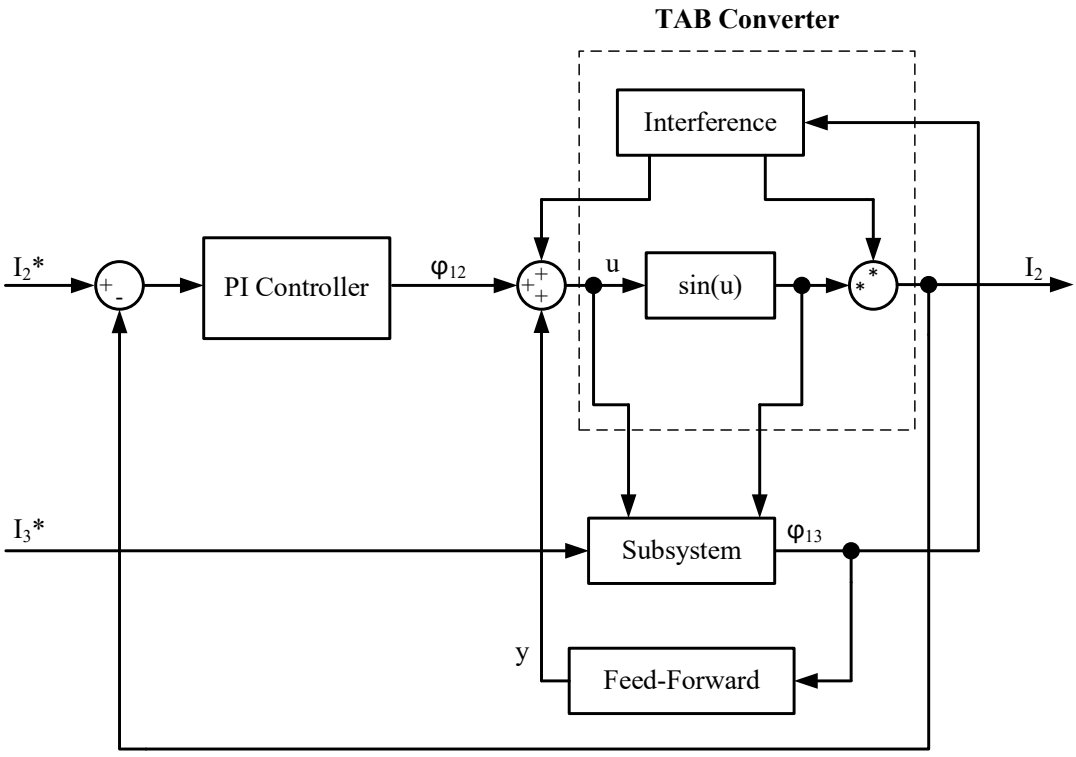

Figure 2.8: Block diagram of the novel feed-forward control method proposed in [91].

power in the ports of the converter. The control block diagram for the hardware decoupling method is shown in Figure 2.9. With the control loops decoupled through inductor sizing, the power at each port can be regulated with two PI controllers. Unlike the matrix decoupling, this approach is capable at wide operating ranges without pre-determined operating points. Each PI controller can be manually tuned for the performance needs of the application and specific TAB parameters.

2.3.2 Phase-Shift PWM

In active bridge converters, the main transfer element of the circuit is the leakage inductance of the transformer windings. As discussed in Section 1.4.1, the equivalent circuit of a DAB converter is analogous to the flow of power in an AC transmission line, modeled as two AC sources connected through a line reactance. As such, the simplest

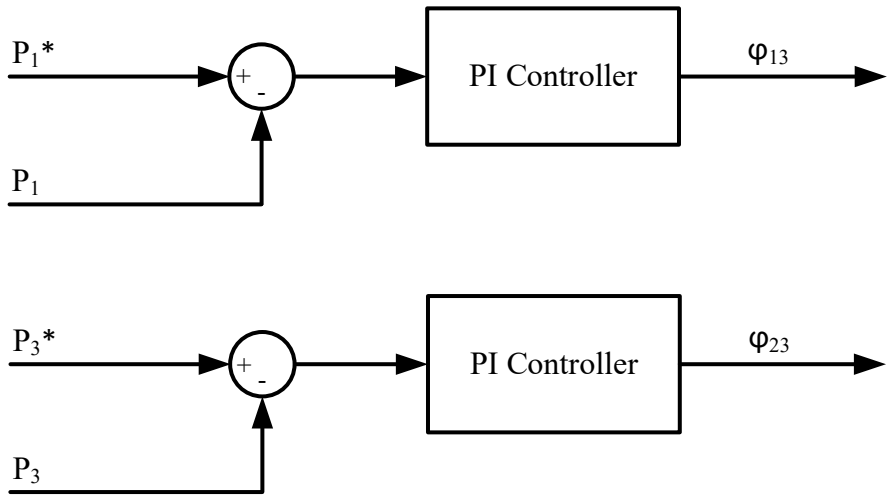

Figure 2.9: Block diagram of the control system utilized in combination with the hardware decoupling method proposed in [70].

approach to control the power in the converter is to introduce a phase shift between the voltages applied to the windings of the transformer. A block diagram of the phase-shift PWM is given in Figure 2.10. Note that although φ_{13} is output from the PI control system, φ_{12} is used to indirectly change φ_{13} since they are directly related. This does not adversely affect the power in the system since φ_{12} is no longer an influence on the equations of the circuit. Shifting the signals of Port 2 relative to Port 1 eliminates the need to implement a control system where Port 3's gate signals must be shifted relative to both Ports 1 and 2, keeping the control loops independent of one another.

The phase shifts generated by the PI controllers are input to the phase shifting blocks. The reference square wave signal is then shifted by the phase amount specified by the control system. The output of each phase shift block is sent to the gates of switches 1 and 4 of each H-bridge, then negated to generate the gate signals for S_{x2} and S_{x3}. Note that in practice a small dead-time must be introduced between the turn off of S_{x1} and S_{x4}, and

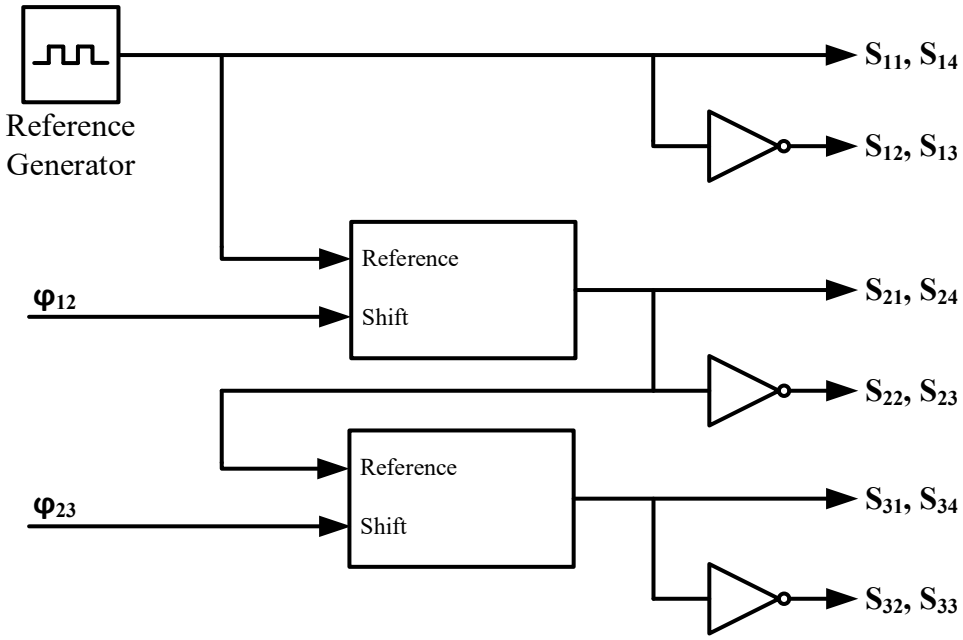

Figure 2.10: Generation of phase-shift PWM gate signals in the proposed converter.

the turn on of S_{x2} and S_{x3} to prevent DC-bus shoot-through and a subsequent short-circuit fault to the system.

CHAPTER 3. SOFT SWITCHING IN TRIPLE ACTIVE BRIDGE CONVERTERS

3.1 Concept of Soft Switching

In the switching devices of a power converter, the losses can be classified into two categories: switching losses and conduction losses. Conduction losses occur during device conduction and are proportional to both the duty cycle and the on-resistance of the MOSFET, R_{ds}. Switching losses, on the other hand, occur during the transition from ON to OFF and vice versa. Switching losses are dependent on the switching frequency of the converter and switching energies of the devices – higher switching frequencies translate to higher losses during hard switching.

As switching frequencies increase in modern converters due to the advent of wide bandgap semiconductors – primarily to reduce the size of magnetic components and increase power density – the associated switching losses must be reduced. One approach to reduce switching losses is the use of soft switching. In a switching device such as a MOSFET, the turn-off and turn-on transitions are not instantaneous. As such, the voltage and current through the switching device overlap during the transition period, as shown in Figure 3.1. The shaded portion of this overlap represents the switching loss dissipated during the transition.

In contrast, a soft switching converter avoids this overlap by switching only when either voltage or current are zero. During turn-on, the converter can operate in zero voltage switching (ZVS), where the switch is turned on while zero voltage is applied. Similarly, zero current switching (ZCS) can be utilized during turn-off to switch off while zero current is flowing through the switch. The voltage and current in a MOSFET during ZVS and ZCS soft switching can be seen in Figure 3.2. The matter of achieving ZVS or ZCS is

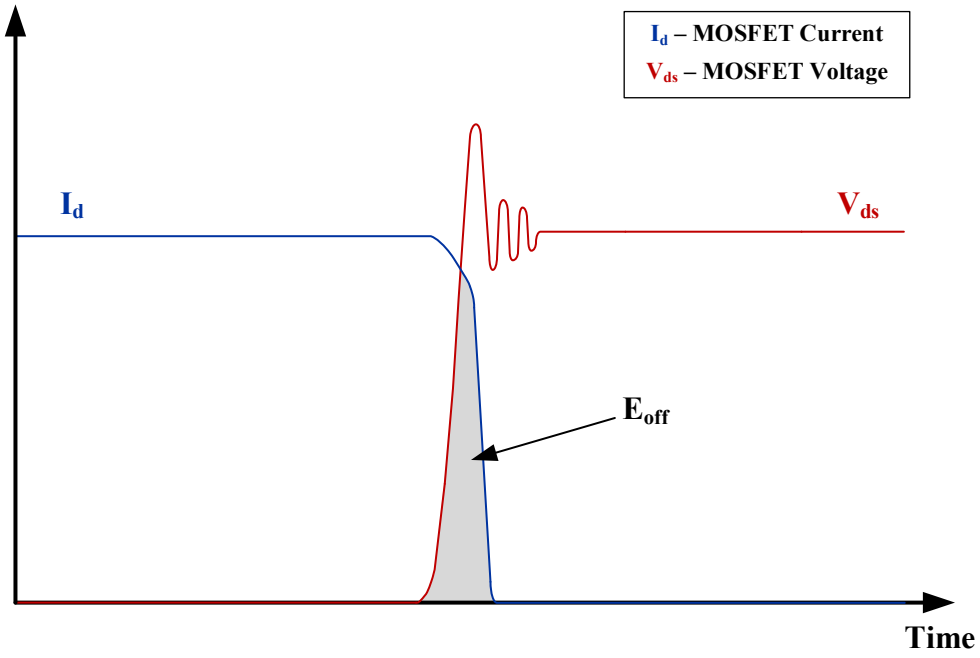

Figure 3.1: Hard switched turn-off operation of a MOSFET exhibiting voltage overshoot, high-frequency ringing, and considerable switching losses.

dependent on the converter, with some capable of achieving soft switching in a variety of ways. Using the full-bridge converter as an example, a designer can utilize coupled inductors to achieve soft switching [55]. Others in the literature have proposed auxiliary circuits for the full-bridge converter, utilizing extra passive components or switches to achieve ZVS [92, 93]. An example is shown in Figure 3.3. Since the DAB and TAB converters can achieve soft switching at no extra cost by using the leakage inductance of the transformer, the proposed converter utilizes this approach to maximize power density.

3.2 Advantages of Soft Switching

Soft switching operation in PWM converters provides numerous benefits to the performance and reliability of the system. Some of these advantages include improved efficiency over hard switching, which allows for more compact thermal management and

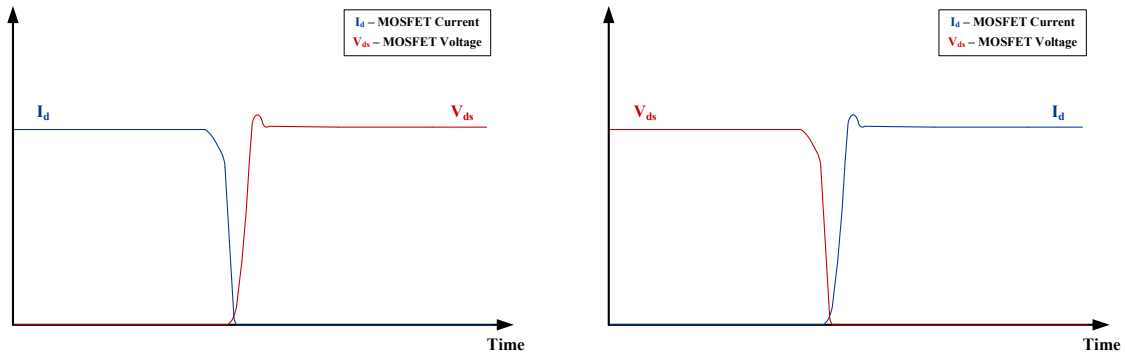

(a) (b)

Figure 3.2: Soft switched operation of a MOSFET in (a) ZCS and (b) ZVS, exhibiting reduced overshoot, losses, and oscillation.

improved power density; a reduction in EMI, which can have adverse effects on low-voltage system components, such as microcontrollers; and improved current and voltage stresses in the switching devices of the converter, which leads to improved lifetime reliability.

Oftentimes, efficiency improvements are the primary goal of soft switching operation. At the component-level, several references in the literature use double pulse testing to measure the difference in efficiency between a soft switched and hard switched SiC module. In [94], an analytical model of a SiC MOSFET is developed to predict its behavior under hard switching and soft switching conditions. The results show that soft switching reduced the losses by 97% compared to hard switching conditions. In [95], a prototype SiC MOSFET module produced by SanRex is tested in hard and soft switching operation to compare the switching losses. The authors found that the soft switching operation had 1.2 times lower switching losses at full load, and 4.5 times lower switching losses at the minimum tested load. To compare hard and soft switching in terms of converter efficiency,

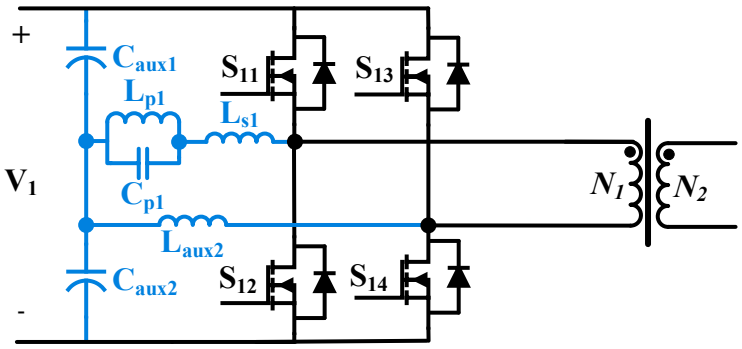

Figure 3.3: Example of auxiliary components added to achieve soft switching in a full-bridge converter [55].

[96] utilizes a boost converter that can be operated in soft switching using auxiliary switches and components. The results demonstrate the efficiency improvements of soft switching, elevating peak efficiency by roughly 8%. Similar converter efficiency results were found in [97], where the authors test a non-inverting buck-boost converter under hard and soft switching. A peak efficiency improvement of roughly 8% was found here as well under soft switching operation.

In addition to efficiency improvements, soft switching operation of a converter results in lower dv/dt and di/dt in the switching devices. Generally, higher dv/dt and di/dt will correspond to higher levels of ringing in the switching device. This high-frequency ringing, particularly between 150 kHz and 30 MHz, tends to cause conducted EMI. In radiated EMI (30 MHz to 1 GHz), components or wires in the circuit effectively become transmission antennas, radiating high-frequency electromagnetic waves to other components of the system. In conducted EMI, high-frequency signal components are transmitted through parasitic capacitance in the system. As a result, sensitive components in the system can be damaged or tripped, such as microcontrollers and low-voltage auxiliary systems. In an application such as hybrid-electric propulsion, safety and

reliability are paramount, and the EMI must be mitigated to acceptable levels to ensure passenger safety. Since there are no existing standards for hybrid-electric aircraft, the DO-160 standard is considered to be the closest EMI standard for the application [98].

In [99], two soft switching full-bridge converters are compared to a conventional, hard switched full-bridge converter. The study finds the peak conducted EMI of the soft switched converters to be several dBμV lower at frequencies below 15 MHz. In [100], buck, boost, and flyback converter topologies were considered to compare the EMI between hard and soft switched PWM converters. The resulting data shows less ringing during the switching transition, and significantly lower conducted and radiated EMI in soft switching operation. In the boost converter, soft switching operation brought the conducted EMI down to background noise levels. In the flyback converter, radiated EMI was reduced by as much as 20 dBμV. These results are consistent in the literature – in [101], di/dt and dv/dt are both reduced considerably through the implementation of ZVS in a flyback converter. ZCS has the same effect on the resultant EMI. In [102], a switched-capacitor bidirectional converter delivers consistently lower measurements of conducted and radiated EMI.

Finally, the current and voltage stresses in a converter are reduced by soft switching operation. In soft switching, the current and voltage overshoot during turn-off or turn-on are significantly reduced. In the converters presented in [100, 101], the measured voltage on the main switch has considerable overshoot when operated in hard switching mode – nearly triple the nominal switch voltage in each case. However, when operated in soft switching mode, the overshoot is either reduced or eliminated entirely. This correlates to safe operation and longer lifetimes for the switching devices of the converter. With these

factors in mind, a converter that can be operated in soft switching mode is desirable for the proposed application in a hybrid-electric propulsion system.

3.3 Soft Switching in Triple Active Bridge Converters

In order to improve efficiency, power density, and reliability, the triple active bridge converter can be operated in soft switching mode. As with the DAB, soft switching in the TAB converter is inherent to the operation of the converter and does not require auxiliary components, although the operating range is limited.

The mechanism for ZVS soft switching in the TAB converter is as follows. For a given port x, in the dead-time before the transformer winding voltage switches from negative to positive polarity, the inductor energy circulates current, discharging capacitors C_{x1} and C_{x4} and charging capacitors C_{x2} and C_{x3}. These are the parasitic capacitances of the switching devices and follow the same naming convention. After charging and discharging, current continues to flow through the diodes D_{x1} and D_{x4}, clamping the voltage across S_{x1} and S_{x4} to zero. While current is still flowing through D_{x1} and D_{x4}, S_{x1} and S_{x4} turn on, resulting in zero turn-on losses. If the current through the respective inductor is of the wrong polarity, the diode will not conduct, and soft switching will not be achieved upon turn-on. An illustration of the ZVS process is shown in Figure 3.4, using Port 3 of the triple active bridge converter as an example. Note that Figure 3.4 is adapted from data exported from PLECS simulation software, and as such the switching waveforms are ideal and do not exhibit real-world non-linear properties.

Ultimately, the condition for soft switching in a given port of the TAB is dependent on the direction of the inductor current relative to the respective port. If a port is configured on the primary side of the transformer, the inductor current must be negative at the time

that S_{x1} and S_{x4} turn on. If a port is configured on the secondary side, the respective inductor current must be positive at the time that S_{x1} and S_{x4} turn on.

In the proposed TAB converter, Ports 1 and 2 are connected to the primary windings of the transformer, while the secondary winding is connected to Port 3. Ignoring the output capacitance of the switching devices, ZVS is guaranteed to be achieved in the switching devices of Port 1 if the current through leakage inductor L_1 is negative at the switching instant t_0, when S_{11} and S_{14} are activated. Similarly, ZVS is achieved in Port 2 if the current through L_2 is negative when switches S_{21} and S_{24} are turned on at switching instant t_1. Finally, ZVS is achieved in Port 3 if the current through L_3 is positive at t_2 when switches S_{31} and S_{34} are activated. The ideal conditions for ZVS are summarized by the following [68]:

$$\begin{cases} Port\ 1: i_{L_1}(t_o) < 0 \\ Port\ 2: i_{L_2}(t_1) < 0 \\ Port\ 3: i_{L_3}(t_2) > 0 \end{cases} \tag{21}$$

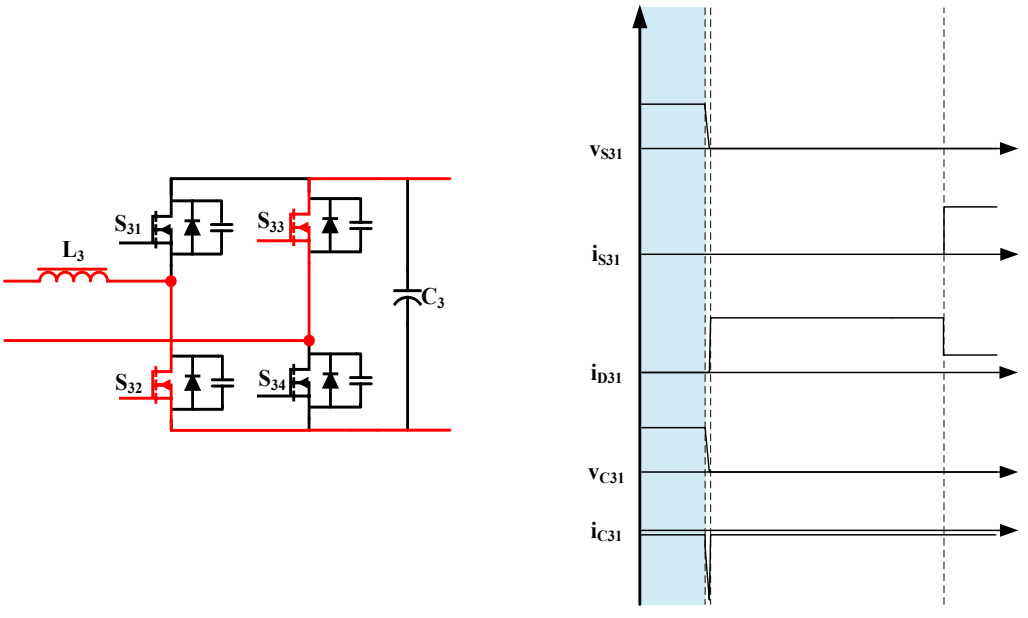

(a)

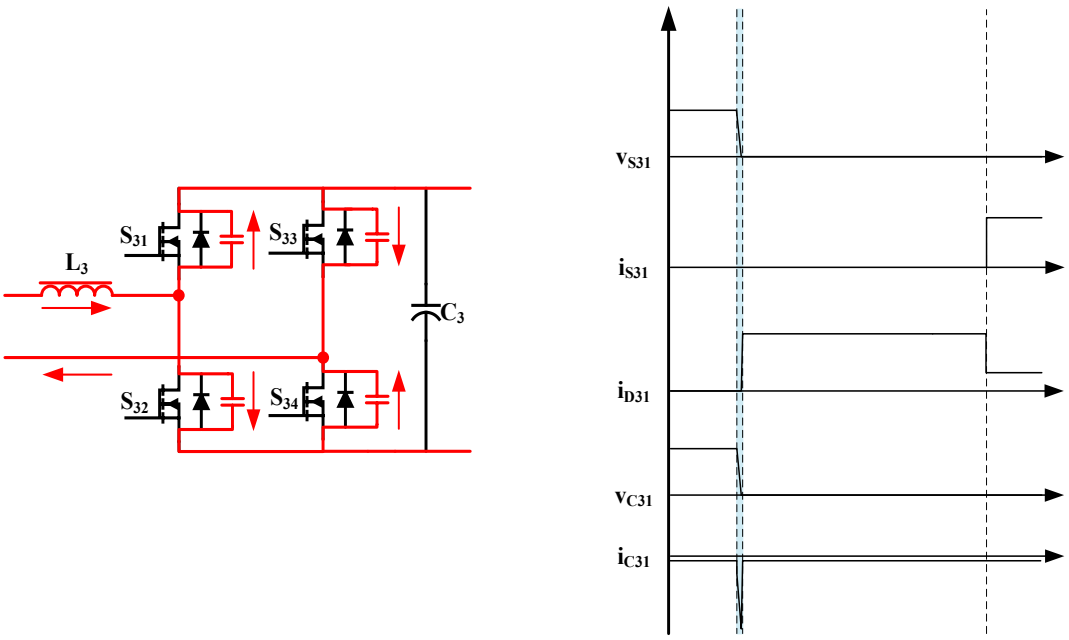
L3
S31
S33
S32
S34
C3
vS31
iS31
iD31
vC31
iC31

(b)

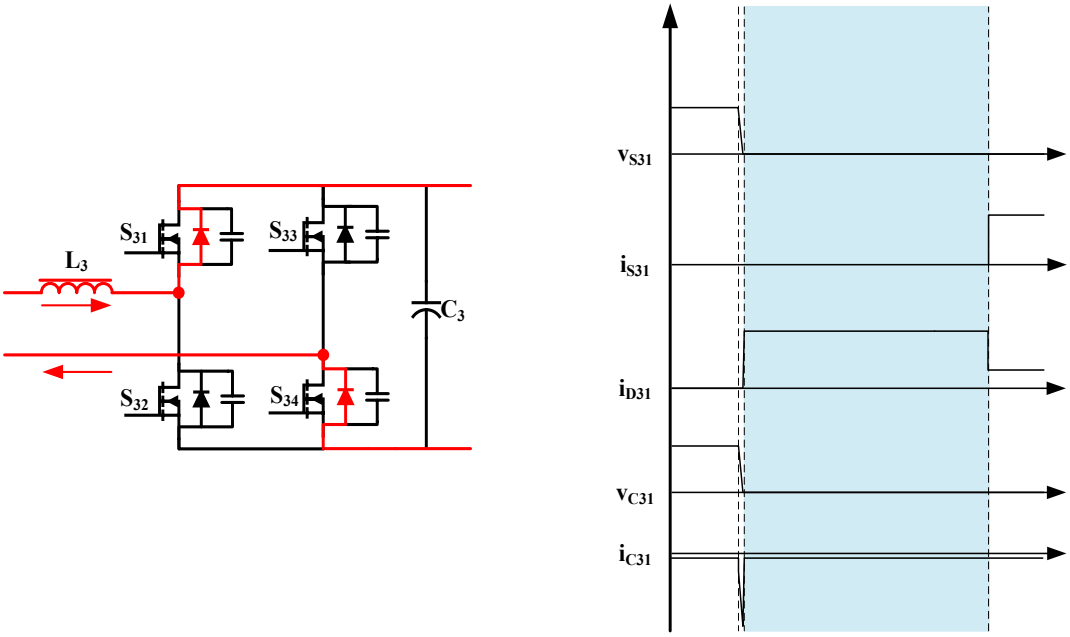
L3
S31
S33
S32
S34
C3
vS31
iS31
iD31
vC31
iC31

(c)

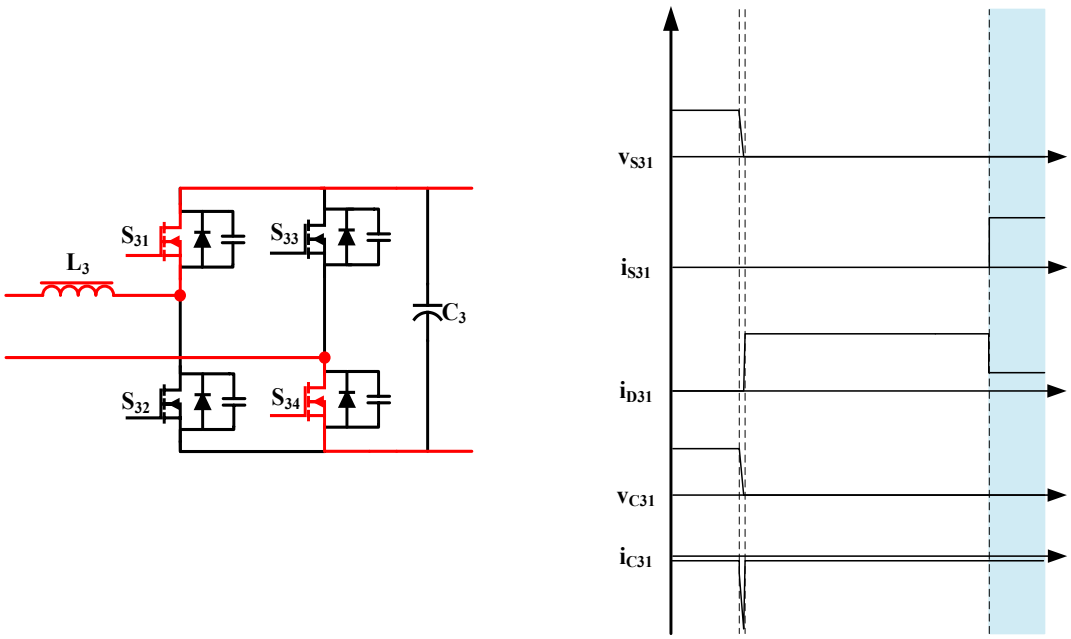

(d)

Figure 3.4: ZVS turn-on switching transition (a) before transition of S_{31}, S_{34} from off to on, (b) capacitor charging and discharging during dead-time before turn-on, (c) diode conduction during dead-time, (d) normal conduction after turn-on.

In addition to reducing the turn-on losses through ZVS soft switching, the turn-off losses of the TAB converter can be mitigated by the parallel switch capacitance. The parallel capacitor of each switch begins charging at turn-off, decreasing the dv/dt of the switch upon turn-off. This slower change in voltage across the switch results in less overlap with the decaying current waveform, and therefore lower switching losses. An illustration of this effect is shown in Figure 3.5. Like Figure 3.4, Figure 3.5 is adapted from PLECS and does not exhibit non-ideal switching behavior. A larger capacitance will lead to a lower dv/dt – in some cases, the parasitic capacitance of the switching device may be sufficient to reduce the turn-off losses to an acceptable level. In other cases, a parallel snubber capacitor can be sized according to the process in [61] to ensure that the energy stored in

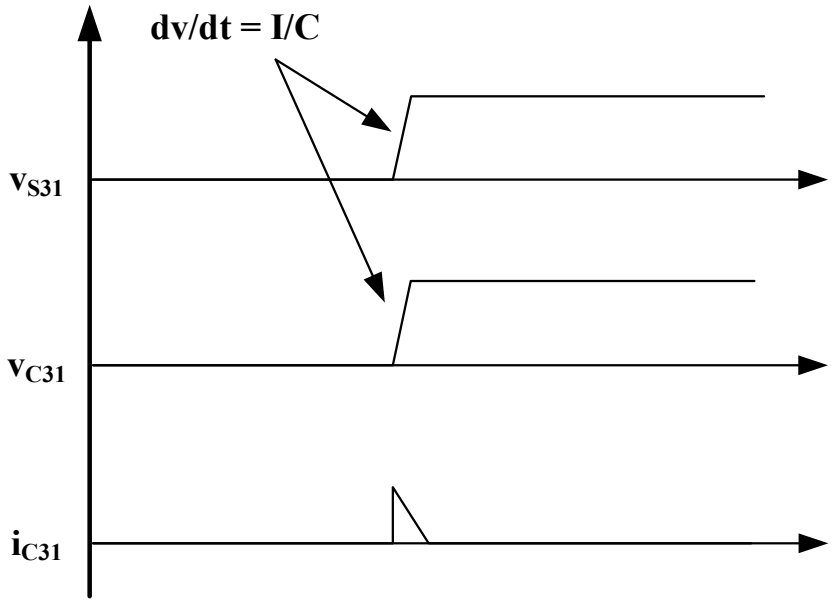

Figure 3.5: Effect of parallel device capacitance on the turn-off behavior of the MOSFET.

the inductor is sufficient to charge and discharge the snubber capacitances. In this work, only the parasitic capacitances of the switching devices are considered in the analysis.

CHAPTER 4. MODELING AND SIMULATION

In Chapter 4, the modeling of the TAB is discussed from the device level to the modeling of the full converter. The concepts of switching losses, conduction losses, and thermal impedance networks are reviewed to understand how device models are implemented in the PLECS simulation. The techniques to model the switching devices and Lithium-Ion battery are expanded upon and the design requirements of the transformer are described. The modeling of the TAB is described in detail and simulation results are given to verify the efficiency and thermal performance of the converter.

4.1 SiC Device Modeling

To quantify the power losses and efficiency of the TAB converter, the losses in the switching devices of the converter must be modeled as they are the main contributor to the overall power losses. Power losses in a switching device can generally be split into two categories: conduction losses and switching losses. Conduction losses are based on the characteristic output curve of the switching device. While the device conducts current, power is dissipated through the on-resistance and conduction power loss P_{cond} can be calculated according to [103], where E_{cond} is the conduction energy losses in J, $i_d(t)$ is device current at time t, $R_{ds(ON)}$ is the on-resistance of the device, and t_{on} is the turn-on time of the device:

$$P_{cond} = E_{cond} \cdot f_s \tag{21}$$

$$E_{cond} = \int_0^{t_{on}} R_{ds(ON)} \cdot i_d(t)^2 dt \tag{22}$$

In addition to conduction losses, switching losses also contribute to the power dissipated in a switching device. As discussed in Chapter 3, the switching losses in a device

are determined by the overlap of the voltage V_{ds} and current I_d during the turn-on and turn-off transitions in the device. Since these losses only occur at these transitions, they are also dependent on switching frequency of the converter. Switching losses in a MOSFET can be determined according to (23) – (25), where E_{on} is the turn-on switching energy loss, E_{off} is the turn-off energy loss, and P_{sw} is the total switching power loss [103]. In the integration, $t_{d(on)}$ is the turn-on delay time of the MOSFET, t_r is the rise time, and t_f is the fall time.

$$E_{on} = \int_0^{t_{d(on)}+t_r} v_{ds}(t) \cdot i_d(t) dt \tag{23}$$

$$E_{off} = \int_0^{t_{d(off)}+t_f} v_{ds}(t) \cdot i_d(t) dt \tag{24}$$

$$P_{sw} = \left(E_{on} + E_{off}\right) \cdot f_s \tag{25}$$

In addition to power losses in the converter, information on the thermal performance of the converter is critical. High temperatures in a power converter correspond to heavier thermal management, requiring larger heatsinks or active cooling solutions. Weight must be minimized in a hybrid-electric aircraft system, so the temperature of the converter must be manageable without bulky thermal management solutions.

To estimate the temperatures in the converter, a thermal model must be built to represent the thermal impedance of the switching devices. The thermal impedance of a device represents its thermal behavior when presented with transient pulses of power. Based on a measured thermal impedance curve, an equivalent model can be built that reflects the characteristics of the device. From the equivalent model, the junction temperature rise can be calculated to characterize the junction temperature of a device.

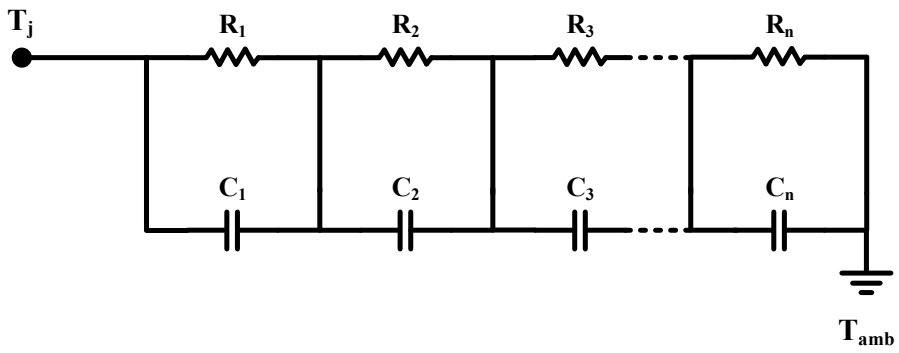

Figure 4.1: An n^{th} order Foster thermal model.

The thermal impedance network of a device can be modeled in PLECS as either a Cauer or Foster RC thermal model. The Foster model is derived by fitting a curve to the thermal impedance, resulting in the RC model shown in Figure 4.1. The Foster model has no physical basis but can be tuned to fit the thermal impedance curve of the device and is trivial to analyze.

Meanwhile, the Cauer model is based on the physical heat-transfer characteristics of the device and can be used to model the individual layers in a switching device and their thermal properties, e.g., the silicon junction, back of the silicon chip, package leads, etc. A Cauer thermal model with *n* elements is illustrated in Figure 4.2.

In PLECS, a thermal description can be added for power devices such as MOSFETs and diodes. For each device in the simulation, there is a description for turn-on and turn-off losses, conduction losses, and thermal impedance. Table 4.1 summarizes the commercial switching devices used in the simulation. Each device was modeled in the simulation using a manufacturer-specified thermal description, available from Wolfspeed.

PLECS takes a different approach to component modeling and loss calculation than simulation software packages such as Simulink or LTspice. To reduce simulation time, a

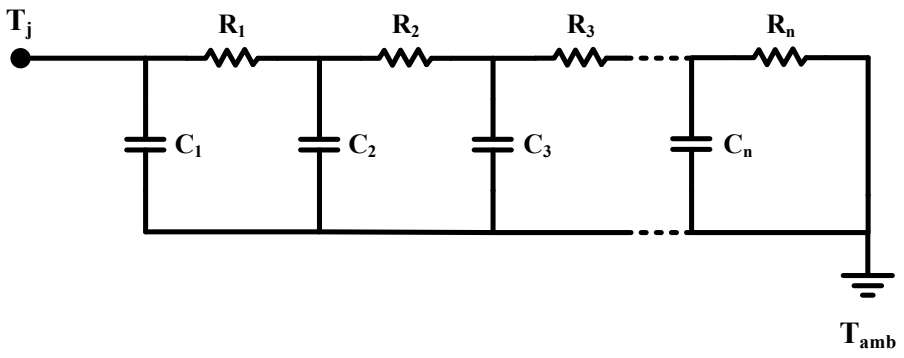

Figure 4.2: An n^{th} order Cauer thermal model.

lookup table is used to calculate the switching losses rather than computing the small time-steps required for waveform analysis. Additionally, switching devices in PLECS are electrically modeled as ideal switches and device parasitics are not considered. The resulting switching voltages are ideal square-wave pulses. From the lookup tables, power losses can be calculated using on-state current, pre- and post-switching current and voltage, and junction temperature. If the input parameters are between two points on the lookup table or outside the data offered by the lookup table, linear interpolation is used to obtain the resulting energy losses. Figure 4.3 gives a plotted example of a lookup table used to calculate the turn-off losses in a MOSFET. For several junction temperatures, each combination of the blocking voltage v_{block} and the on-state current i_{on} yields switching

Table 4.1: Commercial SiC switching modules used in the simulation model.

Port	Voltage Rating	Current Rating	Manufacturer	Part Number
Port 1	1.2 kV	425 A	Cree/Wolfspeed	CAB425M12XM3
Port 2	1.2 kV	765 A	Cree/Wolfspeed	CAB760M12HM3
Port 3	1.7 kV	225 A	Cree/Wolfspeed	CAS300M17BM2

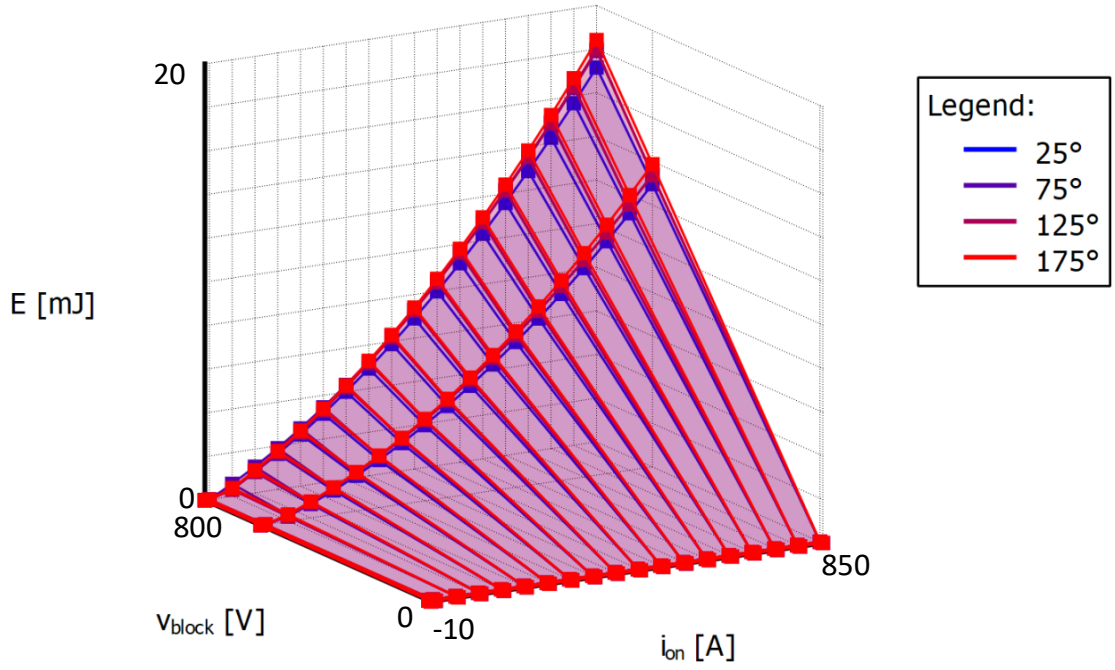

Figure 4.3: A 3D turn-off energy chart used to calculate the turn-off energy losses in a MOSFET in PLECS simulation software.

energy losses E_{off} and E_{on} in mJ. This is processed by an impulse averaging block in PLECS to calculate P_{sw} in Watts. The switching losses presented in this chapter are obtained by averaging over 10 switching cycles.

Conduction losses of the switching devices in PLECS software are calculated according to device current and the on-state voltage by using the forward voltage and on-resistance of the device. Figure 4.4 gives an example of a conduction loss curve for a MOSFET in PLECS.

In addition to the power losses of the device, PLECS allows for thermal modeling to monitor the junction temperature of switching devices in the simulation. Each switching module is represented using the Cauer thermal model. From the device, the thermal energy is transferred to the network shown in Figure 4.5, consisting of a heatsink component, a

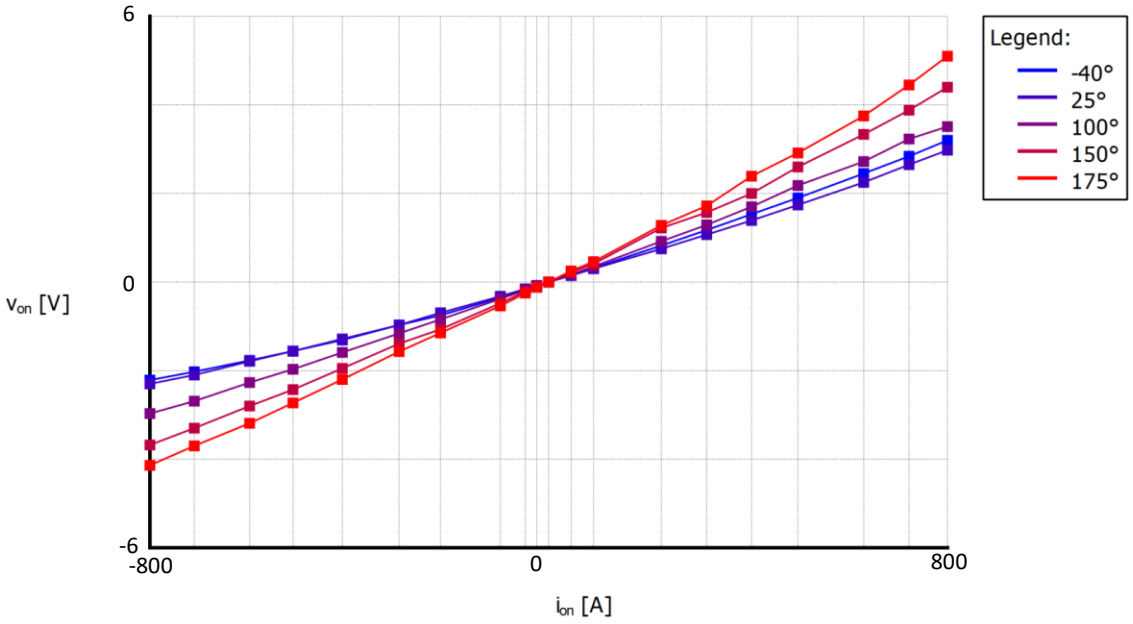

Figure 4.4: Conduction loss curve definition for a semiconductor switch module in PLECS.

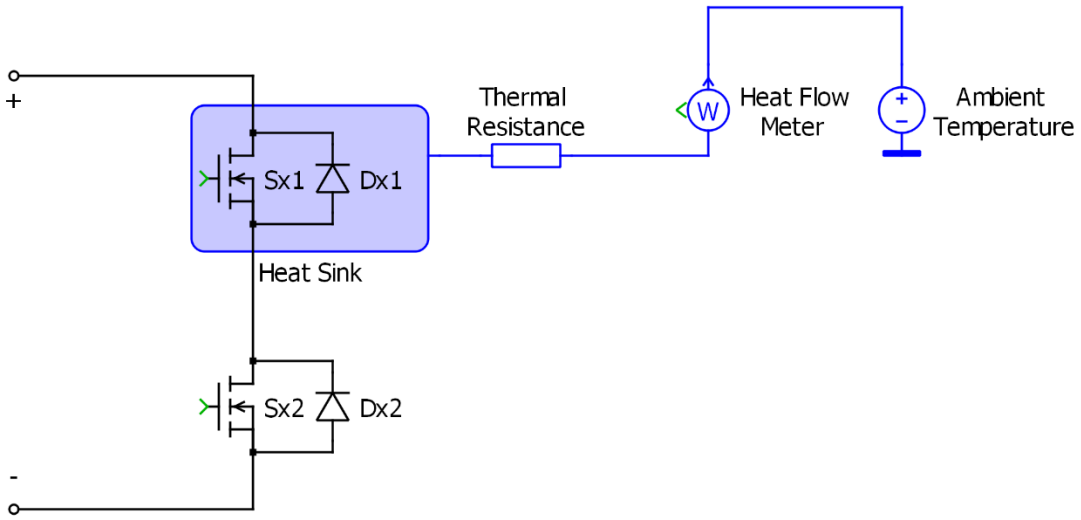

Figure 4.5: Thermal network used to connect a switching device to ambient temperature in PLECS.

thermal resistor, a heat flow meter for measurement, and thermal ground (ambient temperature). The heatsink component in PLECS absorbs the thermal losses dissipated by the enclosed components. At the same time, the boundaries of the heatsink create an isolated thermal environment that propagates its temperature to the components within. This allows PLECS to update the component losses based on the temperature observed by the heatsink. Only one MOSFET is monitored in each H-bridge port due to the symmetry of the circuit. The specifications of the thermal network are as follows:

- Heatsink-to-ambient thermal capacitance $C_{th_{sa}} = 1\ mJ/K$
- Heatsink-to-ambient thermal resistance $R_{th_{sa}} = 1\ mK/W$
- Initial temperature $T_0 = 50$ ℃
- Ambient temperature $T_{amb} = 50$ ℃

4.2 Lithium-Ion Battery Modeling

The battery model in the simulated TAB converter is used to accurately model the dynamic behavior and electrical characteristics of a Lithium-Ion battery pack during charging and discharging and allow for the verification of regenerative charging in the converter. The battery model utilized is based on a battery component found in the PLECS Demo Model "Power Split Hybrid Vehicle System". The battery component in the model is based on the resistor-only dynamic battery model proposed in [104] for the purpose of EV state of charge (SOC) modeling.

The battery model makes several assumptions. First, it is assumed that the internal resistance is constant during the charge and discharge cycles and does not vary as a function of current. Second, the parameters are derived from the discharge characteristics of the

battery and assumed to be the same for charging. Third, the Peukert effect is not taken into account, and the battery capacity does not change with the amplitude of the current. Finally, temperature does not affect the behavior of the battery model.

The parameters used in the model are based on typical Lithium-Ion batteries and are given in Table 4.2.

4.3 Transformer Loss Modeling

While transformer losses are not modeled in the PLECS simulation, this section is used to discuss the design of the high-frequency transformer and the process to calculate the associated core and winding losses. Core and winding losses (P_{fe} and P_{cu}, respectively) in a transformer can be calculated according to the following equations [105, 106]:

$$P_{fe} = (PL)A_c l_m \tag{26}$$

$$P_{cu} = \frac{\rho(MLT){N_1}^2 {I_{total}}^2}{W_A K_u} \tag{27}$$

Equation 26 is used to calculate the core loss, where PL is the core loss density, A_c is cross-sectional area of the core, and l_m is the mean magnetic path length of the core. Meanwhile,

Table 4.2: Parameters of Lithium-Ion battery model.

Battery Parameters	**Value**
Cell internal resistance	1 mΩ
Rated cell capacity	2.4 Ah
Nominal cell capacity	2.1 Ah
Nominal cell voltage	2.9 V
Nominal discharge current	2.3 A

Equation 27 is used to calculate copper winding losses, where ρ is the effective resistivity of the wire, MLT is the mean length per turn in cm, I_{total} is the total RMS winding current, W_A is the window area of the transformer, and K_u is the winding fill factor.

Since many of these parameters rely on the physical description of the transformer, a full transformer design must be developed and prototyped to determine the core and winding losses. While no such model is developed in this work, the required area product of a transformer assuming a toroid core is calculated as follows.

The area product of the transformer WaAc is the product of the window area (W_A) and core area (A_c) and is evaluated according to Equation 28, where P_o is output power, D_{cma} is current density (circular mils/A), and K_t is the topology constant. The maximum flux density B_{max} of typical nanocrystalline materials is roughly 1.2 T, or 12,000 Gauss [107, 108]. According to [109], topology constant K_t is 0.0014 for full-bridge topologies, and current density D_{cma} can be assumed to be 750 circular mils/A for a conservative design.

$$WaAc = \frac{P_o D_{cma}}{K_t B_{max} f} = \frac{300\ kW \cdot 750\ cir.\ mil/A}{0.0014 \cdot 12000\ G \cdot 20\ kHz} = 669.64\ cm^4 \tag{28}$$

The resulting requirement for the area product of the transformer is 669.64 cm^4, which can be used to specify a nanocrystalline core for future prototypes and development.

4.4 Modeling Output Capacitance

As discussed in Section 3.3, the output capacitance of the switching devices must be modeled to accurately represent the switching losses in the converter. In addition to misrepresented switching losses, omitting the parallel capacitance in the model can lead to different ZVS conditions for the converter. According to [61], the conditions for ZVS with

a parallel capacitance are no longer solely dependent on the polarity of the current, especially for larger capacitance values. The author states with a parallel capacitance on each device, the energy stored in the inductor at the time of switching must completely charge and discharge the capacitors in the respective port.

In PLECS simulation software, power semiconductors are modeled as ideal switches. As such, a model integrating the effects of capacitance and other parasitic parameters in the SiC MOSFET is not available. Figure 4.6 shows the parasitic capacitances of a MOSFET device, where C_{rss} is the reverse transfer capacitance of the device, C_{oss} is the output capacitance, C_{iss} is the input capacitance, C_{gs} is the gate-to-source capacitance, C_{gd} is the gate-to-drain capacitance, and C_{ds} is the drain-to-source capacitance. To model the device capacitance in PLECS, a static capacitance is placed in parallel with the switching device, with its capacitance estimated based on the capacitance curves of the corresponding device datasheet and the expected blocking voltage during normal operation. While the capacitance values would vary with blocking voltage in a physical device, this method allows for an estimation of the effect of the device capacitance on the turn-off losses of the converter. The value of the parallel capacitance in the model is calculated according to (29). Since C_{rss} is orders of magnitude lower than C_{oss}, the value of C_{ds} is practically equal to the output capacitance C_{oss}.

$$C_{ds} = C_{oss} - C_{rss} \tag{29}$$

The problem with this implementation can be seen when soft switching operation is lost in the converter. If the capacitor is not fully discharged before the transition from OFF to ON, the remaining charge is shorted through the switching device and a large current spike is observed. As a result of the inrush of current, the extrapolation used by the switching loss

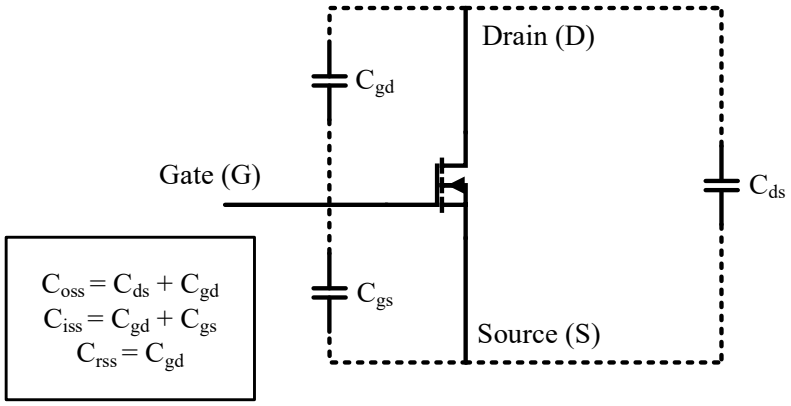

Figure 4.6: Parasitic capacitance C_{oss} of a MOSFET device.

lookup tables produces unrealistically high losses during turn-on. This behavior is not accurate to real-world operating conditions. In a real MOSFET, the energy losses due to the output capacitance are a fixed value in hard switched operation, and only become a significant contributor at very light loads [110, 111]. To circumvent this modeling error, Port 3 data under 50% load in Section 4.5.2, where ZVS is lost, is substituted with data from the ideal model. This presents a more accurate estimate of the turn-on losses and avoids the computational errors present in the model with a parallel capacitor.

4.5 Simulation Results

In this section, the results of the PLECS model are presented and analyzed – first with MOSFET parasitic capacitance omitted from the simulation, then modeled as a static capacitor in parallel with each switch. Three primary operating modes are simulated as defined in Section 2.2. The simulations are performed at an ambient temperature of 50 °C to emulate worst-case thermal conditions. Note that the efficiency results presented in the following sections are only representative of the semiconductor device losses of the TAB, and do not include the transformer losses, filter losses, or losses of other power electronics

in the full series-hybrid system. Consequently, the efficiency presented is not representative of a full system analysis. Considering the other power electronics in the hybrid-electric drivetrain, full system efficiency is estimated in Section 4.5.3.

The converter is simulated on a 4.8 Ω resistive load to ensure an output voltage of 1.2 kV at full power. In Mode 3, the converter is configured to use a 300 V DC source to represent a voltage induced on Port 3 by the regenerative methods discussed earlier. The bidirectional nature of the converter is utilized to direct power from Port 3 to Port 2 and charge the battery of the aircraft. The operating parameters of the TAB are given in Table 4.3.

While each operating mode in the converter is representative of a typical load percentage (e.g., the converter is operated in Mode 2 during cruising, which typically requires 33% of the full-load power), it is useful to plot the load curves for each mode to observe performance at lower load conditions. For the following load curves, 100% load refers to the full load at the specified operating mode. That is, 300 kW at Mode 1 and 100 kW at Mode 2. Mode 3 is designed to transfer any available power to the batteries. Therefore, the load percentage refers to the percentage of the supply voltage on Port 3 out of 300 V.

Table 4.3: Operating parameters of the proposed TAB converter.

Parameter	**Value**	**Parameter**	**Value**
Generator rated power	100 kW	Generator DC-link voltage	540 V
Battery rated power	200 kW	Battery voltage	800 V
Motor rated power	300 kW	Inverter DC-link voltage	1200 V
Inductances L_1, L_2, L_3	13 µH, 13.5 µH, 0.1 µH	Switching frequency	20 kHz
Capacitors C_1, C_2, C_3	600 µF, 600 µF, 500 µF	Transformer turns ratio	1:1:1.8

4.5.1 Ideal Model

In the ideal model, parasitic capacitance of the MOSFET is not modeled and therefore there is no effect of the parasitic capacitance on the model. As discussed in Section 3.3, this results in an overestimation of the turn-off losses since the rise in voltage on the switch is instantaneous. Figure 4.7 shows the ideal PLECS model used to simulate Modes 1 (takeoff) and 2 (cruising and descent).

In Mode 1, the simulation is set to emulate the power draw during aircraft takeoff, which uses the full rated capability of the propulsion system. At 100% load, Port 1 supplies 100 kW of power. Port 2 supplements the generator power by supplying 200 kW from the batteries, and the total output power to Port 3 is 300 kW. This is the highest rated power of the converter. Figure 4.8 illustrates the phase shift enacted between the transformer windings to achieve the rated power. Meanwhile, Figure 4.9 shows the efficiency curves for each H-bridge port in Mode 1 operation. The ratio of power delivered by Ports 1 and 2

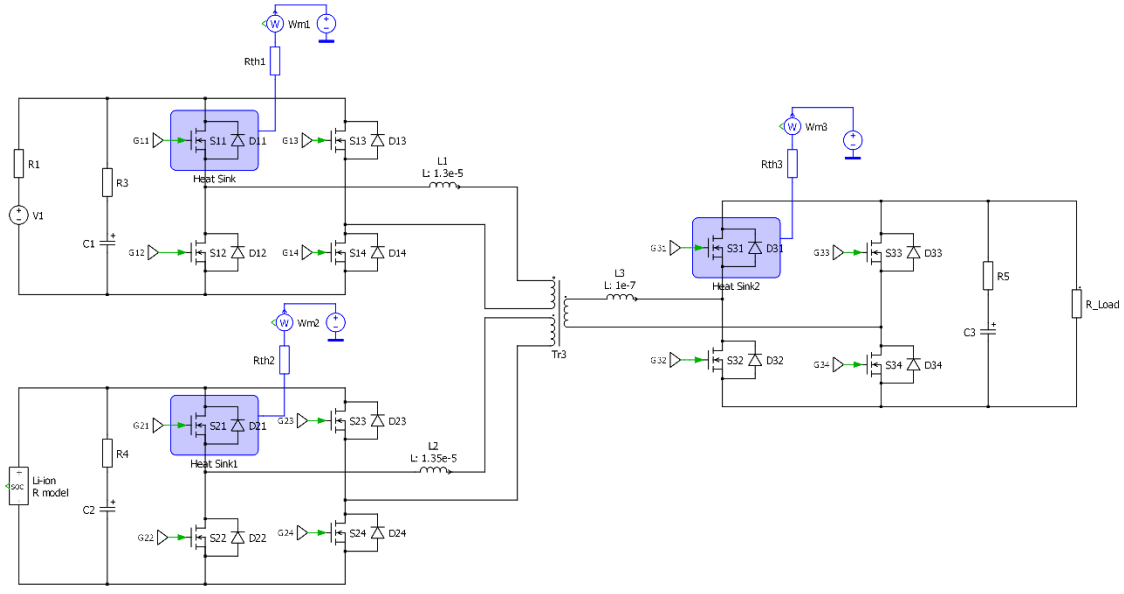

Figure 4.7: Ideal PLECS model used to simulate the propulsion modes of the TAB converter.

remains the same throughout the efficiency curve. That is, Port 1 delivers 1/3 of the output power and Port 2 delivers 2/3 of the output power for each load percentage. Under 50% load, ZVS operation is lost in Port 3 and the efficiency decreases.

In Mode 2, the switching devices in Port 2 are turned off and the TAB operates as a DAB, transferring power only from Port 1 to Port 3. This simulates the cruising and descent modes of the hybrid-electric aircraft, which typically requires a maximum of 30% of the rated power and uses only the onboard generator to provide power. In this mode of operation, 100% load refers to the 100 kW rated power of the generator being transferred to the propulsion motor load. In Figure 4.10, the transformer voltages and currents can be seen for 100% load during Mode 2. Figure 4.11 illustrates the converter efficiency during cruising operation.

In Mode 3, the converter operates in regenerative charging mode. Unlike electric ground-vehicles, regenerative charging of aircraft systems is used infrequently and only in special cases, such as braking during runway taxiing. To demonstrate the regenerative capability of the converter, a 300 V source is applied at the DC-link of Port 3 for 100% load. The PLECS schematic used to simulate Mode 3 is almost identical to that shown in Fig. 4.7, with the load resistor in Port 3 replaced with a DC voltage source to represent the voltage available at the port for regenerative charging. For each load percentage, the available voltage at Port 3 is adjusted accordingly.

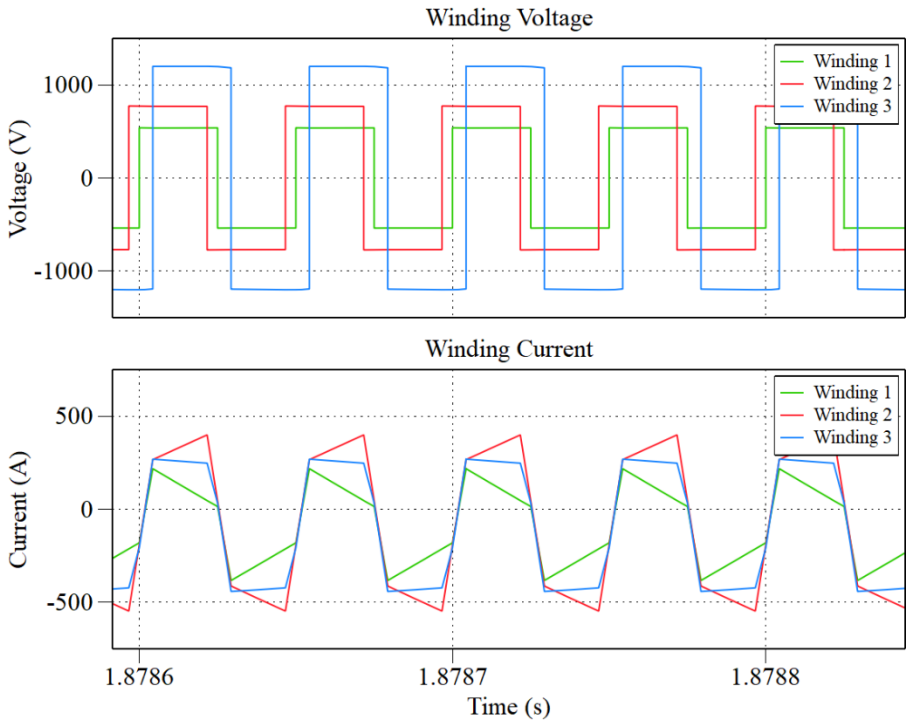

Figure 4.8: Transformer winding voltages and currents at 100% load during Mode 1 (takeoff).

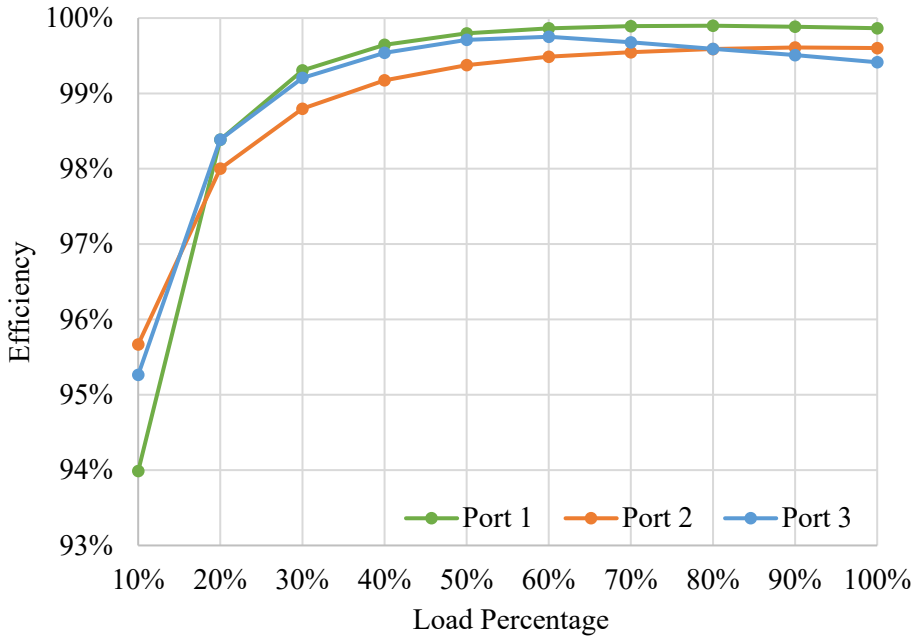

Figure 4.9: Port efficiency curves for the ideal model operating in Mode 1.

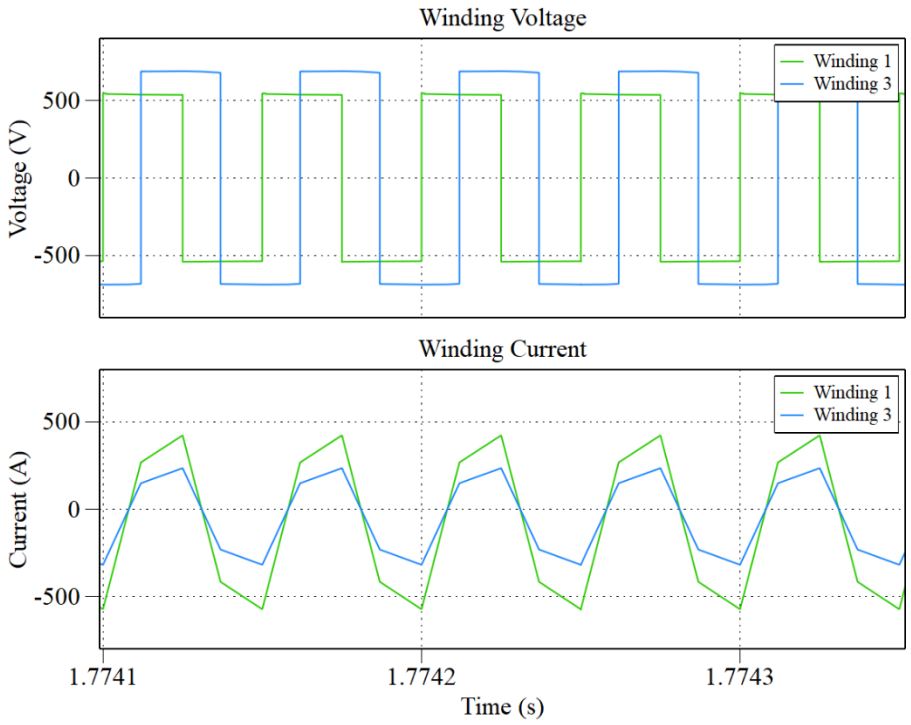

Figure 4.10: Transformer winding voltages and currents at 100% load, Mode 2.

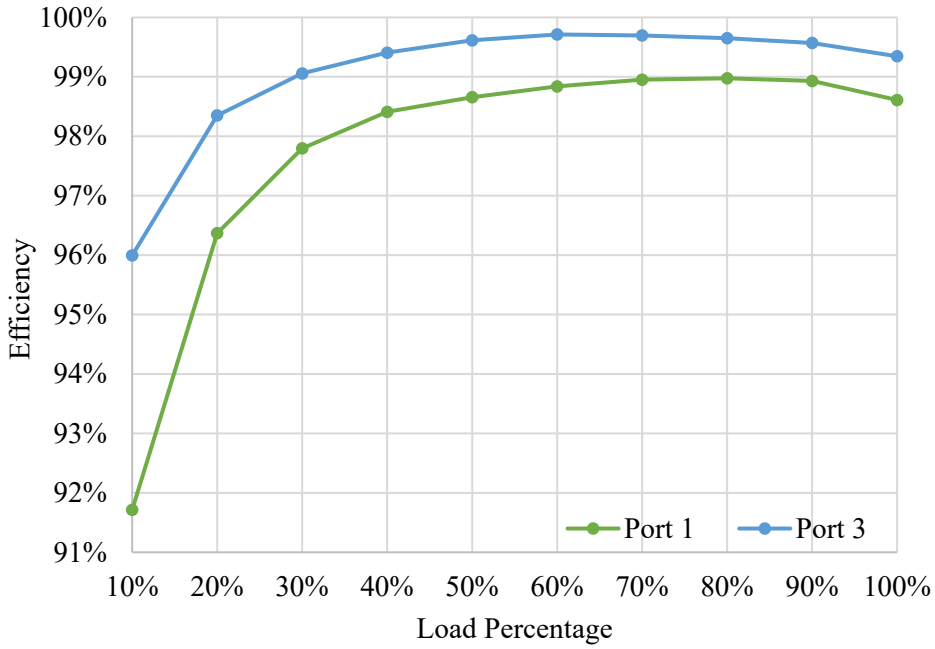

Figure 4.11: Port efficiency curves for the ideal model operating in Mode 2.

Figure 4.12 shows the winding voltage and current on the transformer during Mode 3. Note that in Mode 3 a 90-degree phase shift is present between Ports 1 and 3 to maximize power transfer. Figure 4.13 illustrates the efficiency curve for the regenerative charging mode, based on the available voltage on the DC-bus.

In addition to individual port efficiency, the overall efficiency curves for the TAB converter in each mode can be seen in Figure 4.14. In the ideal model, the peak efficiency of the converter is 99.36%, reached at 60% of full load during Mode 1. The lowest efficiency observed is 45.98% efficiency for very low-power charging operation (Mode 3). The lowest efficiency during propulsion operation (Modes 1 and 2) is 88.39% at 10% load in Mode 2. In each mode, the conduction and switching losses increase at lower load percentages. This is because the transformer currents increase as the voltage ratio strays further from unity, placing higher switching stress and conduction current through the MOSFETs. In Modes 1 and 2, the converter exits the ZVS range below 50% load and switching losses increase. In Mode 3, the converter loses soft switching below 40% of full load.

A more realistic approach to observing the propulsion efficiency – i.e., the efficiency during propulsion Modes 1 and 2 – of the converter is shown in Fig. 4.15. In Fig. 4.15, the converter is employed as it would be in a typical flight profile – from 0 kW to 100 kW, the converter operates in Mode 2, with only the generator supplying power to the load. From 100 kW to 300 kW, the battery supplements the power from the generator and the converter operates in Mode 1. The dip in efficiency observed between Mode 2 and Mode 1 follows the efficiency curves of Mode 2. At 100% load, the current through the

active switching devices nears the rated maximum, causing the overall efficiency of the converter to decrease.

In Fig. 4.16, the breakdown of switching and conduction losses in the converter is presented for each operating mode at full load. In the ideal model, the switching loss is more dominant than the conduction losses in Mode 1, and still quite prevalent in Modes 2 and 3. Since the converter operates in ZVS soft switching at 100% load, these switching loss are all attributable to turn-off losses in the system and can be eliminated by the inclusion of a parallel capacitor in the model.

Finally, Fig. 4.17 demonstrates acceptable thermal performance of the converter at the expected load conditions, even at worst-case ambient temperature conditions. The highest observed temperature takes place in Mode 2, stabilizing at 88 °C in Port 1 – a 38 °C temperature rise from the 50 °C ambient temperature of the simulation. It should be noted that the ideal model presents an overestimation of the turn-off switching losses.

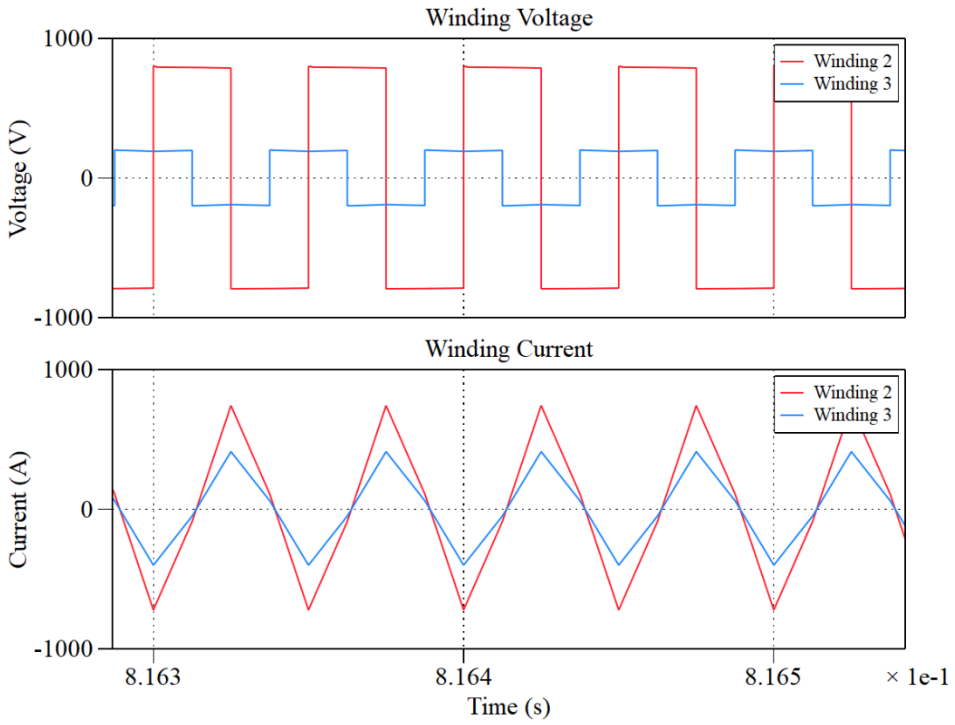

Figure 4.12: Transformer winding voltages and currents at 100% load, Mode 3.

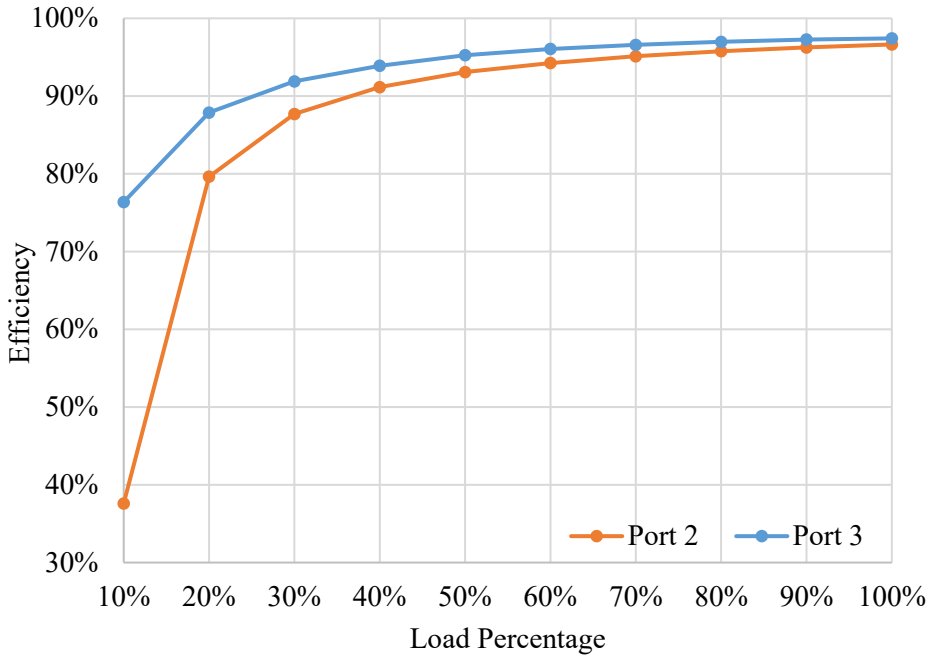

Figure 4.13: Port efficiency curves for the ideal model operating in Mode 3.

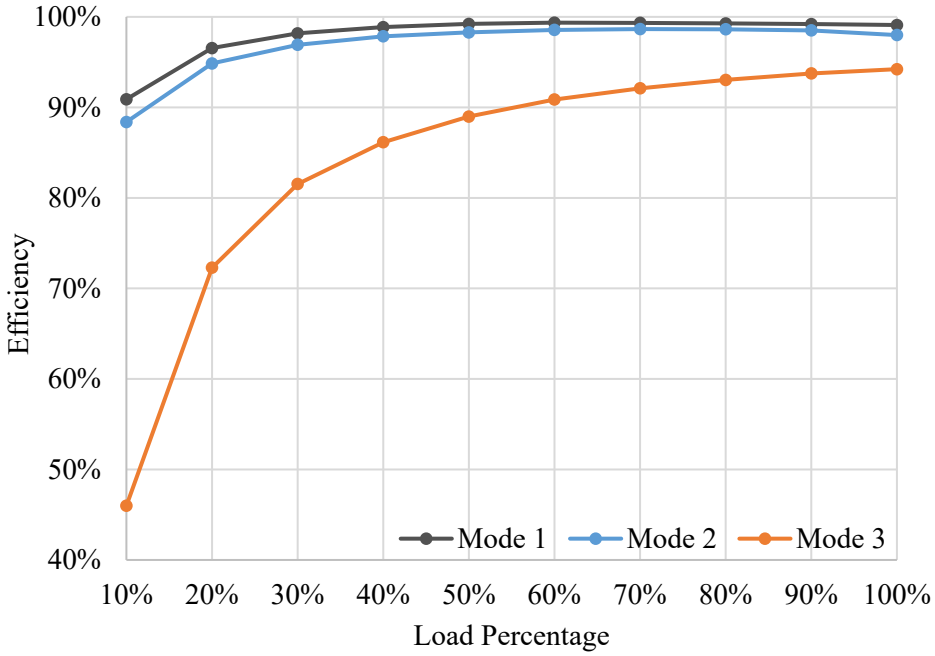

Figure 4.14: Overall efficiency of the ideal TAB converter in each operating mode.

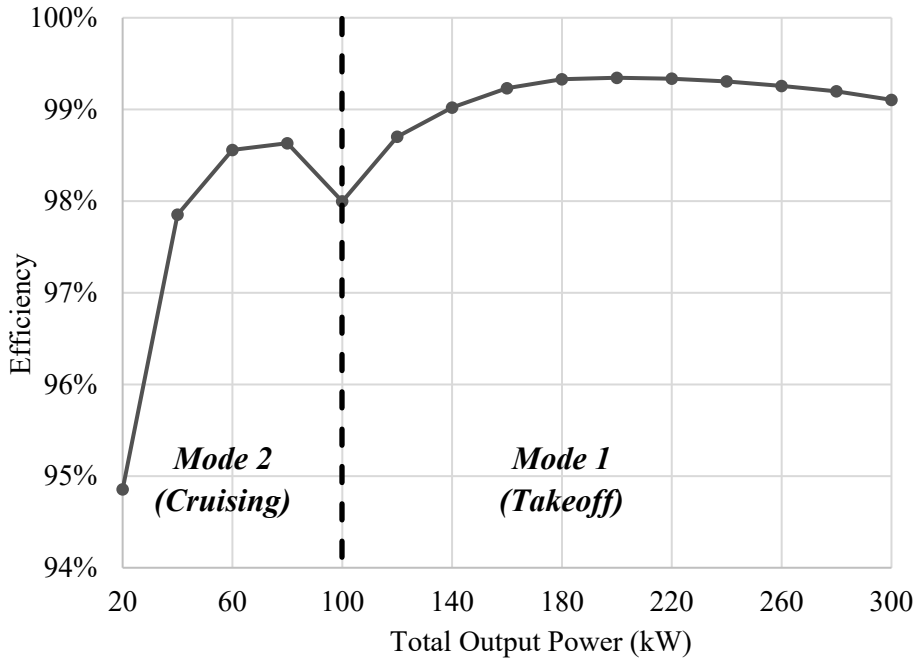

Figure 4.15: Propulsion efficiency of the ideal TAB converter from 20 kW to 300 kW.

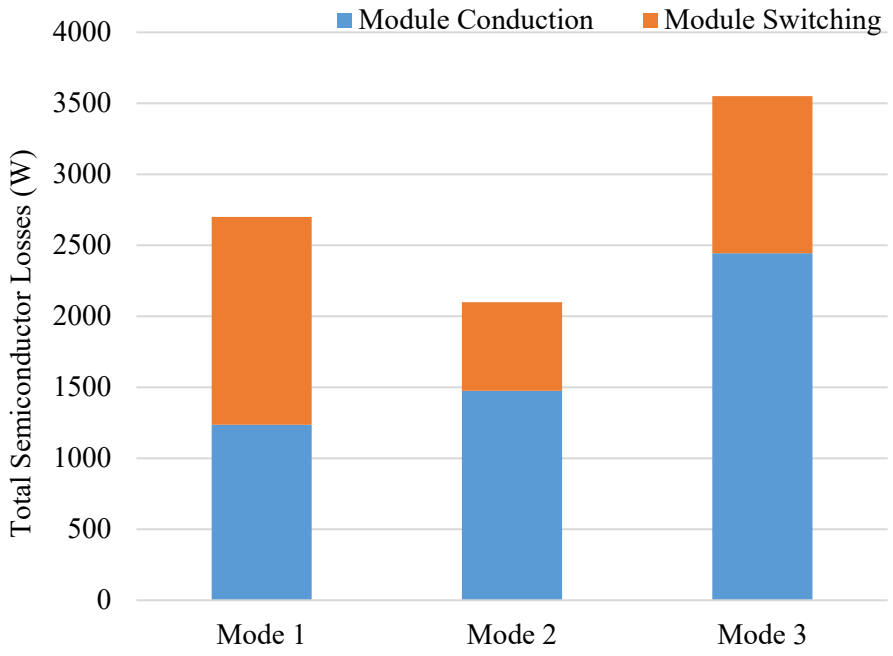

Figure 4.16: Breakdown of semiconductor module losses in the ideal model.

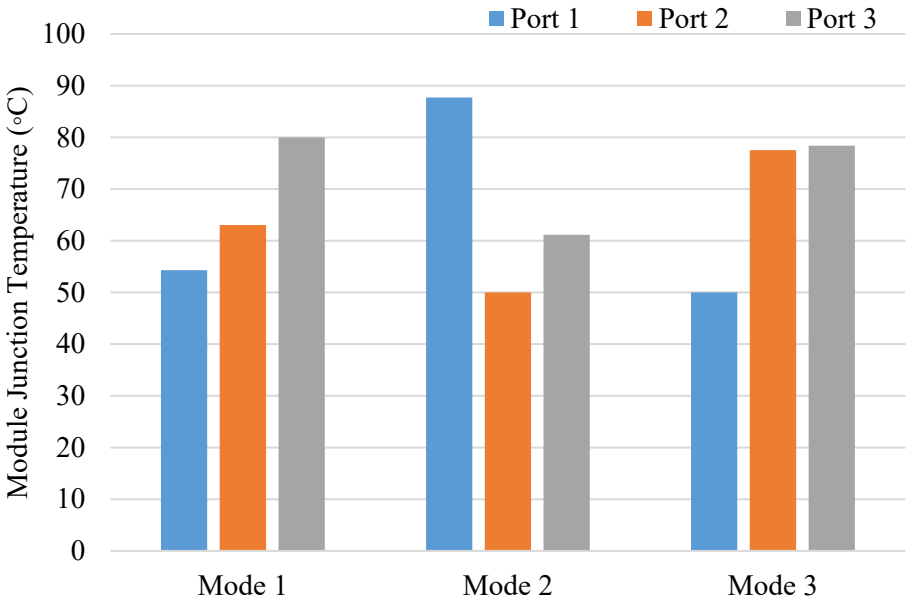

Figure 4.17: Module junction temperatures for each mode in the ideal model.

4.5.2 Non-Ideal Model

The non-ideal model, shown in Fig. 4.18, attempts to model the parasitic output capacitance of the switching devices in the converter. The expected results with the inclusion of the capacitance are lower turn-off losses and overall higher efficiency. However, as discussed previously, the turn-on losses in the non-ideal model become unrealistically high when ZVS is lost since the output capacitance is modeled as a static parallel capacitor. To ensure more accurate results for the load curves, losses from the ideal model are substituted for the corresponding data points where ZVS is lost. For example, if ZVS is lost in Port 3 during Mode 1 at 40% load, the Port 3 losses from the ideal model at the same conditions will be used instead of the value from the non-ideal model. Since the ideal and non-ideal model have the same ZVS boundary, this gives the most accurate view of the non-ideal load curve given the constraints of the model.

The PLECS model utilized in this section is given in Fig. 4.18, using the same method as the ideal model to simulate regenerative charging in Mode 3. The parallel capacitance of each MOSFET is estimated via the C_{oss} and C_{rss} curves in the respective datasheet. The static value of capacitance for each MOSFET is given in Table 4.4.

Table 4.4: MOSFET parasitic capacitance present in the non-ideal PLECS model.

Port	**MOSFET Part No.**	**Parasitic Capacitance**
Port 1	CAB425M12XM3	1.135 nF
Port 2	CAB760M12HM3	2.81 nF
Port 3	CAS300M17BM2	2.42 nF

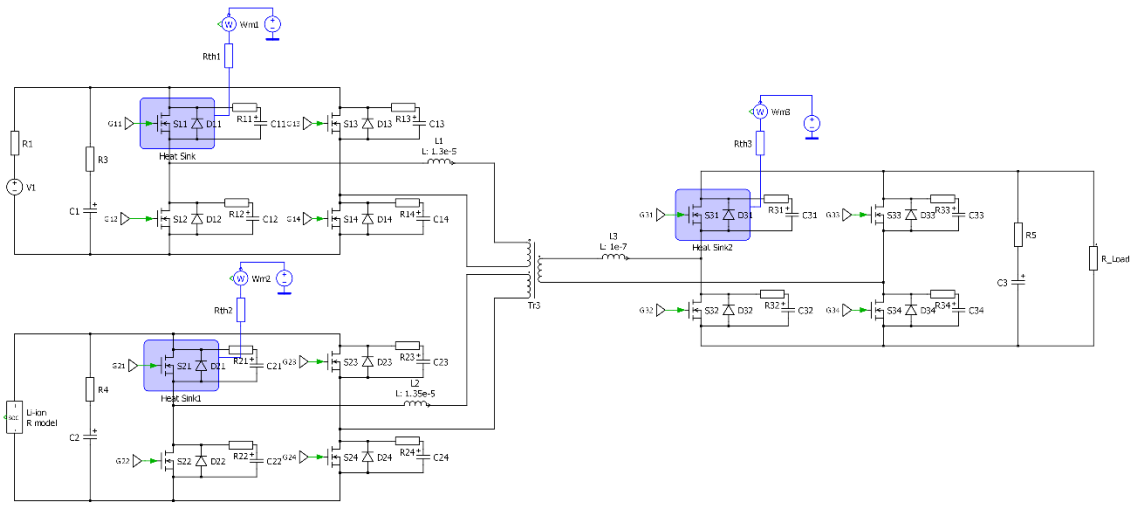

Figure 4.18: Non-ideal PLECS model used to simulate the propulsion modes of the TAB converter.

The methods used to simulate the operating modes of the converter remain the same for the non-ideal model. The port efficiency curves for Modes 1, 2 and 3 are shown in Figures 4.19, 4.20 and 4.21, respectively. Note that each port exhibits higher efficiency in the non-ideal model and for a wider range of load percentages. The drop in efficiency under 50% load appears greater for the non-ideal model since, unlike the ideal model, the turn-off losses are eliminated and do not scale with conduction losses during ZVS operation.

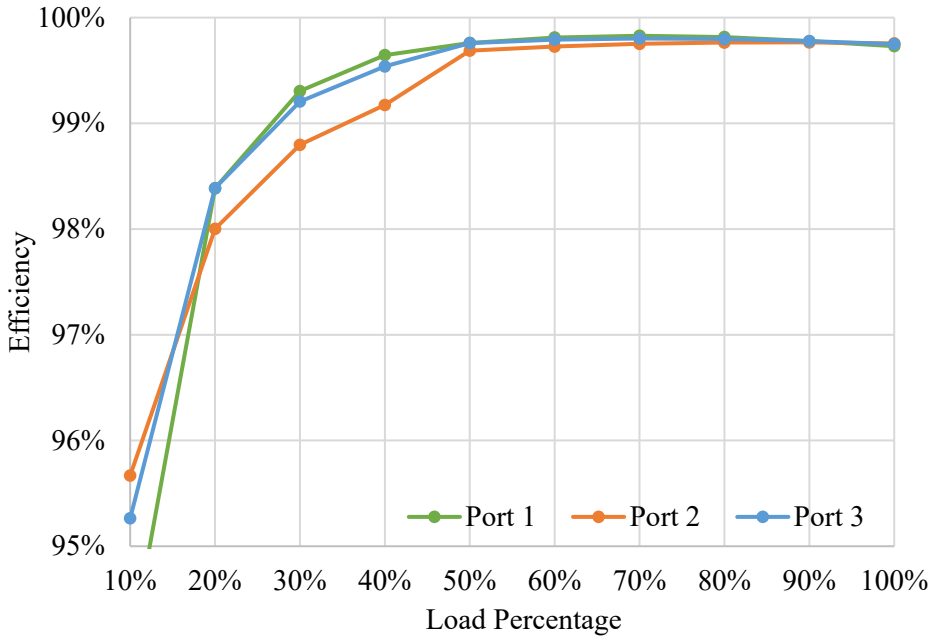

Figure 4.19: Various TAB port efficiency curves for the non-ideal model, Mode 1.

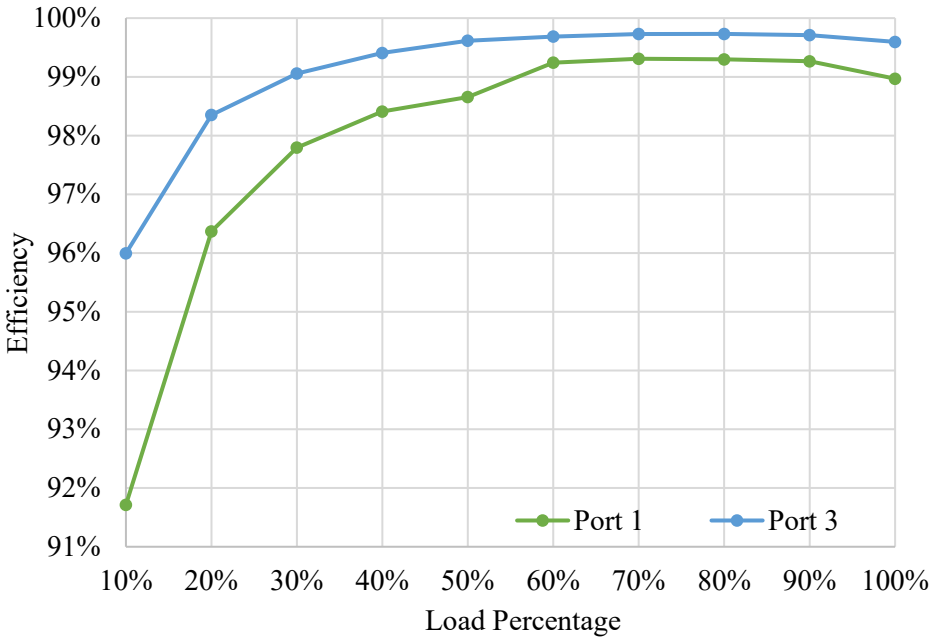

Figure 4.20: TAB port efficiency curves for the non-ideal model, Mode 2.

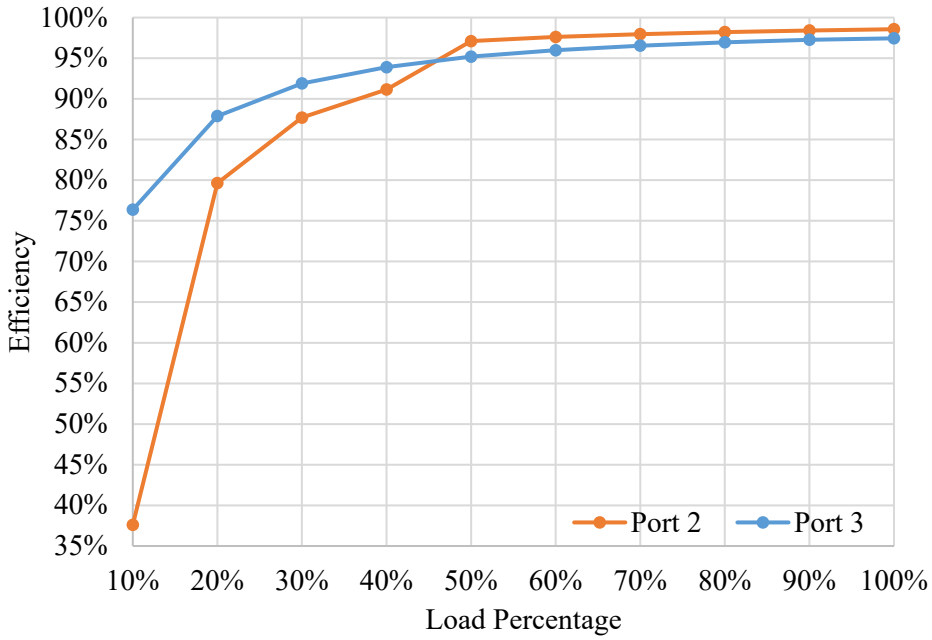

Figure 4.21: TAB port efficiency curves for the non-ideal model, Mode 3.

The increased efficiency of the converter is illustrated further by the overall efficiency curves and propulsion efficiency curve given in Figures 4.22 and 4.23. These figures show that the converter achieves over 99% overall efficiency across much of the practical load range. In the non-ideal model, the peak efficiency of the converter is 99.58%, reached at 70% of full load during Mode 1. The lowest efficiency observed is 45.98% efficiency for very low-power charging operation (Mode 3). The lowest efficiency during propulsion operation (Modes 1 and 2) is 88.39% at 10% load in Mode 2.

Finally, Figures 4.24 and 4.25 show the loss breakdown of the semiconductor modules and the steady-state junction temperatures at 100% load. Compared to the ideal model, lower junction temperatures are observed and the share of switching losses at 100% load is practically eliminated. This is due to the reduction of turn-off losses associated with

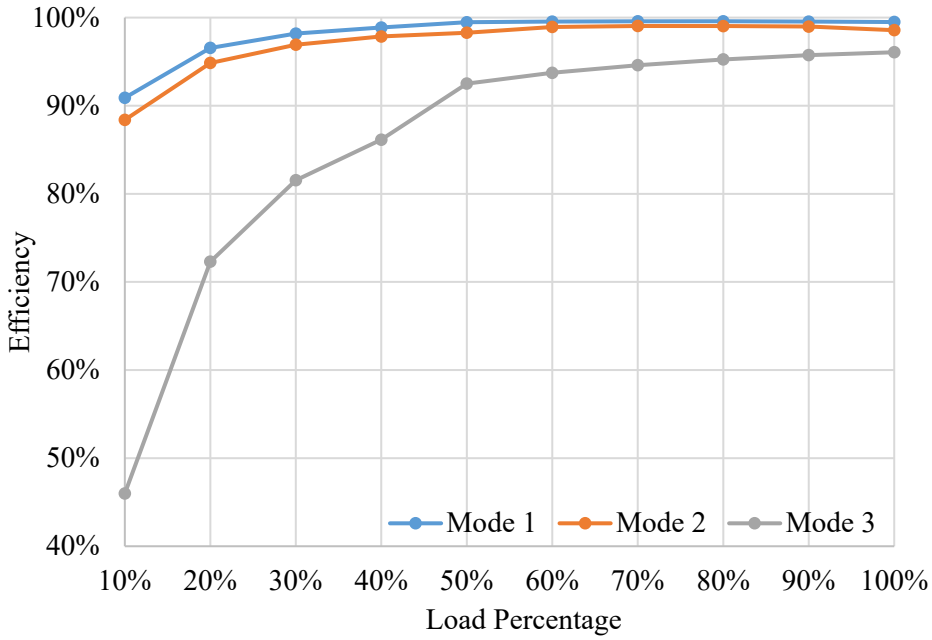

Figure 4.22: Overall efficiency of the non-ideal TAB converter in each operating mode.

the parallel capacitance and should be considered a more accurate result than that shown in the previous section.

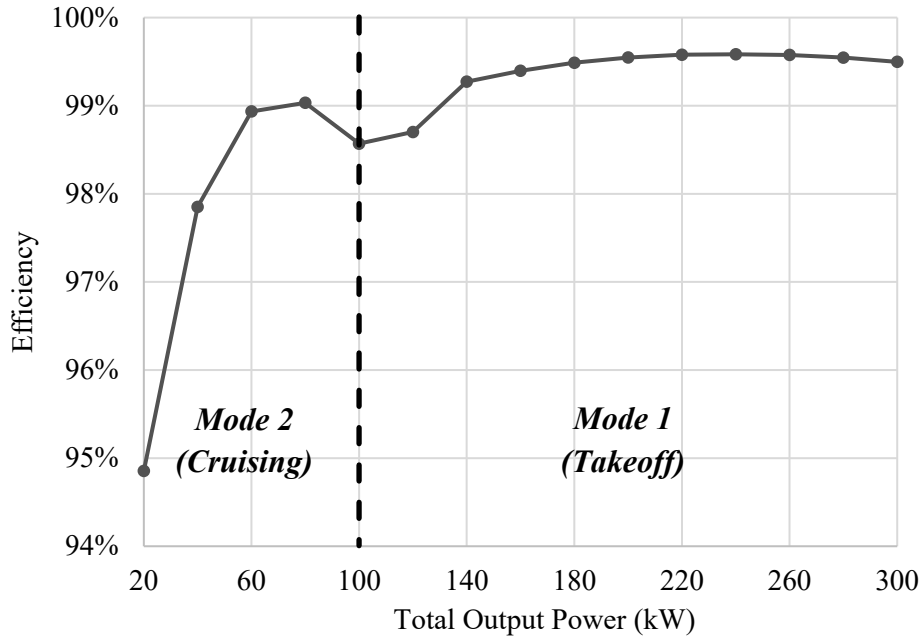

Figure 4.23: Propulsion efficiency of the non-ideal TAB converter from 20 kW to 300 kW.

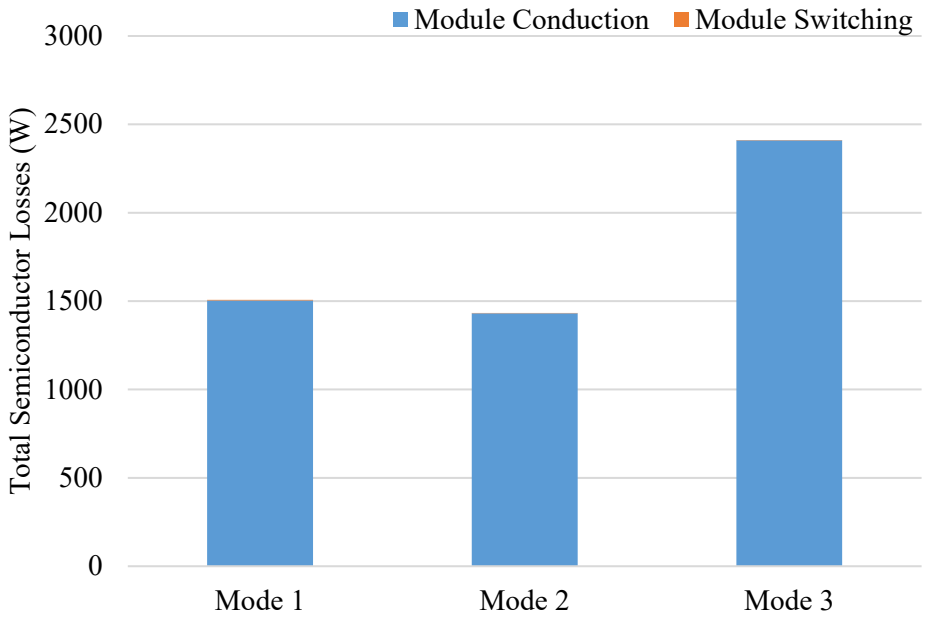

Figure 4.24: Breakdown of semiconductor module losses in the non-ideal model.

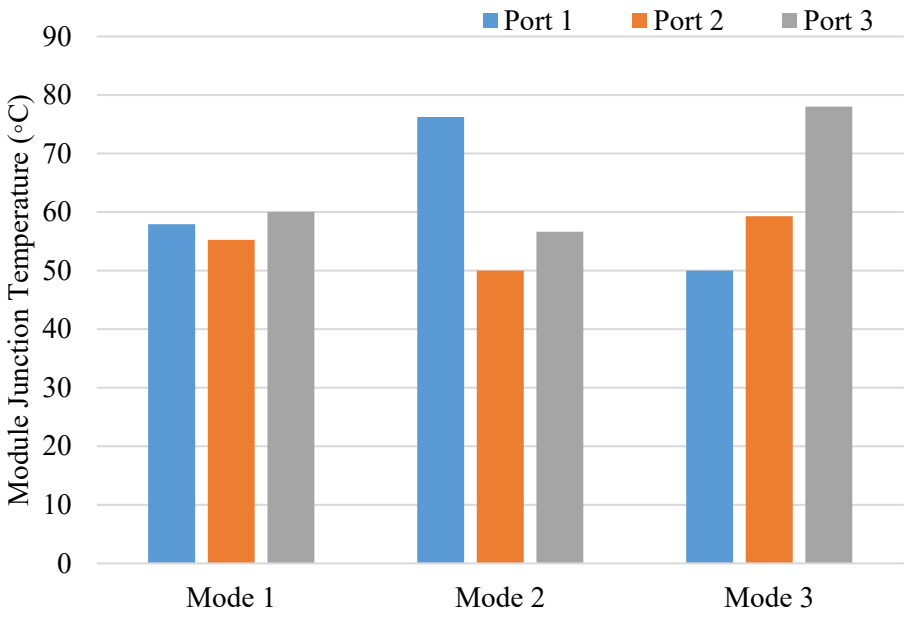

Figure 4.25: SiC module junction temperatures for each mode in the ideal model.

4.5.3 System Efficiency

In Sections 4.5.1 and 4.5.2, only the semiconductor losses of the TAB converter are considered in determining the efficiency curves. This section aims to incorporate the power electronics of the full hybrid-electric system by including a rough estimation of the transformer efficiency, as well as simulation results from the Port 1 input rectifier and Port 3 power inverter, which drives a high-speed motor. Only the propulsion modes of the converter, Modes 1 and 2, are considered in this section as Mode 3 represents an intermittent mode that is only used in edge cases like runway taxiing. Additionally, the power transfer in Mode 3 is very low compared to Modes 1 and 2 and does not present a significant risk to system feasibility in an aircraft application. The system efficiency curves for Modes 1 and 2 are presented in Fig. 4.26, using the non-ideal efficiency data to represent the TAB converter.

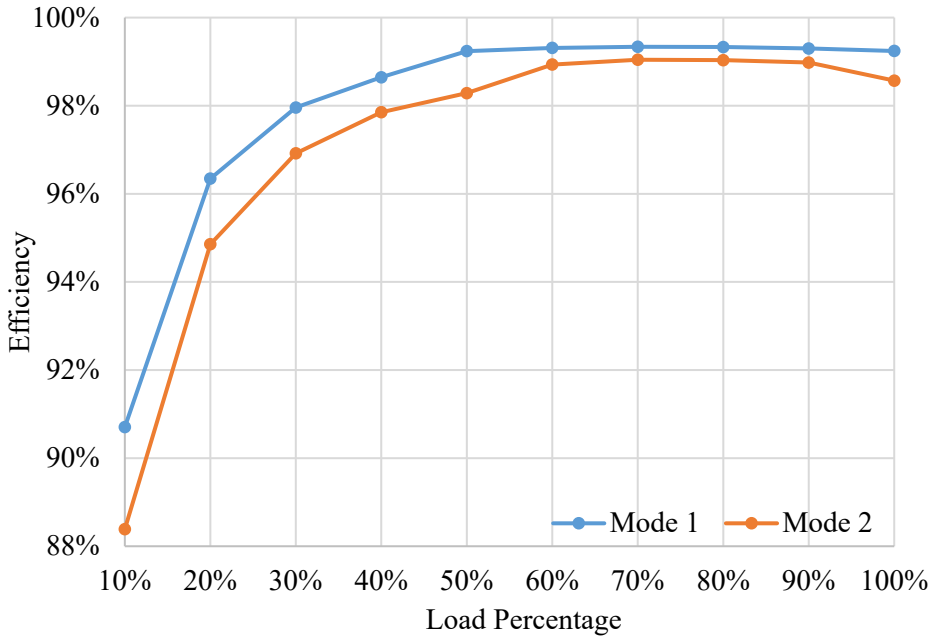

Figure 4.26: Efficiency curves of the series-hybrid power conversion system.

Compared to the semiconductor-only TAB efficiency results, the power electronics of the full system have a peak efficiency that is 0.24% lower at 99.34%. Based on these results, it should be noted that the semiconductor devices of the TAB contribute the majority of the losses in the full system and are therefore more representative of system losses than any other power electronics subsystem. Other considerations for a full system analysis would include the losses of the onboard generator, internal losses of the battery storage system, and losses associated with the propulsion motor of the aircraft, all of which are outside the scope of this thesis.

CHAPTER 5. CONCLUSIONS AND FUTURE WORK

5.1 Conclusions

In this thesis, a triple active bridge 3-port DC-DC converter is developed to interface and manage electric power between the generator, battery, and the propulsion motor load in a hybrid-electric aircraft. Takeoff, cruising, and regenerative operation modes are examined according to the power requirements of a typical hybrid-electric flight profile. Commercial SiC switching modules are chosen to reflect the cutting-edge performance available in today's semiconductor market, and a battery model typical of modern Lithium-Ion batteries is used for the energy storage.

Two models are developed in PLECS simulation software to investigate the efficiency of the converter at typical loads. In the ideal model, the switching losses of the converter are overestimated since the turn-off losses depend partially on the parasitic output capacitance of the switching devices. In the non-ideal model, a static parallel capacitor is added to the switching devices and higher efficiencies are observed, although ZVS is lost at light load conditions.

The results of the simulation prove that the converter is a highly efficient and power-dense topology suitable for hybrid-electric aircraft power management. Considering device output capacitance in the simulation, the converter reaches a peak overall efficiency of 99.74%, and a peak efficiency of 99.59% at full load operation, if only semiconductor losses are considered. Soft switching is sustained across the operating range in all modes except Mode 1 (takeoff), where ZVS is lost below 50% load. Additionally, even at a worst-case ambient temperature of 50 °C, the highest steady-state junction temperature recorded

in the non-ideal model is 72 °C, indicating safe thermal performance without the need for bulky thermal management.

5.2 Future Work

Future research on this topic could include further development in several different areas. First, a TAB converter hardware prototype can be developed, including a high-frequency transformer prototype based on the requirements calculated in Section 4.3 using Litz wire for the windings and a nanocrystalline magnetic core.

In Mode 1 of the converter, soft switching is lost under 50% load. To maximize efficiency across the entire load range, further research can focus on methods to achieve ZVS across the operating range of the TAB. This could include further development of the TAB control, hardware solutions discussed such as external parallel capacitors, or other emerging methods in the literature.

In addition to making changes for ZVS improvements, further research can validate and improve the closed-loop control with respect to both steady-state and dynamic operating conditions. Potential dynamic conditions to study could include step load increases and sudden aircraft acceleration. While control of the converter was not a primary focus of this thesis, further research can validate the robustness and performance of the converter by implementing and testing more complex methods of control.

One important area of research could be the extension of the 3-port TAB to a 4-port Quadruple Active Bridge (QAB) converter to allow for the inclusion of a supercapacitor or fuel cell port. Different energy storage options have different characteristics, and with two energy storage options they can be selected to complement one another. For example, supercapacitors have higher power density and can respond to power demand more quickly

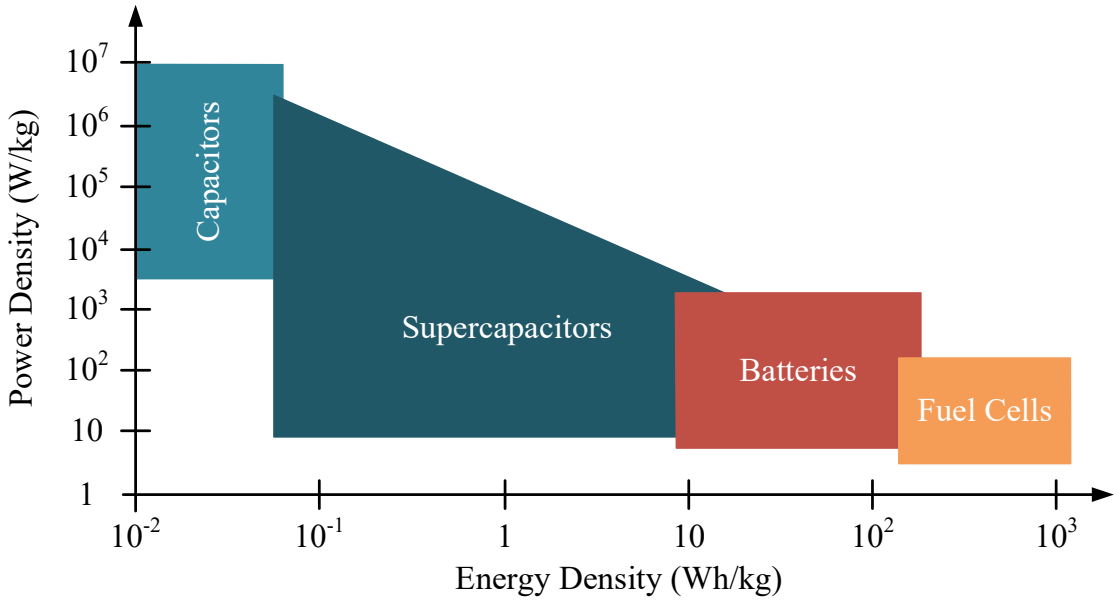

Figure 5.1: Energy and power density of various energy storage technologies [56].

than batteries, whereas a battery pack or fuel cell may be desirable for a continuous demand of energy. Fig. 5.1 depicts the energy density and power density of several energy storage technologies and illustrates why supercapacitors may be preferred alongside batteries or fuel cells to handle transient power demand.

Finally, online health monitoring of the proposed converter will be a crucial topic of research, especially for operating in a high-altitude low-pressure flight environment where the dielectric insulation characteristic and cosmic radiation will be very different from that of ground-level applications. Any semiconductor device failures (i.e., open-circuit fault or short-circuit faults) may cause cascaded system failures and even transportation accidents. Since the application of the converter is safety-critical, the converter must be thoroughly fault-tolerant and able to predict and diagnose any health degradation to avoid failure during use, such as semiconductor lifetime degradation or aging [112, 113].

REFERENCES

[1] O. P. D. M.R. Allen, W. Solecki, F. Aragón-Durand, W. Cramer, S. Humphreys, M. Kainuma, J. Kala, N. Mahowald, Y. Mulugetta, R. Perez, M. Wairiu, and K. Zickfeld, "Framing and Context," in "Global Warming of 1.5°C. An IPCC Special Report on the impacts of global warming of 1.5°C above pre-industrial levels and related global greenhouse gas emission pathways, in the context of strengthening the global response to the threat of climate change, sustainable development, and efforts to eradicate poverty," 2018.

[2] U. Irfan, "A major new climate report slams the door on wishful thinking," *Vox*, Oct. 7. [Online]. Available: https://www.vox.com/2018/10/5/17934174/climate-change-global-warming-un-ipcc-report-1-5-degrees

[3] (2015). *Aviation Emissions, Impacts & Mitigation: A Primer*. [Online] Available: https://www.faa.gov/regulations_policies/policy_guidance/envir_policy/media/Primer_Jan2015.pdf

[4] S. Gössling and A. Humpe, "The global scale, distribution and growth of aviation: Implications for climate change," *Global Environmental Change,* vol. 65, p. 102194, 2020.

[5] H. Ritchie, "Climate change and flying: what share of global CO2 emissions come from aviation?," vol. 2021, ed: Our World in Data, 2020.

[6] D. S. Lee *et al.*, "The contribution of global aviation to anthropogenic climate forcing for 2000 to 2018," *Atmospheric Environment,* vol. 244, p. 117834, 2021.

[7] B. Graver, K. Zhang, and D. Rutherford, "CO2 emissions from commercial aviation, 2018," International Council on Clean Transportation, Working Paper September 2019 2019. [Online]. Available: https://theicct.org/sites/default/files/publications/ICCT_CO2-commercl-aviation-2018_20190918.pdf

[8] J. Hoelzen *et al.*, "Conceptual design of operation strategies for hybrid electric aircraft," *Energies,* vol. 11, no. 1, p. 217, 2018.

[9] "Technology Roadmap for Environmental Improvement," ed: International Air Transport Association (IATA), 2020.

[10] "Hybrid Electric - Glenn Research Center | NASA." NASA. https://www1.grc.nasa.gov/aeronautics/eap/airplane-concepts/hybrid-electric/ (accessed November 14, 2021.

[11] S. J. Freeman, "Examining the Effects of Aviation NOx Emissions as a Short-Lived Climate-Forcer," PhD, Manchester Metropolitan University, 2017.

[12] J. Köhler and P. Jeschke, "Conceptual design and comparison of hybrid electric propulsion systems for small aircraft," *CEAS Aeronautical Journal,* vol. 12, no. 4, pp. 907-922, 2021.

[13] M. A. Rendón, J. Gallo, and A. H. Anzai, "Aircraft Hybrid-Electric Propulsion: Development Trends, Challenges and Opportunities," *Journal of Control, Automation and Electrical Systems,* pp. 1-25, 2021.

[14] R. Seresinhe, C. Lawson, and I. Madani, "Improving the operating efficiency of the more electric aircraft concept through optimised flight procedures," *CEAS aeronautical journal,* vol. 10, no. 2, pp. 463-478, 2019.

[15] T. B. Company, "Future Aircraft Power Systems- Integration Challenges," ed: University of Maryland, 2007.
[16] C. A. Authority, "Aircraft noise and health effects: Recent findings," *CAP1278,* 2016.
[17] M. Alexander-Adams, "The FAA Airport Noise Program," ed: Federal Aviation Administration, 2015.
[18] T. White, "Hybrid-Electric Propulsion--A Great Start to Reducing Aviation's Carbon Footprint," *Regional International/ERA*. [Online]. Available: https://www.collinsaerospace.com/newsroom/Stories/2020/03/White-Hybrid-Electric-Propulsion-Great-Start-Reducing-Aviation-Carbon-Footprint
[19] "Uber Elevate." https://www.uber.com/us/en/elevate/ (accessed 5/26/2021.
[20] G. E. Wroblewski and P. J. Ansell, "Hybrid-electric regional jet aircraft operation efficiency," in *2019 AIAA/IEEE Electric Aircraft Technologies Symposium (EATS)*, 2019: IEEE, pp. 1-22.
[21] A. Rolls-Royce, Alastair Stewart. "Electrifying larger aircraft." https://www.linkedin.com/pulse/electrifying-larger-aircraft-alastair-stewart/ (accessed 8/3/2021.
[22] "Master Plan 2033: Noise Management," Sydney Airport, 2013. [Online]. Available: https://assets.ctfassets.net/v228i5y5k0x4/6g11nNHs7msGQ0gUk0uAi2/63846f6b5001d80586630fd745e331ad/Chapter_14_Noise_Management.pdf
[23] E. Home *et al.*, "Sustainable Aviation Fuel: Review of Technical Pathways Report."
[24] A. Manthiram, "An outlook on lithium ion battery technology," *ACS central science,* vol. 3, no. 10, pp. 1063-1069, 2017.
[25] "OXIS Energy Set To Make Solid-State Lithium-Sulfur Cell Technology a Reality," ed, 2021.
[26] E. National Academies of Sciences and Medicine, *Commercial aircraft propulsion and energy systems research: reducing global carbon emissions*. National Academies Press, 2016.
[27] J. He, D. Zhang, and D. Torrey, "Recent advances of power electronics applications in more electric aircrafts," in *2018 AIAA/IEEE Electric Aircraft Technologies Symposium (EATS)*, 2018: IEEE, pp. 1-8.
[28] "Joby Aviation Welcomes New $75M Investment from Uber as it Acquires Uber Elevate and Expands Partnership," ed: Joby Aviation, 2020.
[29] Y. Xie, A. Savvarisal, A. Tsourdos, D. Zhang, and J. Gu, "Review of hybrid electric powered aircraft, its conceptual design and energy management methodologies," 2020.
[30] B. Schiff, "Ampaire 337 'Parallel Hybrid' Unveiled," *Aircraft Owners and Pilots Association (AOPA)*, Jun. 10. [Online]. Available: https://www.aopa.org/news-and-media/all-news/2019/june/10/ampaire-337-parallel-hybrid-unveiled
[31] R. Lenssen, "Series Hybrid Electric Aircraft: Comparing the Well-to-Propeller Efficiency with a Conventional Propeller Aircraft," 2016.
[32] "World's first serial hybrid electric aircraft to fly at Le Bourget," ed. Munich: Siemens, Diamond Aircraft, EADS, 2011.
[33] R. Dyson, "NASA hybrid electric aircraft propulsion," *NIEA Biomimicry Summit, Cleveland, OH, Oct,* vol. 4, 2017.

[34] "Airplane Concepts." NASA. https://www1.grc.nasa.gov/aeronautics/hep/airplane-concepts/ (accessed.
[35] "EHang | UAM - Passenger Autonomous Aerial Vehicle (AAV)." EHang. https://www.ehang.com/ehangaav/ (accessed 6/27/2021.
[36] R. Knight, "EHang 216 AAV Successfully Completes Trial Flights in Japan," *Inside Unmanned Systems*, Jun. 10. [Online]. Available: https://insideunmannedsystems.com/ehang-216-aav-successfully-completes-trial-flights-in-japan/
[37] P. Wolfsteller, "Joby Aviation reveals plan to go public, showcases eVTOL in flight," *FlightGlobal*, Feb. 24. [Online]. Available: https://www.flightglobal.com/airframers/joby-aviation-reveals-plan-to-go-public-showcases-evtol-in-flight-/142595.article
[38] K. Swartz, "Inside Joby's Unicorn: Flight Tests and Patents Reveal New Details," *eVTOL News*, Dec. 22. [Online]. Available: https://evtol.news/news/inside-jobys-unicorn-flight-tests-and-patents-reveal-new-details
[39] "Aircraft - BETA." https://www.beta.team/aircraft/ (accessed 6/27/2021.
[40] "Beta Technologies ALIA." eVTOL News. https://evtol.news/beta-technologies-alia/ (accessed 6/27/2021.
[41] "Products | magniX." https://magnix.aero/products (accessed 6/27/2021.
[42] C. Delbert, "World's Largest All-Electric Airplane Flies for Historic 30 Minutes," *Popular Mechanics*, May 29.
[43] "E-Fan X - Electric flight - Airbus." https://www.airbus.com/innovation/zero-emission/electric-flight/e-fan-x.html#concept (accessed 6/27/2021.
[44] "GE, NASA Partner on $12MM Program to advance the Future of Electric Flight," ed. Niskayuna, NY: GE Research, 2019.
[45] "Honeywell's Newest Turbogenerator Will Power Hybrid-Electric Aircraft, Run On Biofuel," ed. Phoenix: Honeywell International Inc., 2021.
[46] "Testbed facilities - Rolls-Royce." https://www.rolls-royce.com/innovation/testbed-facilities.aspx#/ (accessed 6/27/2021.
[47] "Rolls-Royce starts testing most powerful hybrid-electric propulsion system in aerospace," ed: Rolls-Royce plc, 2021.
[48] "Vehicles | Hybrid-Electric Aircraft." Ampaire Inc. https://www.ampaire.com/vehicles/Electric-EEL-Aircraft (accessed 6/27/2021.
[49] N. Wu, "Hybrid-Electric Plane Takes to the Skies Above Maui," *Government Technology*, Dec. 10. [Online]. Available: https://www.govtech.com/fs/transportation/hybrid-electric-plane-takes-to-the-skies-above-maui.html
[50] D. Lawhorn, V. Rallabandi, and D. M. Ionel, "Power electronics powertrain architectures for hybrid and solar electric airplanes with distributed propulsion," in *2018 AIAA/IEEE Electric Aircraft Technologies Symposium (EATS)*, 2018: IEEE, pp. 1-6.
[51] A. Trentin *et al.*, "Research and Realisation of High-Power Medium Voltage Active Rectifier Concepts for Future Hybrid-Electric Aircraft Generation," *IEEE Transactions on Industrial Electronics,* 2020.

[52] S. Adarsh and H. Nagendrappa, "Multiport Converters to Integrate Multiple Sources and Loads-A Review of Topologies," in *2018 4th International Conference for Convergence in Technology (I2CT)*, 2018: IEEE, pp. 1-7.
[53] P. C. D. Goud, A. Sharma, and R. Gupta, "Solar PV Fed Fast Charging Converter with Isolated Unidirectional Dual-Bridge Topology," in *2018 8th IEEE India International Conference on Power Electronics (IICPE)*, 2018: IEEE, pp. 1-5.
[54] H. Tao, A. Kotsopoulos, J. L. Duarte, and M. A. Hendrix, "Family of multiport bidirectional DC–DC converters," *IEE Proceedings-Electric Power Applications,* vol. 153, no. 3, pp. 451-458, 2006.
[55] N. Swaminathan and Y. Cao, "An Overview of High-Conversion High-Voltage DC–DC Converters for Electrified Aviation Power Distribution System," *IEEE Transactions on Transportation Electrification,* vol. 6, no. 4, pp. 1740-1754, 2020.
[56] J. Benzaquen, J. He, and B. Mirafzal, "Toward more electric powertrains in aircraft: Technical challenges and advancements," *CES Transactions on Electrical Machines and Systems,* vol. 5, no. 3, pp. 177-193, 2021.
[57] H. Ramakrishnan, "Bi-Directional, Dual Active Bridge Reference Design for Level 3 Electric Vehicle Charging Stations," Design Guide June 2019 2019.
[58] S. Shao, H. Chen, X. Wu, J. Zhang, and K. Sheng, "Circulating current and ZVS-on of a dual active bridge DC-DC converter: A review," *IEEE Access,* vol. 7, pp. 50561-50572, 2019.
[59] H. Bai and C. Mi, "Eliminate reactive power and increase system efficiency of isolated bidirectional dual-active-bridge DC–DC converters using novel dual-phase-shift control," *IEEE Transactions on power electronics,* vol. 23, no. 6, pp. 2905-2914, 2008.
[60] H. Tao, A. Kotsopoulos, J. L. Duarte, and M. A. Hendrix, "Transformer-coupled multiport ZVS bidirectional DC–DC converter with wide input range," *IEEE transactions on power electronics,* vol. 23, no. 2, pp. 771-781, 2008.
[61] R. Naayagi, A. Forsyth, and R. Shuttleworth, "Performance analysis of DAB DC-DC converter under zero voltage switching," in *2011 1st International Conference on Electrical Energy Systems*, 2011: IEEE, pp. 56-61.
[62] T. Bheemraj, B. Krishna, V. Karthikeyan, and S. Kumaravel, "High accurate dual loop controller for power regulation in DAB DC-DC converter for solar PV applications," in *2019 International Conference on Computing, Power and Communication Technologies (GUCON)*, 2019: IEEE, pp. 355-359.
[63] H. Liu, Q. Song, C. Zhang, J. Chen, B. Deng, and J. Li, "Development of bi-directional DC/DC converter for fuel cell hybrid vehicle," *Journal of Renewable and Sustainable Energy,* vol. 11, no. 4, p. 044303, 2019.
[64] G. Buticchi, D. Barater, L. F. Costa, and M. Liserre, "A PV-inspired low-common-mode dual-active-bridge converter for aerospace applications," *IEEE Transactions on Power Electronics,* vol. 33, no. 12, pp. 10467-10477, 2018.
[65] M. Tariq *et al.*, "Battery integration with more electric aircraft DC distribution network using phase shifted high power bidirectional DC-DC converter," in *2015 IEEE PES Asia-Pacific Power and Energy Engineering Conference (APPEEC)*, 2015: IEEE, pp. 1-5.

[66] F. Ciccarelli, L. Di Noia, S. Hamasaki, and R. Rizzo, "Thermal Analysis of DAB Converter Core used in Hybrid Aircraft Propulsion System," in *2019 International Conference on Clean Electrical Power (ICCEP)*, 2019: IEEE, pp. 705-709.
[67] H. Tao, A. Kotsopoulos, J. Duarte, and M. Hendrix, "Design of a soft-switched three-port converter with DSP control for power flow management in hybrid fuel cell systems," in *2005 European Conference on Power Electronics and Applications*, 2005: IEEE, pp. 10 pp.-P. 10.
[68] Y. Wu *et al.*, "A 150-kW 99% Efficient All Silicon Carbide Triple-Active-Bridge Converter for Solar-Plus-Storage Systems," *IEEE Journal of Emerging and Selected Topics in Power Electronics,* 2020.
[69] Z. Wang and A. Castellazzi, "SiC-based Triple Active Bridge Converter for Shipboard Micro-grid Applications with Efficient Energy Storage," in *2018 International Conference on Smart Grid (icSmartGrid)*, 2018: IEEE, pp. 39-45.
[70] R. Liu, L. Xu, Y. Kang, Y. Hui, and Y. Li, "Decoupled TAB converter with energy storage system for HVDC power system of more electric aircraft," *The Journal of Engineering,* vol. 2018, no. 13, pp. 593-602, 2018.
[71] C. Ivey, A. Alfares, and J. He, "Hybrid-Electric Aircraft Propulsion Drive Based on SiC Triple Active Bridge Converter," in *2021 IEEE/IAS Industrial and Commercial Power System Asia (I&CPS Asia)*, 2021, pp. 431-436.
[72] R. Rai and N. R. Tummuru, "Circulating and leakage power flow elimination technique between source ports in triple active bridge topology," in *2020 IEEE International Conference on Power Electronics, Smart Grid and Renewable Energy (PESGRE2020)*, 2020: IEEE, pp. 1-6.
[73] L. Jiang and D. Costinett, "A triple active bridge DC-DC converter capable of achieving full-range ZVS," in *2016 IEEE Applied Power Electronics Conference and Exposition (APEC)*, 2016: IEEE, pp. 872-879.
[74] T. Ohno and N. Hoshi, "Analysis of Intermittent Control for Triple Active Bridge Converter to Suppress Cross-current," in *2021 IEEE 12th Energy Conversion Congress & Exposition-Asia (ECCE-Asia)*, 2021: IEEE, pp. 391-396.
[75] "BaSiCs of SiC: Silicon Carbide as a Semiconductor," Jan 09, 2020.
[76] G. Vacca, "Benefits and advantages of silicon carbide power devices over their silicon counterparts," *Semicond. Compd. Adv. Silicon,* vol. 12, no. 3, pp. 72-75, 2017.
[77] J. Bigorra, C. Borrego, J. Fontanilles, and J. Giró, "Innovative electrical and electronic architecture for vehicles with dual voltage power networks. In-vehicle application," *SAE transactions,* pp. 232-239, 2000.
[78] A. Semiconductor, "Cosmic Ray Failures of Power Semiconductor Devices," *IEEE Spectrum*, Jun. 21, 2019. [Online]. Available: https://spectrum.ieee.org/cosmic-ray-failures-of-power-semiconductor-devices
[79] J. J. Aw, "Cosmic radiation and commercial air travel," *Journal of travel medicine,* vol. 10, no. 1, pp. 19-28, 2003.
[80] H. Asai *et al.*, "Tolerance against terrestrial neutron-induced single-event burnout in SiC MOSFETs," *IEEE Transactions on Nuclear Science,* vol. 61, no. 6, pp. 3109-3114, 2014.
[81] C. Felgemacher, S. V. Araujo, P. Zacharias, K. Nesemann, and A. Gruber, "Cosmic radiation ruggedness of Si and SiC power semiconductors," in *2016 28th*

International Symposium on Power Semiconductor Devices and ICs (ISPSD), 2016: IEEE, pp. 51-54.

[82] F. Principato, S. Altieri, L. Abbene, and F. Pintacuda, "Accelerated Tests on Si and SiC Power Transistors with Thermal, Fast and Ultra-Fast Neutrons," *Sensors,* vol. 20, no. 11, p. 3021, 2020.

[83] G. Soelkner, W. Kaindl, M. Treu, and D. Peters, "Reliability of SiC power devices against cosmic radiation-induced failure," in *Materials science forum*, 2007, vol. 556: Trans Tech Publ, pp. 851-856.

[84] A. A. Martins and M. J. Pinheiro, "On the propulsive force developed by asymmetric capacitors in a vacuum," *Physics Procedia,* vol. 20, pp. 112-119, 2011.

[85] R. Glassock, V. Madonna, P. Giangrande, and M. Galea, "RexMoto-a range extender concept for light electric aircraft," in *2020 IEEE Transportation Electrification Conference & Expo (ITEC)*, 2020: IEEE, pp. 930-935.

[86] M. Hepperle, "Electric flight-potential and limitations," 2012.

[87] J. Olsen and J. R. Page, "Hybrid powertrain for light aircraft," *International Journal of Sustainable Aviation 15,* vol. 1, no. 1, pp. 85-102, 2014.

[88] M. T. Heinrich, F. Kelch, P. Magne, and A. Emadi, "Regenerative braking capability analysis of an electric taxiing system for a single aisle midsize aircraft," *IEEE Transactions on Transportation Electrification,* vol. 1, no. 3, pp. 298-307, 2015.

[89] K. Nishimoto, Y. Kado, R. Kasashima, S. Nakagawa, and K. Wada, "Decoupling power flow control system in triple active bridge converter rated at 400 V, 10 kW, and 20 kHz," in *2017 IEEE 8th International Symposium on Power Electronics for Distributed Generation Systems (PEDG)*, 2017: IEEE, pp. 1-6.

[90] C. Zhao, S. D. Round, and J. W. Kolar, "An isolated three-port bidirectional DC-DC converter with decoupled power flow management," *IEEE transactions on power electronics,* vol. 23, no. 5, pp. 2443-2453, 2008.

[91] O. Takanobu and N. Hoshi, "A new control method for triple-active bridge converter with feed forward control," in *2018 International Power Electronics Conference (IPEC-Niigata 2018-ECCE Asia)*, 2018: IEEE, pp. 971-976.

[92] M. Pahlevaninezhad, P. Das, J. Drobnik, P. K. Jain, and A. Bakhshai, "A novel ZVZCS full-bridge DC/DC converter used for electric vehicles," *IEEE Transactions on Power Electronics,* vol. 27, no. 6, pp. 2752-2769, 2011.

[93] G. N. B. Yadav and N. L. Narasamma, "An active soft switched phase-shifted full-bridge DC–DC converter: analysis, modeling, design, and implementation," *IEEE Transactions on power Electronics,* vol. 29, no. 9, pp. 4538-4550, 2013.

[94] M. R. Ahmed, R. Todd, and A. J. Forsyth, "Predicting SiC MOSFET behavior under hard-switching, soft-switching, and false turn-on conditions," *IEEE Transactions on Industrial Electronics,* vol. 64, no. 11, pp. 9001-9011, 2017.

[95] S. Tiwari, J. K. Langelid, O.-M. Midtgård, and T. M. Undeland, "Hard and soft switching losses of a SiC MOSFET module under realistic topology and loading conditions," in *2017 19th European Conference on Power Electronics and Applications (EPE'17 ECCE Europe)*, 2017: IEEE, pp. P. 1-P. 10.

[96] T. Halder, "Hard and Soft Switching Geometries For Operations of the MOSFET Used For the SMPS," in *2021 Devices for Integrated Circuit (DevIC)*, 2021: IEEE, pp. 1-6.

[97] Y. Zhang, X.-F. Cheng, and C. Yin, "A soft-switching non-inverting buck–boost converter with efficiency and performance improvement," *IEEE Transactions on Power Electronics,* vol. 34, no. 12, pp. 11526-11530, 2019.
[98] D. Zhang, J. He, and D. Pan, "A megawatt-scale medium-voltage high-efficiency high power density "SiC+ Si" hybrid three-level ANPC inverter for aircraft hybrid-electric propulsion systems," *IEEE Transactions on Industry Applications,* vol. 55, no. 6, pp. 5971-5980, 2019.
[99] M. R. Yazdani and M. Farzanehfard, "Evaluation and comparison of conducted EMI in three full-bridge DC-DC switching converters," in *2019 10th International Power Electronics, Drive Systems and Technologies Conference (PEDSTC)*, 2019: IEEE, pp. 439-444.
[100] H. Chung, S. Hui, and K. Tse, "Reduction of power converter EMI emission using soft-switching technique," *IEEE Transactions on Electromagnetic Compatibility,* vol. 40, no. 3, pp. 282-287, 1998.
[101] Z. Emami, H. Farzanefard, and S. Motahari, "EMI evaluation in hard switching and soft switching PWM flyback converters," in *2010 1st Power Electronic & Drive Systems & Technologies Conference (PEDSTC)*, 2010: IEEE, pp. 46-51.
[102] Y.-S. Lee and S.-C. Chu, "EMI performance comparison of switched-capacitor bidirectional converter with and without QR ZCS," in *2009 International Conference on Power Electronics and Drive Systems (PEDS)*, 2009: IEEE, pp. 1137-1142.
[103] I. Technologies, "How to Select the Right CoolMOS and its Power Handling Capability," Germany, Application Note 2002.
[104] O. Tremblay and L.-A. Dessaint, "Experimental validation of a battery dynamic model for EV applications," *World electric vehicle journal,* vol. 3, no. 2, pp. 289-298, 2009.
[105] "Powder Core Loss Calculation," Design Guide. [Online]. Available: mag-inc.com
[106] S. Barqi, "Optimum design approach of high frequency transformer: including the effects of eddy currents," in *2018 15th International Multi-Conference on Systems, Signals & Devices (SSD)*, 2018: IEEE, pp. 298-303.
[107] C. Jiang, X. Li, S. S. Ghosh, H. Zhao, Y. Shen, and T. Long, "Nanocrystalline powder cores for high-power high-frequency power electronics applications," *IEEE Transactions on Power Electronics,* vol. 35, no. 10, pp. 10821-10830, 2020.
[108] D. Ruiz-Robles, E. L. Moreno-Goytia, V. Venegas-Rebollar, and N. M. Salgado-Herrera, "Power Density Maximization in Medium Frequency Transformers by Using Their Maximum Flux Density for DC–DC Converters," *Electronics,* vol. 9, no. 3, p. 470, 2020.
[109] "Transformer Design," Design Guide. [Online]. Available: mag-inc.com
[110] R. Hou, J. Lu, and D. Chen, "Parasitic capacitance Eqoss loss mechanism, calculation, and measurement in hard-switching for GaN HEMTs," in *2018 IEEE Applied Power Electronics Conference and Exposition (APEC)*, 2018: IEEE, pp. 919-924.
[111] F. Stückler, S. Abdel-Rahman, and K. Siu, "600 V CoolMOS C7 Design Guide: Tuning the limits of Silicon," Application Note 2015.

[112] J. He, N. A. Demerdash, N. Weise, and R. Katebi, "A fast on-line diagnostic method for open-circuit switch faults in SiC-MOSFET-based T-type multilevel inverters," *IEEE Transactions on Industry Applications,* vol. 53, no. 3, pp. 2948-2958, 2017.
[113] J. He, R. Katebi, N. Weise, N. A. Demerdash, and L. Wei, "A fault-tolerant T-type multilevel inverter topology with increased overload capability and soft-switching characteristics," *IEEE Transactions on Industry Applications,* vol. 53, no. 3, pp. 2826-2839, 2017.

VITA

Cole M. Ivey graduated Magna Cum Laude from the University of Kentucky in August 2020 with a Bachelor of Science in Electrical Engineering. During his undergraduate period, Cole was involved with the UK Solar Car Team, eventually joining team leadership with the position of Electrical Team Co-Lead. Professionally, he completed two co-op experiences before graduating. While pursuing a Master of Science in Electrical Engineering, Cole was supported by the Tennessee Valley Authority Teaching Assistantship as well as a NASA KY grant led by Dr. JiangBiao He. He has published a research paper as the first author titled "Hybrid-Electric Aircraft Propulsion Drive based on SiC Triple Active Bridge Converter" in the 2021 IEEE Industrial & Commercial Power System Asia Conference. Currently, Cole is employed as a full-time electrical engineer at Ethicon, a subsidiary of Johnson & Johnson.